Pattern Transfer and Characterization of Biomimetic Micro-Structured Surfaces for Hydrophobic and Icephobic Applications

by

Brendan McDonald

A thesis
presented to the University of Waterloo
in fulfillment of the
thesis requirement for the degree of
Master of Applied Science
in
Chemical Engineering - Nanotechnology

Waterloo, Ontario, Canada, 2013

Author's Declaration

I hereby declare that I am the sole author of this thesis. This is a true copy of the thesis, including any required final revisions, as accepted by my examiners.

I understand that my thesis may be made electronically available to the public.

Abstract

Using both artificial and natural templates, biomimetic micro-structures are fabricated on conventional coating materials (epoxy and silicone elastomers) to mimic both artificial and natural templates through effective pattern transfer processes. The pattern transfer processes use a soft-polymer negative stamp, where the flexibility of the stamp allows for easy conformation to both flat and curved surfaces. Patterns have been successfully transferred as a rigid epoxy to complex surfaces or as a soft elastomer replica of a hydrophobic Trembling Aspen leaf. The hydrophobicity and friction behaviour of the resulting micro-patterned surfaces are systematically investigated, showing that surface patterning can be used as an effective way to improve hydrophobicity while reducing the surface adhesion and friction without a loss of the structural integrity or rigidity typical of epoxy coatings. The relative strength of the micro-pattern was determined through indentation testing in order to support the claim of a robust pattern on the micro-scale that is able to withstand the harsh environment of industrial application or weather exposure.

With the well characterized patterned epoxy material fabricated and able to be transferred to many different surfaces, the potential for the patterned surface to act as an icephobic coating was pursued. The robustness of the epoxy material with the unique ability to coat surfaces that are typically unable to possess a micro-structure makes this coating an ideal candidate for large-scale icephobic application. The potential use of a micro-patterned epoxy coating is investigated against comparable surface coatings within an innovative experimental set-up to measure the relative ice-adhesion strength of different substrates. In characterizing the relative shear-force required to remove frozen water droplets from the coating surface at the interface, several variables and factors were explored. The addition of a surface pattern was found to impact the icephobic ability of several materials, where different materials with the same pattern were compared to identify that the surface energy of the substrate influences the icephobic nature of a surface. Moreover, previous studies that relate the water contact angle or hysteresis to ice-adhesion strength are questioned through a preliminary qualitative analysis of ice adhesion strength data. This work demonstrates a potential process for the utilization of biomimetic epoxy micro-patterns as an enhanced hydrophobic and icephobic option for large scale protective coatings.

Acknowledgements

I would like to express my thanks and gratitude to all of those who have helped me shape and develop my work to its current state with the hope that it shall be continued and those following will be able to build upon this foundation. To my research supervisor, Professor Boxin Zhao, I would express my appreciation for providing a solid footing and an open approach in allowing me to explore the field of biomimetics, and learn at the forefront of this research.

All of my family and friends have provided constant support both by contributing their time and by continually providing an extra push or challenge to help me through and over all obstacles. I would like to thank my lab-mates and all of those who have helped me in training, and in thinking of the many solutions that were found over my time as part of this research group. All of these people have made sure that I was able to keep a light-hearted approach to my work, while maintaining the focus required. More specifically, I would like to acknowledge the contributions of several individuals who have directly aided me in my work. Owen Crookston, an undergraduate research assistant played a large role in refining the friction testing of the epoxy surfaces and collecting a complete data set. Poonam Patel has offered much of her time as a volunteer to offer her knowledge from a biological perspective and help shape the direction of the biological mimicry work while also with sample fabrication and characterization. Both Aleksander Cholewinski and Josh Trinidad, fellow graduates of the University of Waterloo Nantechnology Engineering program have spent a great deal of time developing an alternate coating process within our lab that was trialed as part of the icephobic research proposed, as well as collecting data for that work. Current PhD candidate Hamed Shahsavan provided much insight and direction for the friction characterization of the epoxy pillar system, and was recognized with the second authorship of that paper. Additionally, there have been countless others who have played a large role in my training, understanding, and development as a student, to all of whom I am grateful.

Table of Contents

List of Figures

List of Tables

Chapter 1
Introduction

Research Objective and Development

Inspired by the superhydrophobic properties and surface micro-structures observed on lotus leaves and other natural plants, the fabrication of surface patterns at the micro and nanometer scale is growing as an alternative approach to manipulate and improve the interfacial properties of wetting, adhesion, and friction [1–5]. The intent of this research is to generate a successful pattern transfer mechanism to transfer biological and biologically inspired patterns from one surface to another. This work investigates the feasibility of applying micro-features to common coating polymer resins with the purpose of tuning the hydrophobicity and friction behaviour of patterned surfaces. With the application of these patterns, several interesting phenomena can be observed such as the replication of the *lotus-effect*; combining a superhydrophobic state with controllable self-cleaning smart properties [3], [4], [5], [6], [7]. The Lotus Effect derives from the mechanism of cleaning observed on the Lotus leaf which is superhydrophobic; these natural surfaces promote the agglomeration of water into droplets that will roll off the surface at low incline angles removing dust, spores, and other particulate matter in the presence of rain, dew, and even fog [1], [8], [9], [10], [11], [12]. In nature, this ability allows for plants to clean themselves and maximize their exposure to sunlight. Some insects employ similar surface structures to take advantage of this phenomenon and collect or manipulate the flow of water within arid environments. It has been found that self-cleaning surfaces are typically very rough, which is responsible for the wetting mechanism that generates the superhydrophobic state. The close proximity of micro- and nano-scale surface structures allows water droplets to sit on top of the asperities, effectively reducing the real area of contact at the liquid-solid interface. A secondary benefit of the surface pattern is the reduction of adhesion for solid contaminates that are sitting on the surface, where the reduced real contact between the particulate and the surface effectively makes any contaminate easier to remove.

There are many examples in nature that show how different species of plants, animals, and insects utilized surface patterns to achieve superhydrophobic or low-adhesion properties so that they can do extraordinary things. Butterfly wings promote anisotropic wetting, where directional micro- and nano-structures on the surface will control the flow of water on the low wetting surfaces [13]. Many different plants, such of the Trembling Aspen (populous tremuloides) which can be found on the University of Waterloo campus use a hydrophobic surface as a self-cleaning mechanism that removes contaminates from the surface in order to make photosynthesis more efficient. Found throughout North America, the Trembling Aspen is a medium size deciduous tree that can grow to 25 meters in height, and are typically found in moist areas although the species is able to grow in many different climate conditions. Similarly,

insects like the Stenocara Beetle also use the ability of enhanced hydrophobicity through a pattern on its back to collect water from fog or moist air to survive in dry and arid conditions [1]. As detailed by Bhushan et al., even different plant species within the same family can include vastly different properties. He observed that even though two different species of roses contained superhydrophobic surfaces, one was high-adhesion and the other low. This was found to be the result of different sized asperities that were packed at different densities on the surface which could be used to tune the adhesion of water droplets [12].

The patterns developed within this work are produced with the intent to induce superhydrophobic behaviour and to manipulate the relative adhesive and friction properties from their molecularly smooth counterparts. There are several procedures that have been developed to serve different requirements. An ordered array of Polydimethylsiloxane (PDMS) pillars was generated through both single and a dual-pattern transfer procedure using photolithographically patterned SU-8 arrays of pillars and holes as initial moulds. This process was extended to the use of tree leaf samples as a mould, where the biologically optimized patterns are able to be copied to both soft and rigid materials. Additionally, rigid patterns of SU-8 were able to be copied in the form of an epoxy coating tailored to fulfill a specific role as a robust and controlled patterned surface. The highlight of this pattern transfer procedure is the ability to replicate a pattern with a rigid thermoset polymer onto not only flat, but also curved or more complex surfaces. Moreover, the size of the patterned area is only limited by the curing conditions that are applied through the procedure. Thus the micro-patterned epoxy can potentially serve as a coating layer within large scale industrial or outdoor applications. Contrary to direct surface patterning techniques, the designed two-stage pattern transfer process can be applied to many different surfaces traditionally unable to be patterned due to the issue of restricted availability or complex and expensive approaches. The strength of the patterned epoxy structures was examined through indentation testing. The hydrophobicity and friction behaviour of the fabricated arrays of epoxy micro-pillars were systematically investigated, showing a large increase in hydrophobicity along with a decrease in friction. These advantages combined with the rigid and robust nature of the epoxy pillars suggests the potential for the patterned material to serve as a passive icephobic coating layer as many current solutions are too fragile.

Through characterization, the addition of a surface pattern results in an increase in hydrophobic behaviour for all materials trialed, while decreases in frictional forces are also apparent. Further investigation looks to link one or both of the increasing hydrophobicity or decreasing adhesion and friction forces to a decrease in the ability of ice to form, or adhere to the surface. It has been established that the addition of a modified physical structure that generates a superhydrophobic wetting state results in a delayed freezing time, and decreases the ice-adhesion force for droplets contacting the cooled surface [14], [15], [16], [17]. However, the common flaw for many icephobic surfaces is their ability to maintain

their functionality over time [17]. Both soft PDMS and rigid epoxy patterns were fabricated, where both materials proved to be capable of maintaining their integrity following multiple freeze thaw cycles. However, the PDMS was able to be easily destroyed with the application of a slight abrasive force. Conversely, the stronger mechanical properties and higher elastic modulus of the epoxy material indicate that these surfaces should be sufficient for withstanding weathering and mechanical stresses while retaining functionality.

The following sections offer an introduction to influential areas of study including the primary topics of superhydrophobicity, icephobicity and pattern transfer. Each topic is expanded to outline the basis of each field and the relevant role played by each in the development of the hydrophobic and icephobic micro-structured surfaces.

Superhydrophobicity

The hydrophobic properties of micro-structured systems have been studied in depth, and are well characterized. Within literature, it is understood that superhydrophobic surfaces are the result of a combination of chemical and physical surface properties [2], [7], [18], [19], [20]. At the solid-liquid interface adhesive forces between the liquid and solid will promote spreading, whereas the cohesive forces of the liquid will cause it to bead up and minimize contact with the surface. The addition of micro- and/or nano-patterns to the surface increases the real surface area. However, the nominal contact area may be reduced due to the droplet sitting on top of air-pockets trapped within the protrusions on the surface. Superhydrophobic surfaces possess many different beneficial properties for numerous applications, where droplets of water will bounce off of them, and gently places droplets will rest on the surface in spheres until any applied force will cause them to roll.

Replica moulding techniques have generated high aspect-ratio pillar arrays from polymeric materials such as epoxy, polyurethane, and hydrogels with lateral dimensions ranging from 300nm to 1μm [2], [5], [15], [18], [21]. Through employing high aspect ratio micro-pillar arrays, the addition of surface roughness will allow for a greater surface area and control over interfacial properties. The inspiration of using a micro-pillar array is derived from nature, wherein many different plant, animal, and insect species benefit from surfaces that have a specific function. The leaves of the Trembling Aspen referenced within this thesis possess a protective coating of lipophilic structures deposited on the outer structures of the leaf. This layer comprises of an insoluble polymer of omega hydroxyl acids interlinked through ester bonds that serve primarily to retain moisture within the leaf. There are also several lipid layers that form a wax consisting primarily of aliphatic compounds such as alkanes, aldehydes, ketones, primary and secondary alcohols and esters. The projected wax crystals on the surface of the leaf result in both light reflection and the sought after non-wetting properties. The observed non-wetting nature is due

to both the aforementioned wax coating on the surface as well as and the hierarchical nature of the surface pattern formed. The surface of superhydrophobic plant species consists of micro-scale papillae, or bumps, covered with nano-scale wax crystals. This architecture creates a low-adhesion self-cleaning surface which allows a water drop to roll on the surface given very little incline. To take advantage of the wetting nature of the leaf biology, the Trembling Aspen has evolved in two specific ways. First, the Trembling Aspen is known for a the long leaf stem relative to other tree species which along with the perimeter of the leaf being covered with long petioles serve to promote a slight vibration of the leaf even in low wind conditions which gives the species the descriptive *trembling* title, and provides the incline and kinetic energy that promotes the rolling action of the water droplets.

In order to synthesize superhydrophobic surfaces, both the chemical and physical properties must be tailored to resist wetting. However it is the physical pattern that is ultimately responsible for any superhydrophobic properties. The contact angle of Teflon®, a common non-stick coating polymer, is only 110°; to be defined as a superhydrophobic surface, the contact angle should be greater than 150°. Therefore even the materials that possess some of the lowest surface energies are unable to achieve a superhydrophobic state without some sort of modification.

There are two general pathways to take when attempting to fabricate a superhydrophobic material. You can either add a surface roughness with the application of a low surface energy material, or you can simply roughen a low-energy material. The methods described in this report focus on the idea of adding roughness to low energy materials, both by adding an array of micro-pillars or by mimicking the pattern observed on the Trembling Aspen leaves.

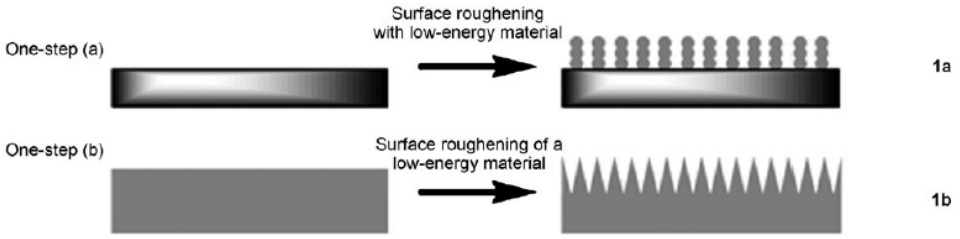

Figure 1: The two one-step methods of generating a superhydrophobic surface through combining both chemical and physical properties to maximize the non-wetting potential of a material [2]

Superhydrophobic surfaces require some sort of structuring, which is able to be achieved with the deposition of particles [10], photolithography [22], or by the growth of roughness through the vapour deposition growth of carbon nano-tubes [2]. Any of these pathways is able to be further enhanced with a subsequent treatment to enhance the chemical hydrophobicity of the protrusions in order to better resist the penetration of liquid between the asperities. Superhydrophobicity also is generally improved with an increased density of protrusions on the surface material such that any meniscus between two contact points is unable to reach the substrate between the structures. Furthermore, the hysteresis and the effective

rolling angle of a droplet is able to be further reduced with the introduction of a hierarchical patterned surface where texture is added to the already rough surface on the nano-scale to further prevent the droplet from achieving contact with the material [7]. When deciding on how to fabricate a superhydrophobic surface, there are several practical issues that must be addressed such as the material's ability to survive any roughening process. Furthermore, there are specific physical constraints that are present on any physical surface, where the structures must be able to withstand the intermolecular forces and maintain structural integrity against competing pillar-pillar and pillar-substrate interacting forces.

Icephobicity

The icing of structures and surfaces has long been an issue that has resulted in the destruction and inefficiency of many structures, power lines, and equipment. Therefore, a potential means to prevent or reduce the amount of ice that accumulates and adheres to surfaces is of great interest. Research has long been active with the intent of synthesizing a passive measure to reduce or eliminate ice-adhesion. Currently there are no materials that can be considered completely ice-phobic by possessing the ability to prevent ice-formation or adhesion within a super-cooled environment Nonetheless there are materials that are able to reduce the ability of ice to adhere and impede ice formation. With the introduction of micro and nano-patterning techniques allowing for greater control over the physical structure of surfaces, both superhydrophobic surfaces have found many new applications, one of which is icephobic coatings. This method of surface modification is considered to be passive, in that there is no energy input, which is ideal for large-scale or remote applications. Passive methods of anti-icing or de-icing surfaces are preferable to other ice repellent techniques such as heaters or physical removal due to the longevity of the solution and little to no upkeep cost. Research involving the behaviour of water in contact with super-cooled surfaces has not been explored in depth, and most studies concerning the icephobicity of surfaces generally is unable to quantify observed results over a range of temperatures. With this approach, the icephobic coating synthesized is hydrophobic in order to impede the formation of ice by deterring the presence of water wetting the surface within a super-cooled environment. This behaviour is observed with the induction of both a high contact-angle to indicate hydrophobicity in conjunction with a low slip-angle indicating that the water is easily able to roll from the surface. It has been observed that hydrophobic surfaces that possess low contact angle hysteresis delay the freezing time of water droplets [23].

There are three primary means to generate icephobic coatings: first a self-assembled monolayer of $–CH_3$ or $–CF_3$ low surface-energy groups that are hydrophobic; secondly a mixture of at least two different hydrophobic components that will interrupt the liquid-like layer sitting on the surface and reduce specific bonds; and finally, a structured and porous deposit that will generate air pockets at the interface to provide stress and prevent a complete adhesion [24]. The proposed study will utilize a combination of

all three measures to generate an icephobic surface. The application of a micro-pattern to a surface demonstrates the ability to reduce ice-adhesion strength, while functioning as a coating able to delay the onset of freezing. The function of the surface pattern is to mimic the Lotus Effect in optimizing the inclusion of air-pockets at the solid-liquid interface with the promotion of the Cassie-Baxter wetting mechanism.

The development of an in-lab icing experimental set-up focuses on attempting to recreate the rime icing mechanism. The freezing of super cooled water droplets as they contact a sub-zero temperature surface represents the primary concern for outdoor applications that are hampered with ice formation and build-up. By recreating these conditions, the potential of a surface to generate nucleation sites for icing to occur, while also minimizing the ability of the droplet to freeze to the surface material can be observed. Within environments where rime icing is prevalent, it is important to study the potential of water droplets to penetrate the surface of the patterned array of asperities. The role of external forces such as strong winds or increased droplet momentum can lead to greater penetration of the water droplets into the surface, and must be considered.

Biomimetic Pattern Transfer and Surface Coatings

There are two primary pattern transfer procedures developed within this work. The common theme of the pattern transfer is the ability to mimic a surface pattern onto a new substrate. This has been achieved through a two-step soft-lithographic approach which is able to be applied to both soft and rigid polymers. Each transfer process was developed with a specific purpose; the transfer of a rigid pattern to a rigid epoxy material creates a robust surface, and the transfer of a biological pattern to a soft elastomer accurately replicates a natural pattern.

Different materials and techniques have been used in the fabrication of micro structured patterns, including PDMS, polyurethanes, SU-8, silicon, etc [25]. In contrast to well-characterized polymer systems, the hydrophobic benefits of adding a micro-pattern to an epoxy material have not been explicitly studied beyond the effect of pattern density [7] or geometry [26] with the exception of the common epoxy photoresist SU-8. Although conventional industrial epoxies have not typically been explored as a candidate for micro-patterning, they offer a good potential for pattern transfer within large-scale industrial applications. Epoxy resins are already used commonly as protective coatings or adhesives and can be found within automotive, aeronautic, and wind-harnessing industries. Providing a means to transfer a physical micro-pattern to the epoxy surface can impart beneficial engineering properties to conventional applications. The ability to accurately transfer micro-patterns to these surfaces offers a means to improve conventional protective coatings while providing the additional benefit of control over the wetting and tribological behaviour of the surface.

Chapter 2

Literature Review

This chapter serves to outline and review the primary principles and mechanisms supporting the major concepts covered within this thesis. The thermodynamic principles of wetting and the involved intermolecular forces that play a role at the interface are addressed along with the supporting theory of wetting. The contact angle is defined as a measure of wetting, along with the dynamic theory of wetting before equilibrium conditions are met and under non-thermodynamic ideal conditions resulting in contact angle hysteresis. Young's equation, considered as the backbone of any wetting theory, is derived along with the theoretical definitions that have followed with a practical role in real systems. As any surface is not infinitely smooth at the atomic scale, the two main wetting mechanisms that describe the non-ideal nature of wetting with the addition of roughness are discussed. Finally, the primary theories supporting adhesion and friction, and the non-ideal nature of contact between two mating materials, are discussed. Each of these material and surface properties are able to be modified and controlled by tuning specific properties such as the roughness, surface compliance, and chemical heterogeneity to achieve specific goals.

Intermolecular Forces

The text Intermolecular and Surface Forces outlines the two primary intermolecular forces of van der Waals and the electrical double-layer (EDL) exist in an attraction and repulsive competition with one another. The van der Waals attraction, named after Dutch scientist J.D. van der Waals, describes the attractive forces between molecules due to their dipole moments. Van der Waals forces are a combination of three primary interactions: permanent dipole forces, dipole-induced forces, and instantaneously induced dipole-induced dipole (London dispersion force). Many molecules have a permanent dipole due to the charge imbalances that exist through the molecular structure (e.g., H_2O, HCl). Conversely, neutral molecules (e.g., O_2, N_2) can possess a separation of charges, giving rise to a temporary dipolar state. Thus, van der Waals forces are considered universal and exist on all surfaces. Van der Waals forces are only relevant on a short range and they decay rapidly with an increasing distance, D, where at the molecular or atomic level, van der Waals attraction energy is proportional to D^{-6}. The electric double layer (EDL) force can be thought of as a shell that appears on a charged surface when it is placed into an (aqueous) liquid. It consists of two parallel layers of ions. The first layer is the surface charge at the solid–liquid interface (known as the Stern layer) and the second layer is in the fluid (known as diffuse layer), where it electronically screens the first layer. In the diffuse layer, the electrical potential decays exponentially within tens of nanometers from the surface [27].

The Derjaguin-Landau-Verwey-Overbeek (DLVO) Theory combines both the van der Waals attraction and the double-layer repulsion into a total or net energy interaction. According to the DLVO theory, two particles will attract each other from a long distance until the double-layer force generates a potential wall when the particles are very close. If this energy barrier can be overcome, the particles will attract each other strongly, resulting in aggregation.

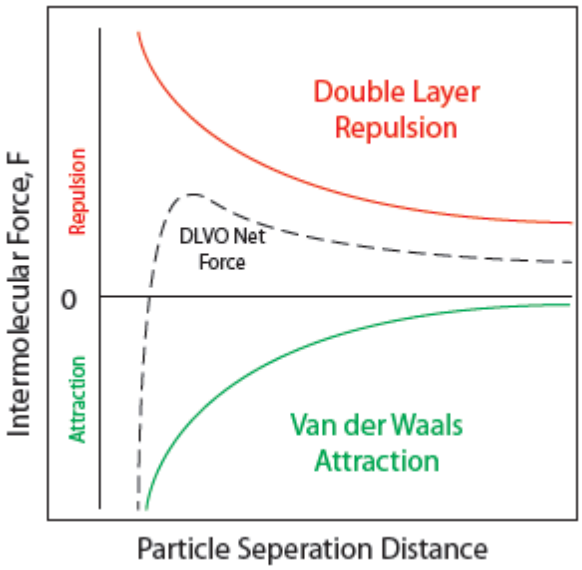

Figure 2: A DLVO curve representing the intermolecular interaction balance of van der Waals attraction and EDL repulsion to show the net behaviour of interacting particles.

Figure 2 shows that there are two minimums on the DLVO curve. The maximum potential representing the energy barrier is a function of the concentration of electrolytes within an aqueous solution, where higher electrolyte concentrations reduce the maximum potential. In some cases, DLVO theory does not apply due to a combination of other very strong short-range forces (i.e. steric or hydration forces) that can exist outside of a liquid environment and influence solid-solid interactions. Steric repulsion results from surfaces possessing molecular chains that physically resist overlapping as a consequence of their physical size, structure, composition, or molecular characteristics.

Thermodynamic Principles of Wetting

In 1805, Thomas Young and Pierre Simon showed that an interface has a specific energy that is proportional to the number of molecules present, or the surface area of that interface [28]. This is why droplets to be spherical when suspended (minimizing the surface area), and why liquids will tend to maintain this shape when in contact with a non-wetting solid against the influence of gravity flattening the droplet. The free energy of a material is based on the energy that is either created or lost with the change of surface area of a material, and is defined as $\boldsymbol{\gamma = \delta E/\delta A\ (J/m^2)}$. However, when referring to liquids, it is

common to refer to the surface tension of a material which is a linear force that is defined by the tension per unit length of a material and is expressed in the equivalent unit of **N/m**. Surface tension is a force that resists the compression of the liquid at the surface, and can be observed in the ability of some objects to float in water even though they are more dense. This is due to the amount of energy that would be expended if the surface was to be expanded through the breaking of the cohesive attractive forces within the water to accommodate the area of the object. Cohesion refers to the work required to separate a unit area of material to generate new surfaces and is defined by; $\mathbf{W_{\alpha\alpha} = 2\gamma_{\alpha}}$, where γ_{α} refers to the surface tension of material α. Conversely, the work required to separate an interface of two materials to an infinite separation distance within a vacuum while creating new surfaces is defined as the work of adhesion; $\mathbf{W_{\alpha\beta} = \gamma_{\alpha} + \gamma_{\beta} - \gamma_{\alpha\beta}}$. The work of adhesion is a useful quantity because it distinguishes two states of contact and separation, and can be thought of as the generation of a unit area of surfaces α and β with the loss of the interfacial area. Figure 3 visualizes this relationship.

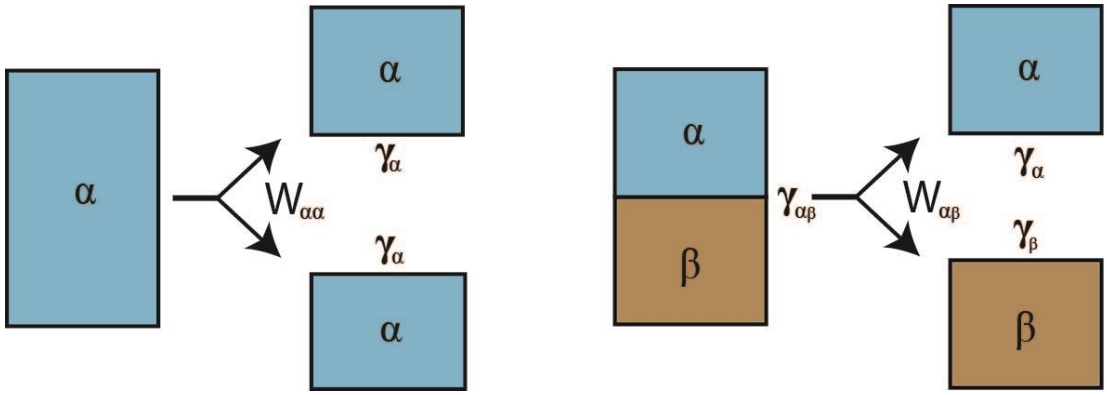

Figure 3: A schematic outlining of the work of cohesion versus adhesion

The interfacial energy is defined by the free energy required to promote a change of area for two materials when they are removed from contact, which can be found with the summation of the resulting surface tensions minus the interacting surface tension.

The equilibrium wetting behaviour and properties of a liquid on a solid substrate is related to the molecular interaction of the materials involved, which can be simplified by the Lennard-Jones equation modelling the interaction of two neutral bodies;

$$\boldsymbol{\omega(r) = 4\varepsilon \left\{ \left(\frac{\sigma}{r}\right)^{12} - \left(\frac{\sigma}{r}\right)^{6} \right\}}$$

This relations describes the short-range repulsion and attraction components of the interaction where, ε represents the depth of the potential well, σ is the finite distance to the inter-atomic potential becoming zero, and *r* is the distance to the potential maximum. This model generates the general understanding of inter-atomic interaction, where a force of attraction will exist that is inversely proportional to the distance

separating the atoms until a maximum attraction well observed before quickly experiencing a strong repulsive force as the particles begin to interact electronically.

Hydrophobicity - Wetting Interaction at the Solid Interface

Hydrophobicity is a measure of the interaction of water and a material at the interface, where hydrophobic materials are defined by a poor interaction with water in contrast to hydrophilic materials that have strong interaction ability. The behaviour of this interaction is referred to as wetting, and is observed in the ability of a liquid to establish contact based on the intermolecular interactions at the interface. The degree of wetting observed is a result of the force balance between the intermolecular adhesion and cohesion forces as outlined in Figure 3. Adhesion forces act at the interface between the liquid and solid, and will cause the droplet to spread out over a surface as the adhesion pulls the liquid. Cohesive forces act within the bulk liquid and cause the droplet to ball up on the surface as the water wants to minimize the interfacial surface area. Table 1 outlines the resulting contact angle from the intermolecular forces acting on the system as adapted from the work of Dr. Quéré [18].

Table 1: An outline of the intermolecular forces playing on a liquid droplet and the subsequent contact angle observed from the interaction [2]

Contact Angle	**Wetting State**	**Interaction Strength**	
		Solid-Liquid	**Liquid-Liquid**
$\theta = 0°$	Complete	Strong	Weak
$0° < \theta < 90°$	High	Strong	Weak
$90° \leq \theta \leq 180°$	Low	Weak	Strong
$\theta = 180°$	Non-	Weak	Strong

The point of contact is measured at the three-phase line where the liquid droplet is confined within the area defined by the three-phase line where the contact line of the liquid and solid is also in contact with the atmosphere. Young's relation is derived from the force balance at a liquid-liquid interface, where some simple assumptions result in the way to calculate the contact angle. All of the thermodynamic equations stated, and the following derivations are under the assumption of ideal conditions where any solid interface is represented by an atomically smooth surface, the solid materials are infinitely rigid, and the interface possesses complete chemical homogeneity. In reality, it is almost impossible to generate a perfectly smooth surface and non-ideal contact occurs very easily.

Solid-Liquid Contact

Under the assumption of ideal conditions, the droplet's interaction with the solid interface should yield a single and equal contact angle [7]. The contact angle is the angle between the liquid-gas and solid-liquid interface as defined by θ_C in Figure 4-a. As a liquid droplet of a defined volume spreads further onto a surface, the contact angle will decrease as the area of the solid-liquid interface increases, serving as an inverse measure of the wettability of a surface.

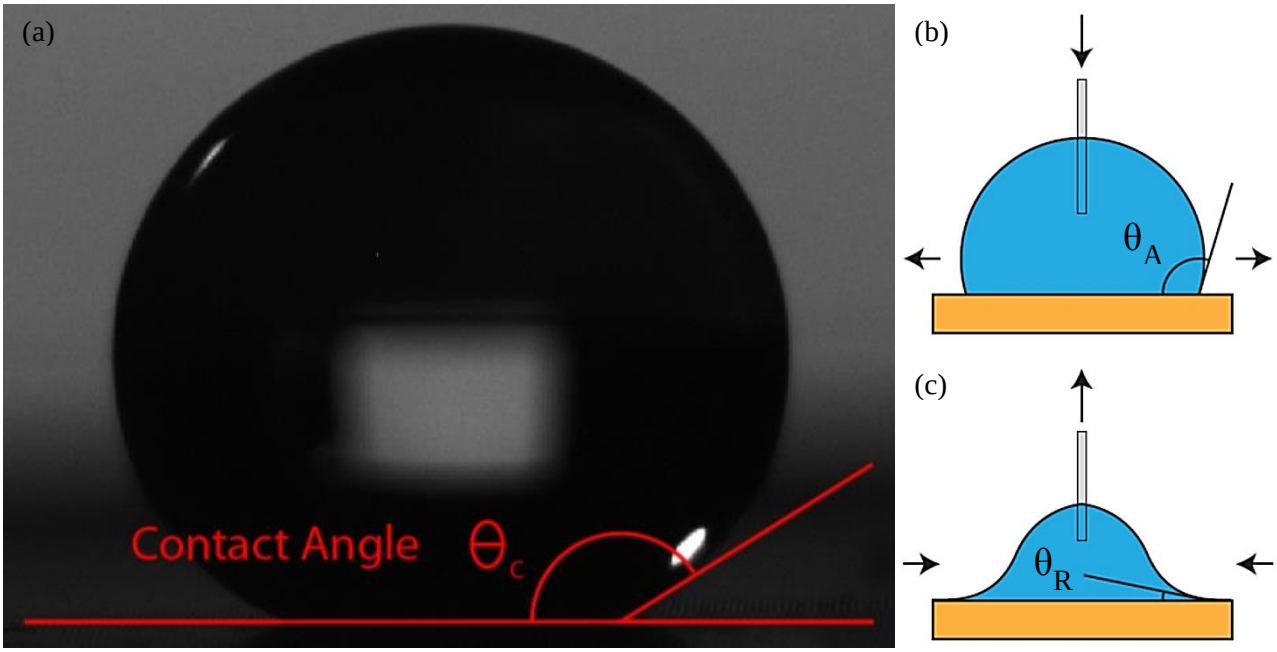

Figure 4: Illustration of how the contact angle is calculated as part of (a) a standard Sessile contact angle test, and (b) the advancing contact angle as the droplet expands and water is injected opposite to (c) the receding contact angle as water is drawn back into the syringe

Typically surfaces with water contact angles greater than 90° are considered to be hydrophobic. Conversely, surfaces with water contact angles less than 90° are considered hydrophilic and will favour the spread of water over the surface. The definition of superhydrophobicity is generally considered to categorize surfaces with a water contact angle greater than 150° which shows very minimal solid-liquid interaction, although more recently superhydrophobic surfaces have also been defined by possessing a low contact angle hysteresis. The contact angle hysteresis shown in Figure 4-a,b represents the ability of a liquid to act dynamically with the surface given a non-equilibrium state, and is derived from non-idealities present at the solid-liquid interface. Contact angle hysteresis is defined as the difference between the advancing, θ_A, and receding, θ_R. There are three identified sources for the contact angle hysteresis; i) surface roughness is able to trap or impede the triple-phase line from moving along the surface, ii) chemical contaminations the disrupt the solid surface, and iii) solutes within the liquid may deposit back onto the surface. Looking at these potential causes and the dynamic molecular state of a

liquid, we observe the thermodynamically irreversible nature of surface alterations resulting from the solid-liquid contact prevents the retreating liquid from following the same path due to the metastable reorientation of the liquid molecules. Typical solids are heterogeneous on micro-scale, where glass is close to an ideal surface with a roughness amplitude of about 0.5nm, and contaminates that are brought by air to the surface are usually on the submicron level due to the colloidal limit of floating particles [29]. The presence of these heterogeneities or imperfections will affect the value of the contact angle as the contact line by interacting with the different defects that can pin the droplet edges and produce a range of different contact angles [30]. Pinning may also result from the swelling of a polymer at the interface while in contact with a soluble liquid following a prolonged exposure to a droplet.

In real systems, calculation of the contact angle hysteresis is a difficult problem due to the surface variations and defects apparent. However, it is the hysteresis pins the contact line and generates the variability of the contact angle [12]. As a practical consequence of this, we are able to observe the ability of droplets to stick to inclined surfaces and resist the pull of gravity. This is an important consideration for surfaces desired to mimic the ability of a lotus leaf and remove droplets given a slight incline. Within different applications, both low and high hysteresis values are able to be applied to different surfaces to achieve specific results. However, to take advantage of the lotus effect on an anti-wetting surface, low hysteresis values are required. Conversely anti-fogging surfaces take advantage of high adhesion with a high hysteresis value to prevent the droplets from rolling or spreading on a surface following condensation. Both high and low hysteresis values are observed within nature in plants and vegetation, each with a specific purpose to suit the evolutionary needs and ultimately benefit the species [12]. Low hysteresis values have also been identified as the determining factor of the icephobic potential of a surface rather than the contact angle [17].

The contact angle hysteresis can be measured through several different procedures, which includes: i) the most common means to quantify the contact angle hysteresis is dynamic contact angle testing which involves the slow injection of water onto a substrate where the angle can be observed to increase as the volume increases due to the contact line being pinned as shown in Figure 4-b. There is a critical volume that the droplet will achieve before the contact line will suddenly jump, and the largest static contact angle value before this jump is labelled as the advancing contact angle, θ_A. Conversely, the removal of water from the droplet allows us to observe the smallest contact angle before the contact line recedes as shown in Figure 4-c, presenting the receding contact angle, θ_R. The difference between the advancing and receding contact angles is the magnitude of the contact angle hysteresis; ii) measuring the contact angle of the droplet as the solid surface is tilted until the droplet begins to roll from the surface and defining the leading and trailing edge contact angles, and; iii) through measuring the contact angles as the droplet is moved on the surface using the tip of a syringe.

Equilibrium Wetting Conditions - Young's Law

The contact angle observed in Figure 4-a is the apparent contact angle of a real system, where the ideal conditions of chemical homogeneity, rigidity, and a perfect smoothness are all meant to establish a thermodynamically stable environment. However, imperfections are inherent within any physical system, and therefore the observed contact angle is only the apparent value of the true contact angle which can be determined through rigorous thermodynamic calculation. Young's Law is derived from a force balance equation that represents the minimization of energy at the three-phase point. Figure 5 indicates the three-phase point in a three fluid system.

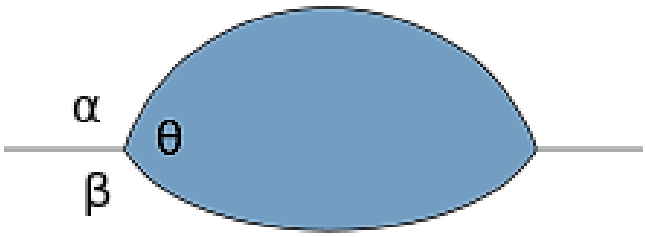

Figure 5: The interaction of a three-fluid system, with the three-phase point of mutual contact is positioned where the phases α, β, and θ meet

In this scenario there are three phases present, and therefore there will be three interacting surface tension forces that need to be considered. At equilibrium, the net force per unit length acting on the boundary line between the separate phases is equal to zero, where each force is based on the surface energy possessed at the interface of each material. This becomes;

$$\gamma_{\alpha\theta}\cos(\theta) + \gamma_{\theta\beta} + \gamma_{\alpha\beta}\cos(\beta) = 0$$

where α, β, and θ are the three angles observed in each phase, and γ_{ij} represents the surface energy between the two phases *i* and *j*. Regarding in a liquid-solid contact scenario, the phase α becomes the atmosphere, β is the solid, and θ is now the liquid, where the contact angle is represented by the interior angle of the liquid phase, θ. For our purpose, we replace the solid-phase with a flat solid material, where the Young equation makes the assumption of a flat and rigid surface and β then becomes equal to 180°. This simplifies the net-force equation to Young's equation that relates the equilibrium contact angle and the three surface tensions;

$$\gamma_{\theta\alpha}\cos(\theta) + \gamma_{\beta\theta} + \gamma_{\beta\alpha}\cos(\pi) = 0$$

$$\gamma_{\theta\alpha}\cos(\theta) + \gamma_{\beta\theta} = \gamma_{\beta\alpha}$$

which can be represented by the redrawn three-phase point diagram in Figure 6;

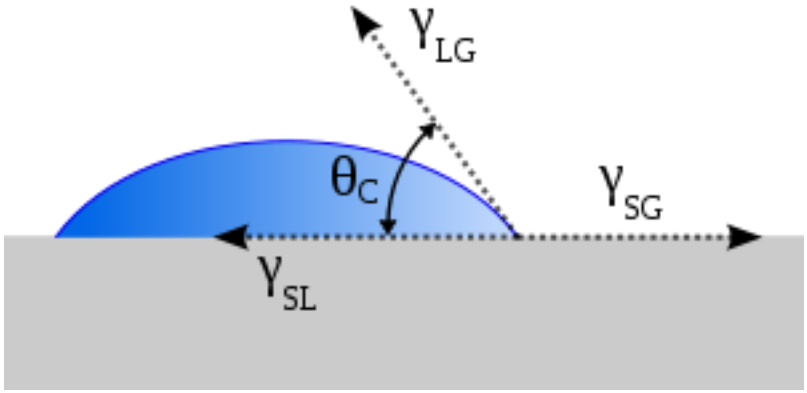

Figure 6: The typical schematic set-up of the three-phase point to display the interacting forces, which are equal to zero when the liquid phase is at rest on the solid surface

The three surface tensions are defined when the phases achieve equilibrium with each other maintaining a force balance. This relation between the three-phases is able to be used to predict the contact angle of a liquid droplet on a solid surface if the three surface energies are known. Conversely, by observing the contact angle, and with the surface energy of both water and ambient atmosphere relatively well known, we are able to predict the surface energy of a solid material.

Based on the vector forces within the Young model, we know that neither γ_{SG} nor γ_{SL} are able to be larger than the sum of the other two surface energies. In looking at the vectors involved within this system, in order to achieve a complete wetting state, the restriction based on the physical system has to be overcome where $\boldsymbol{\gamma_{SG} > \gamma_{SL} + \gamma_{LG}}$. Likewise, to achieve a completely non-wetting surface; $\boldsymbol{\gamma_{SL} > \gamma_{SG} + \gamma_{LG}}$. This lack of solution indicates that there is no way for a droplet to achieve a complete wetting and non-wetting state at equilibrium. However, any combination of surface energies that fulfills the requirements will yield a contact angle between 0 and 180° at an equilibrium state. Looking further into the wetting conditions, we are able to define the spreading parameter, *S*, to gauge the wetting ability of a surface in the intermittent time before a surface is able to reach an equilibrium state;

$$S = \gamma_{SG} - (\gamma_{SL} + \gamma_{LG})$$

This equation can be derived from either observing the vector interactions, or by looking at the difference in the work of adhesion to the solid interface from the work of cohesion within a liquid droplet in a vacuum state;

$$S = W_{\alpha\beta} - W_{\beta\beta}$$

A positive spreading coefficient indicates a surface that will wet completely with liquid, and a negative spreading indicates that the surface will only partially wet. The spreading coefficient is the primary descriptor of the dynamic wetting system, and indicates if a droplet will continue to spread while in

contact with a surface. Inputting the spreading factor into the Young equation, we are able to define the Young-Dupré relation;

$$S = \gamma_{LG}(\cos\theta - 1)$$

which can be used to solve for the spreading coefficient given that the contact angle is restricted to values between 0 and 180° producing a spreading coefficient less than zero. With the spreading coefficient, Figure 7 shows the three possible wetting states that can exist within any three phase system.

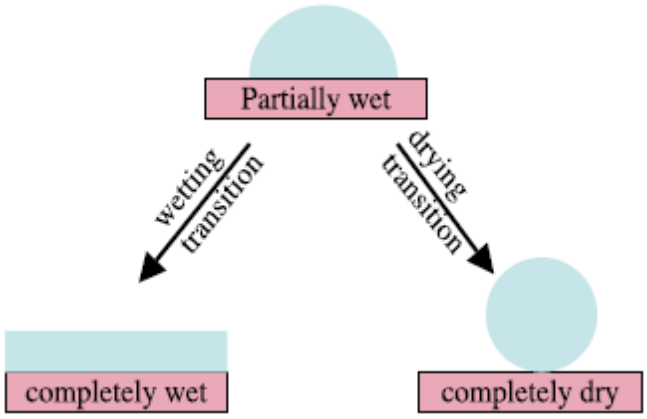

Figure 7: The three potential wetting states as predicted by the Young-Dupré relation [31]

In the complete drying state, a macroscopic vapour layer would form between the solid and liquid phases, although the non-wetting aspect of the surface does not necessarily indicate the evaporation of the liquid to a vapour phase. However, the van der Waals forces between the surface and the hypothetical vapour layer tend to spread the vapour too thin, and prevent any complete barrier from forming and causing the surface to be completely dry [32]. Opposite to this effect, a completely wetting surface will constantly spread the liquid over the solid surface until the layer achieves it minimum thickness as defined by the interactive van der Waals forces, although the stabilizing short-range forces decay exponentially over the nano-scale.

The most common case is a partial wetting state, where both the physical and chemical properties of the surface will impact the observed contact angle and wetting state of the material. Partial wet surfaces are a result of a droplet that is surrounded at the three-phase contact line by a microscopically thin-film layer adsorbed at the interface. The film layer at the interface is in thermodynamic equilibrium, where the entropy gained from the adsorption of the molecules and the average thickness of the interfacial film varies from a fraction of a water molecule to several water molecules thick based on the affinity of the vapour molecules to the substrate surface [33]. Complete wetting systems possess a macroscopically thick wetting layer at the three-phase contact line, where the equilibrium spreading coefficient is zero. This results in a solid-vapour interface that consists of the macroscopically thick wetting layer so that the surface tension is equal to the sum of the solid-liquid and liquid-vapour interfaces.

Enhancing Wetting Properties - Physical Modification

The presence of asperities or structures on the surface of a material modifies the observed wetting properties dramatically and can be used to control the behaviour of a surface with different liquids. When a droplet is much larger than the surface asperities, the roughness of the surface will affect the interaction with a finite droplet at the interface to reflect the average properties of the substrate. Surface patterning occurs both naturally and by design in order to alter and control the wetting properties of a surface, where a rough surface projects a greater surface area versus an equivalent projection that is molecularly smooth. The minimization of free energy leads to an effective contact angle within this area reflective of the direct difference in the ratio of the real contact area to the macroscopically observed contact area. The Wenzel equation has been developed to account for the extra area of the drop that is in contact with the solid surface to determine the adjusted equilibrium contact angle, θ_W, from the intrinsic contact angle value, θ_C, with ideal conditions;

$$\boldsymbol{\cos(\theta_W) = r * \cos(\theta_C)}$$

In this equation, *r* is the ratio of the real to the projected area at the liquid-solid interface, where the real area of contact is always greater than the projected area of a smooth surface; $\boldsymbol{r > 1}$. It is important to note that hydrophobic contact angles are predicted to increase with a greater roughness, whereas hydrophilic contact angles are predicted to decrease. Therefore, you are able to tune the contact angle of an interface with a defined surface energy through adjusting the surface roughness as shown in Figure 8. The Wenzel equation makes the important assumption that the liquid will be in conformal contact over the entire real contact area, where for many surfaces this is not the case. The effect of roughness in conjunction with a chemically hydrophobic surface can lead to superhydrophobicity, where water can achieve contact angles close to 180°. Under static conditions, the three-phase line will locate itself at some surface asperities, where small liquid masses are able to be completely pinned at these irregularities, where if the asperities are adequately small (<< 1μm) the contact line places its advancing front to the location with the lowest possible free-energy [34]. The reorientation of the solid-liquid interface leads to a new thermodynamic equilibrium state with an adjusted contact angle from what would be observed on a smooth surface.

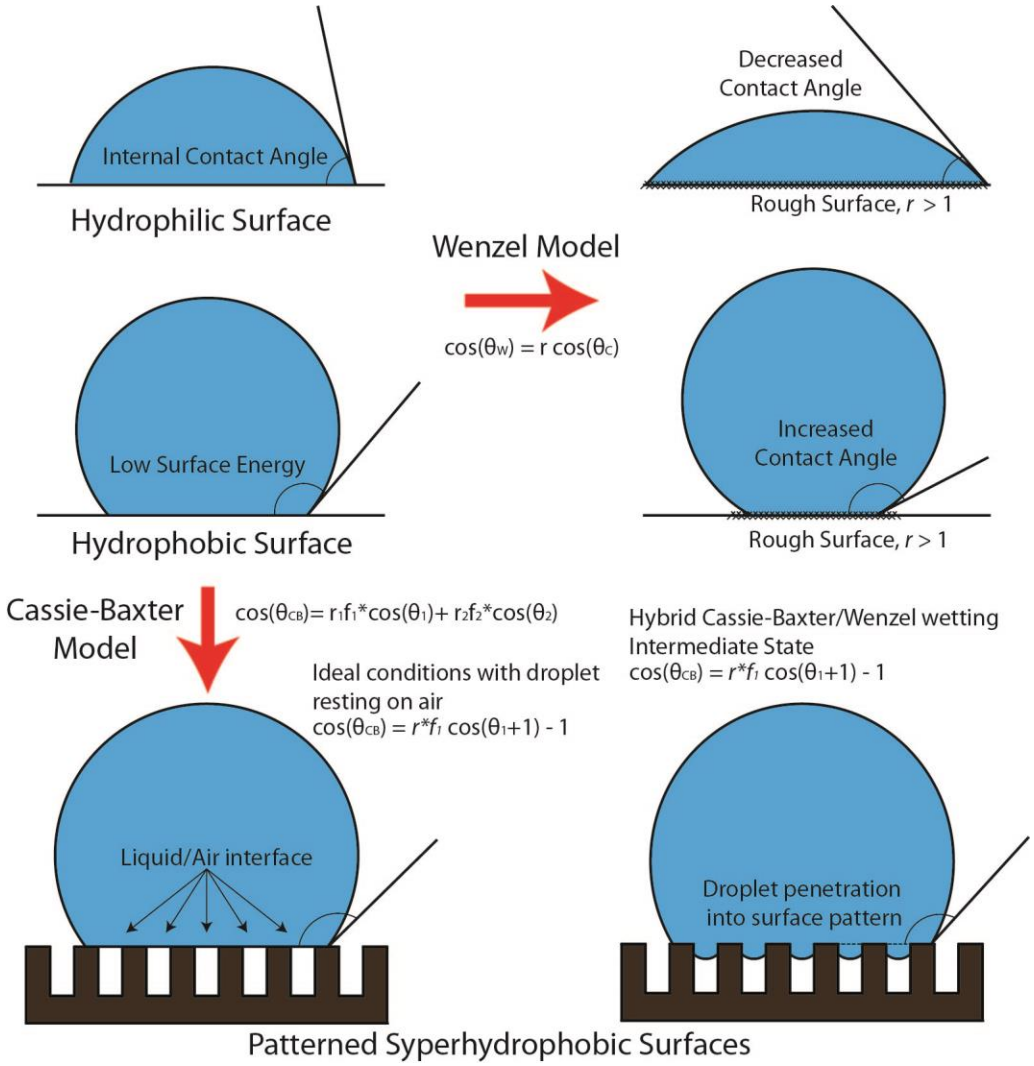

Figure 8: The effect of surface patterns on the thermodynamically ideal contact angle via both the Wenzel and Cassie-Baxter wetting mechanisms. Image adapted from previous wetting study [35]

Moving away from the more ideal Wenzel equation, Cassie and Baxter derived a means to take into account surfaces that do not possess either chemical homogeneity, or time-dependence from the rearrangement of the interacting molecules. Non-uniform surface conditions leads to the reordering and dynamic restructuring of the molecules within the system to minimize the free-energy of the interaction. Additionally, direct exposure to different mediums will lead to the rearranging of the materials in order to minimize the free-energy at the interface, where for instance the polarity of a liquid exposed to a surface will lead to restructuring at the interface. For example, more polar side-groups or block components of a polymer chain will be buried within the bulk structure if exposed to non-polar liquids and vice-versa. Cassie and Baxter reported a similar calculation of the bulk contact angle to Wenzel's original prediction for heterogeneous solid systems, where both the roughness, *r*, and the fraction of multiple surfaces over the interface, *f*, will affect the resulting adjusted contact angle [36];

$$\cos(\theta_{CB}) = r_1 f_1 * \cos(\theta_1) + r_2 f_2 * \cos(\theta_2)$$

When surfaces possess asperities that are packed densely or have a high aspect-ratio, droplets are observed to sit on top of the structures. This is due to the surface tension of the liquid phase preventing the droplet from penetrating the textured surface and achieving complete conformal contact with the entire real contact area. This mode of contact is referred to as laid-contact, or a non-conformal contact state, which can alter the observed properties of the surface, and in some cases cause for hydrophilic materials to become hydrophobic following the application of a pattern. Trapping of air leads to what is called the *fakir effect*, where air is trapped underneath the droplet sitting on the extremities of the surface protrusions as visualized in Figure 8 for the patterned superhydrophobic surfaces [37]. Taking the relationship proposed by Cassie and Baxter a little further to incorporate the air trapped beneath the droplet at the interface with a contact angle of 180°, we are able to adjust the above formula for a single homogeneous material where the droplet is also sitting on air to;

$$\cos(\theta_{CB}) = f * \cos(\theta_C + 1) - 1$$

With this modified formula, *f* refers to the fraction of the interface that is in contact with the solid material ultimately resulting in the adjusted Cassie-Baxter contact angle, θ_{CB}. Within real systems under non-ideal conditions, the mode of contact is not analog, and could be considered as a hybrid between laid and conformal contact. In this case, a combination of both Wenzel and the Cassie Baxter wetting mechanisms has been proposed to predict the resting contact angle at equilibrium for liquids that sit both on trapped air and in conformal contact with rough surfaces [37], [38];

$$\cos(\theta_{W/CB}) = r(f_1 \cos(\theta_1) - f_2$$

Under the condition where the liquid phase is in contact with more than one material at the interface and there exists chemical heterogeneity on the surface, the spreading coefficient varies depending on the local position. The resulting adjusted contact angle is given a value depending on the average value of the materials present at the interface. The Cassie-Baxter equation can be adjusted to include the average spreading coefficient of the materials at the chemically heterogeneous interface based on the fraction of each material and their respective surface energy at the interface;

$$(-1 - \cos(\theta_{CB}) = -S$$

Solid-Solid Contact and Interaction - Tribology

Under the condition of an ideal contact, a solid-solid interface is generated under the assumption that the surfaces are atomically smooth, are rigid, possess chemical homogeneity, and there is no energy lost through elastic dissipation. Using the Hamaker theory, the total Van der Waals force interactions between two bodies can be summed, where the attraction between every atomic pair at the interface can be integrated into an approximate total force of adhesion. Between two macroscopic bodies, the

relationship of van der Waals attraction to distance depends on the geometry of the interaction. For two flat plates, the overall work of adhesion from the van der Waals interaction is equal to $\mathbf{W_A(D) = -H/12\pi D^2}$, which is a function of the separating distance D and the Hamaker parameter, H. However, as two parallel plates offers a very difficult experimental setup to replicate, the Derjaguin approximation can be used to transform this interaction to that between two ideal rigid and homogeneous spherical solids when D is much less than the radii of the spheres involved, R_1 and R_2;

$$F(D) = 2\pi\left(\frac{R_1 R_2}{R_1 + R_2}\right) W_{12}$$

The value of the Hamaker constant depends on the chemical nature of the molecule or surfaces; it is in the order of magnitude of 10^{-20} J in air and 10^{-21} J in water. Because of the universal van der Waals interactions and the predominately attractive forces, when two smooth polymer surfaces approach each other to a distance within a few nanometers, they jump into contact.

Hertz Non-Adhesive Elastic Contact

The Hertz theory of adhesion is built from approximating an ideal system, although the observed non-idealities of any two solids in close proximity was always present. This value is able to estimate the interaction between two identical solid spheres in vacuum, although non-ideal conditions such as elasticity and energy dissipation must be taken into account in any real system. Non-adhesive contact was observed almost 300 years ago by Newton when pressing two glass plates together and observing the diffracting light around a single spot that was created upon contact. However, Hertz was able to correlate the applied load for contact of two spherical surfaces to the resulting contact area [20], [39];

$$F = \frac{K\, a^3}{R}$$

The magnitude of the applied load, *F*, is found given the radius of the contact area, *a*, the reduced modulus, *K*, and the combined radius of the interacting spheres as defined by $\mathbf{R = R_1R_2/(R_1+R_2)}$. The reduced modulus is the combined Young's modulus of two interacting solid bodies;

$$\frac{1}{K} = \frac{3}{4}\left[\left(\frac{1 - v_1^2}{E_1}\right) + \left(\frac{1 - v_2^2}{E_2}\right)\right]$$

with the values of the elastic modulus, E, and the associated Poisson's ratios, *v*. With the Hertzian model, it is assumed that any strains incorporated into the system are small and within the elastic limit, that the area of contact is less than the characteristic radius of the interacting bodies, and that the surfaces are smooth and frictionless.

Adhesive and Anti-Adhesive Mechanisms

There are many instances in nature where different species take advantage of either high- or low-adhesion surfaces to optimize their performance and ability to survive under specific conditions or situations. The adhesion observed for surfaces is often related to the temperature, and the rate-dependent thermo-physical properties of the materials in contact, where the bodies will store elastic energy when brought into physical contact [40], [41], [42]. This stored elastic energy is also able to be dissipated through other mechanisms including viscoelasticity, plastic deformation, and friction to name a few. As the materials are separated, the stored elastic energy of the materials can dissipate in crack growth at the interface. Thus, if a material is able to store this elastic energy within its bulk, it can be expected that it will have greater adhesive properties which is generally the case for softer materials. There are two criteria outlined for materials that have a strong adhesion. First is the maximization of the real area of contact, and second is the existence of long dissipative bonds at the interface [43]. Long dissipative bonds should be present at the interface to ensure that any elastic energy dissipated by the bulk during separation through the elongation of the interfacial bonds. During separation of two solids, the stored elastic energy is the main driving force at the interface, where energy is required in order to create the new area formed (see adhesion energy above). Therefore, as energy is required to generate new area, maximizing the real area of contact would mean that more energy is required to completely separate the two surfaces. Conversely, it is this roughness that is the reasoning why macroscopic particles usually do not adhere to one another, as two hard surfaces will result in minimal potential contact area as shown in Figure 9-top. However, Figure 9 displays two different means to increase the adhesion at the interface, where if one material is soft as in the bottom image, it is able to better conform to the hard surface and increase the amount of real contact area. Moreover, the presence of a liquid at the interface as in the top image is common in many biological systems, and increases the likelihood of capillary interactions between the surfaces at the interface enhancing the overall adhesion [44].

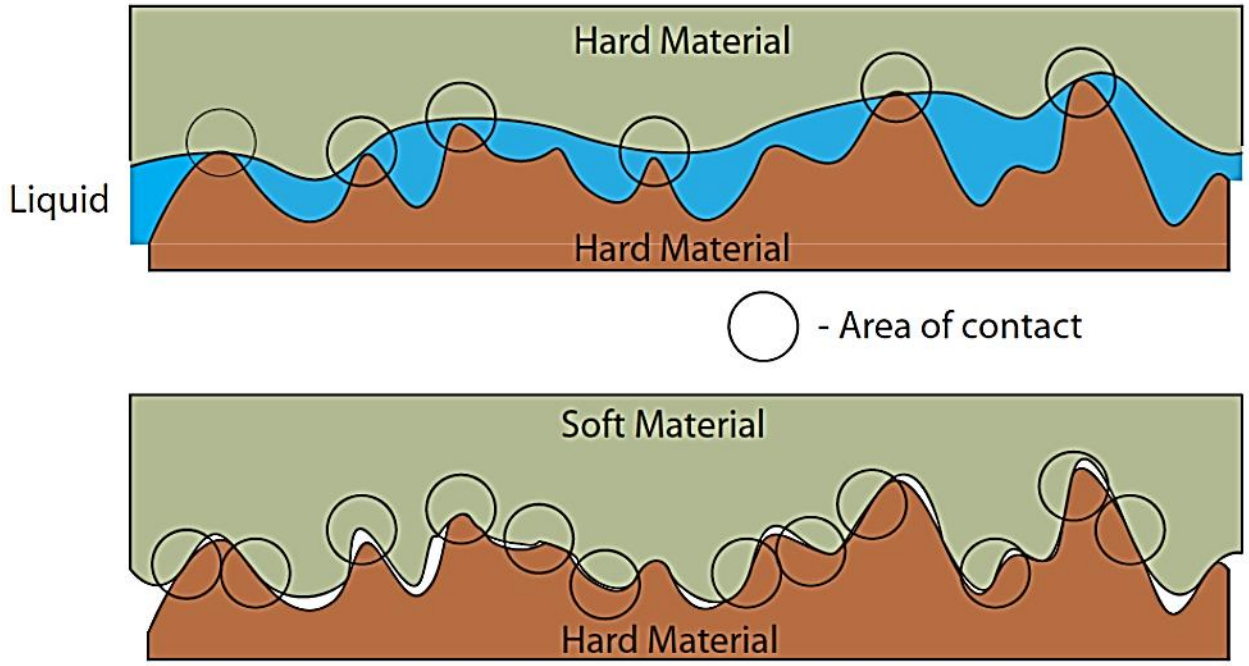

Figure 9: The interaction of two hard surfaces (top) leads to a reduction of the real area of contact and therefore the adhesion experienced, whereas the introduction of a softer material better able to conform to the hard surface, and a liquid introducing capillary interactions will increase the adhesion experienced between hard materials

Capillary interactions result from water condensing into the gaps of neighbouring surfaces forming a water meniscus under ambient conditions. A classic example of capillary forces at work can be illustrated with the construction of sandcastles using damp sand, where it is impossible to form any structure with either dry sand or underwater. A structure of damp sand takes advantage of capillary forces that cause a film of water to adhere the particles together. Capillary forces normally consist of three contributions: (1) the Laplace pressure contribution due to the existence of meniscus; (2) the division of surface tension of water in the direction normal to the surfaces, which value depends on the contact angles and is always small compared to the Laplace pressure contribution for small contact angels; and (3) if the two surfaces are in direct contact, the adhesion force due to the van der Waals attractions should also be taken into account.

Opposite to the increase of adhesion, many plants, animals, and insects benefit from the ability to reduce the adhesion experienced when in contact with different surfaces. This is primarily achieved by reducing the real area of contact between the mating surfaces, and the introduction of repellent surface chemicals or coatings.

Dry-Friction Behaviour and Mechanism

When dealing with classical friction, Amontons' Law of Friction generates a linear relationship with the force of friction proportional to the normal load; $\boldsymbol{F_X} = \mu * \boldsymbol{F_Z}$, where μ is the coefficient of

friction that is unique for every interaction [37], [45]. However, this relation was expanded upon when Bowden and Tabor found that there was still some observable friction force even at zero normal loads. This finding was attributed to the existence of intermolecular forces at the near interface, and an additional term be added to the then current understanding of friction to incorporate the interaction at the molecular real area of contact; $\boldsymbol{F_X = A * S_C}$, where S_C is the shear stress between the two surfaces, and the contact area, A. The contact area is dependent on the normal load as described by either the Hertz model for non-adhesive contact (Figure 9-top) or the JKR (Johnson, Kendall, and Roberts) model for adhesive dependent contact (Figure 9-bottom without the liquid). The classical JKR theory relates a loading force to substrate deformation, elastic modulus, and surface energy. The expanded relation applies within situations where the normal load, F_Z, is extremely small. This was followed with work by Homola and Israelchvili who proposed the generalized Amontons' Law as; $\boldsymbol{F_X = \mu * F_Z + A * S_C}$. This model serves to emphasize the role that the normal load plays with the resulting friction, where at normal loads greater than the adhesive forces between the surfaces the classical Amontons' Law will dominate the term. Conversely, the friction will be dominated by the interfacial interactions at a smaller preload force. As a result, at preloads around the adhesive force of the interface, the friction will not follow the classical linear trend relative to the loading force. In Hertizian contact, the relation is $\boldsymbol{F_X \propto F_Z^{2/3}}$, and for the JKR mechanism of contact, F_X would follow the dependence of the real area of contact on the applied load.

Current Icephobic Research

The effect of the accumulation of ice or wet-snow on surfaces is a well-defined problem within cold-climate regions, and causes many issues with infrastructure damage and money invested [46]. Atmospheric icing is the primary contributor to this accumulation, which is a result of super-cooled droplets coming into contact with a surface, and freezing on contact. Various means to control, limit, or eliminate the ability of ice to adhere to surfaces have been trialed, where both active (de-icing involving the input of energy) and passive (anti-icing preventing the formation of ice without the expenditure of energy) methods are currently used. Passive anti-icing coatings serve to delay the formation or the overall ability of ice to adhere to a surface, ultimately decreasing the overall accumulation of ice on a surface [14], [16], [17], [46], [47], [48], [49]. One approach to icephobic surfaces is the use of superhydrophobic surfaces to decrease the ability of water to remain on a surface. Additionally, delaying the freezing transition, or decreasing the observed ice-adhesion once ice or snow accumulates on the surface would lead to decreased accumulation.

Superhydrophobic Surfaces as an Icephobic Approach

In looking towards superhydrophobic solutions for icephobic applications, an easy connection is made between the real contact area and the ice-adhesion strength, as the primary physical mechanism for decreased ice-adhesion strength is the decreased real area of contact at the liquid-solid interface. Therefore the ability of water to remain on top of the structures without penetrating the surface is paramount to ensure icephobicity. A good measure of the real contact area is the resulting contact angle that is measured for equal volume droplets. However, the hysteresis has also been linked to the adhesive ability of water droplets, where the hysteresis can be described as the measure of energy dissipation during the flow of the droplet, and a low hysteresis implies low adhesive ability [12]. The adhesion of a liquid droplet can be tied to physical variables like the pitch between the structures on the surface, the height of asperities, and the density of the structures. From studying two contrasting rose samples, one with high adhesion and one with low, Bhushan et al. found that a smaller pitch value and greater height resulted in low adhesion surfaces. Even though both surfaces displayed contact angles greater than 150°, it was theorized that the difference in adhesion was a result of the ratio of pitch to height, which is responsible for the level of Cassie-Baxter regime wetting observed minimizing the area of real contact. However, the epoxy pillars fabricated indicate that there is also a large role played by the solid interface and the chemical contribution to hydrophobicity. The pillar array dimensions are very close to those described for the dried low-adhesion Bairage Rose leaves [12], although the wetting properties of the epoxy micro-structures resembled the more adhesive rose sample. The study of contrasting rose samples also looked into the role of the surface waxing on the resulting hydrophobicity, where it was found that surfaces with a greater density of asperities were less impacted by the addition of nanoscale wax crystals. In fact, the less dense the surface structures, the more dependent the surface was on the amount of wax added to promote the hierarchical structures that are responsible for the superhydrophobic behaviours of increasing contact angle and decreasing contact angle hysteresis. This matches well with the observations performed with the epoxy micro-structures, because even though the surface resembled the low-adhesion surface, the hydrophilic nature of the epoxy material used led to a greater tendency to wet the entire surface and for the droplets to penetrate partially into the patterned surface. Therefore, even though the physical properties of the surface match well with the low-adhesion rose petal sample, the wetting nature of the epoxy results in a high-adhesion surface.

However, relating these findings back to an application focus, the primary issue addressed within this works, and a constant among many other icephobic studies, is the ability of surfaces to maintain their icephobic properties through several freezing and ice-removal cycles without degrading in performance. As superhydrophobic surfaces rely on a physical pattern to generate a Cassie-Baxter state of wetting, the destruction of the surface topography with the freezing of removal of ice or physical scratching is one of

the primary disadvantages to using nano-scale asperities to create an anti-icing superhydrophobic surface [50], [51], [52].

Work has been completed by Kulinich and Farzaneh from the University of Quebec to measure the adhesion strength of ice through employing fabricated glazed-ice surfaces on hydrophobic surfaces. Both the contact angle and hysteresis were observed, and a correlation was drawn to the bonding ability of the surface and the ice. From this work, it was shown that a correlation between contact angle and ice-adhesion is only valid for surfaces with low wetting hysteresis [47]. Furthermore, the contact angle hysteresis values when related to ice-adhesion were found to be more effective when skewed more towards the tendency of the surface roughness to peaks as opposed to valleys. The tendency towards more peaks on the surface results in less contact area between the water and solid during hysteresis testing. This trend carries into ice-adhesion strength testing where the hysteresis correlated well to the adhesion observed, while contact angles values were not a good trending variable. Additionally, it was observed that samples with low hysteresis accumulated ice at a greater rate than the low-adhesion high hysteresis surfaces with an equal surface energy.

There are many means to generate superhydrophobic surfaces, and therefore many potential ways to fabricate an icephobic interface. Farhadi et al. describe the various means trialed within their lab, where samples were prepared with polymeric-nanopowder dispersions spun coated onto surfaces, the application of a low surface energy fluoropolymer to a rough surface, sintered nanoparticles on a flat surface, and doped silica rubber particles dispersed on a surface. Each of these surfaces possessed a common initial contact angle value between 150 and 155° all with hysteresis values less than 7°. After condensing water onto each surface while they cooled, the layer of water predictably lowered the contact angle and increased the hysteresis, while the ice-adhesion strength increased. However, the amount that the ice-adhesion strength increased was found to be a function of the duration of condensation and the surface temperature. This brings a valid argument against the functionality of icephobic surfaces in humid environments where even superhydrophobic fluoropolymer surfaces will have some condensation on the surface. The collection of water within the rough networks will accelerates further water condensation. Many studies also agree that frosting or slight wetting resulting from condensation will decrease the icephobicity observed, and in some cases generate icephilic surfaces [53], [54].

The Mechanism of Freezing

Studies performed by Chatterji attempting to understand the effect of freezing water on the degradation and destruction of concrete at sub-zero temperatures have referenced the subtle variability of the specific volume of water with the temperature other than just at the phase-change crystallization of

water. It was found that the specific volume of water is minimized at 4°C, where any structure saturated with water at or near 4°C will become super-saturated as the temperature increases or decreases [55].

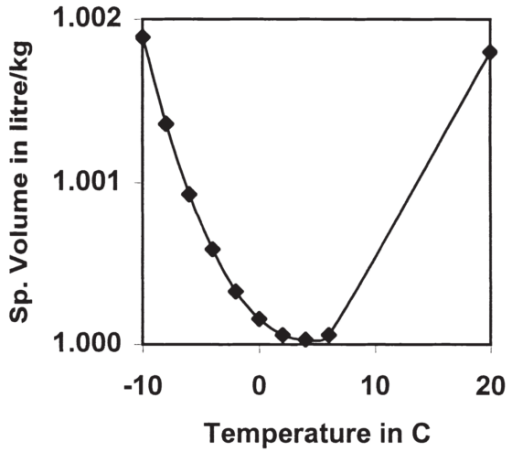

Figure 10: The specific volume of water as a function of temperature which shows the expansion of bulk water at higher temperatures, and in super-cooled conditions [55]

In looking at the rime-icing mechanism, cooling droplets coming into contact with the surface may lead to super-saturation as they expand and push excess water further into the structured surface leading to a hybrid or even Wenzel wetting mechanism. Water tends to freeze more quickly along the boundary interface resulting with the bulk water being enclosed within the ice-crystals and leading to crack formation as the core expands during the subsequent bulk phase change. The critical volume observed for crack formation as the core freezes is for enclosed volumes greater than 10mL [55].

The way in which ice freezes first on the liquid-air interface before the bulk leads to a characteristic peak observed for the droplet once it is completely frozen due to the pressure from the volume expansion. This may have a negative effect on a superhydrophobic surface that relies on the ability of surface asperities to reduce the total area of contact between the droplet and the solid material as the liquid freezes. If the liquid has a high affinity for the solid, the ability to re-establish contact with a larger real surface area or to embed itself into pores could lead to increased ice-adhesion strength.

Mechanical Properties of Ice

The study of ice friction has become a hot topic of late, where the underlying principles are still underdeveloped with several competing theories. Nonetheless, ice-friction plays a major role within cool climates where icing applications can have a large impact on safety, functionality, and the most studied field, sports. The existence of a liquid-like-layer (LLL) is paramount to the understanding of ice-friction, where the thickness of this layer defines which friction regime is present. Starting with thinnest to thickest: (i) dry friction is the absence of a lubricating layer, which cannot exist under atmospheric conditions where there will always be at least a molecularly thick LLL; (ii) boundary friction is defined

for situations with a molecularly thick LLL, where the contact zone has a temperature less than the melting temperature, and the thickness of the layer is less than the surface roughness. Typically the coefficient of friction within the regime is lower than that of dry-friction due to lubrication; (iii) mixed friction has a contact zone temperature greater than the melting point, although the characteristic roughness is still greater than the LLL thickness. Within this regime, the slider is partially in supported by the LLL, which reduces adhesion, although capillary bridges can lead to greater adhesion (see Figure 9); and (iv) hydrodynamic friction is described by the thickness of the layer being greater than the surface roughness and the contact zone temperature greater than the melting point. Here the LLL carries the sliding load, although greater applied loads can cause a transition back to the mixed regime. The friction is again defined by classical mechanics, where the surface area of the slider is the area of contact and the friction can be described as: $\boldsymbol{F_X = A * \tau_L}$, where τ_L is the shear-strength of the lubricating interface [56].

The LLL is a result of several mechanisms, although logic behind the existence of the LLL has not been agreed upon. Surface melting was the first proposed mechanism, and is based on a permanent existence of amorphous liquid at the surface of bulk ice. The bulk hexagonally packed structure of crystalline ice appears to break down at its surface, which may be due to the elastic energy stored within the structure [57] or due to the claim that the sum of free surface energy at the solid-vapour interface is greater than the combination of a solid-liquid and liquid-vapour interfaces [56]. In fact, it has been determined through extensive modelling that the molecular affinity for water molecules within a solid network varies greatly (from 53 to 18kJ/mol) on a perfect surface (and even more so on the layer just below the surface, 85 to 30kJ/mol) versus the average and approximately constant bulk affinity at just a few kJ/mol [57]. The high surface energy at the surface of ice is a consequence of the bulk molecules being able to easily form four hydrogen bonds (both donating and accepting), where the unfilled hydrogen bonds at the surface result in dangling hydroxyl groups that repel one another and electrostatically destabilize the surface. This energy instability results in an amorphous surface that generates the LLL observed. The second mechanism is pressure melting, where the pressure exerted on an ice surface will generate the LLL at temperatures close to the melting point. Although the effect of this mechanism was minimized through experimental studies that determined the extreme roughness of any real surfaces at an interface leads to pressure only being associated over a very small area. A third mechanism labelled as frictional heating was also proposed, where heat generated from the onset of friction results in the formation of a thicker LLL. Although the energy transfer is not ideal (there is some energy lost to material deformation at the interface), this mechanism is still considered to be the primary contributor of lowered friction values observed on ice [56]. A study performed by Colbeck et al. showed that only 0.005% of an ice skate is in contact with an ice surface, and therefore the contribution of both pressure melting and frictional heating is contained to a very specific area, increasing their effectiveness [58].

Chapter 3

Pattern Transfer of Biomimetic and Natural Structured Surfaces

This chapter discusses the different pattern transfer techniques that were developed to impart a defined structured pattern from one surface to another in order to mimic or create specific surface properties. There are two primary pattern transfer techniques that have been developed using a soft-lithographic approach to mimic a pattern from a variety of source substrates. The micro-patterned surfaces are characterized to gauge their potential within new applications that take advantage of the imparted superhydrophobic and friction tailoring abilities. The majority of the pattern transfer of the array of pillars to an epoxy substrate has been published[1].

The pattern transfer of a robust epoxy coating achieves several objectives with this work, where this procedure presents both a successful and repeatable process able to be carried out within a basic chemistry lab, and the process is able to be scaled up easily to large and complex coating applications. Figure 13 is the key reference for this work, providing a schematic outline of the two-stage transfer process that employs modified soft-lithography and moulding techniques. The pattern transfer process outlined in Figure 16 was developed to mimic Trembling Aspen leaf samples with the PDMS elastomer.

Soft Lithography

Soft-lithographic techniques are employed throughout this work, where the base materials are introduced to the mould or stamp before allowing them to cure into a solid patterned material. This process involves several physical properties that must be considered in order to ensure an accurate pattern transfer. During the moulding process, liquid precursors infiltrate the mould channels through capillary action, where the complete filling time, *t*, can be estimated with the equation;

$$t = \frac{2\eta_m h^2}{R\gamma_m cos\theta}$$

where η_m is the viscosity of the precursor, R is the hydraulic radius of the pores, γ_m is the surface tension of the precursor, and θ is the contact angle between the liquid and the surface of the mould channel [59]. A degassing process is applied before every curing step to remove air within the channels and speed up the filling process.

Once cured, the epoxy micro-pillar arrays are stable in air due to the high elastic modulus of the epoxy material, which is approximately 500MPa. The elastic modulus and strength of the epoxy material

[1] B. McDonald, H. Shahsavan, and B. Zhao, "Biomimetic Micro-Patterning of Epoxy Coatings for Enhanced Surface Hydrophobicity and Low Friction," *Macromolecular Materials and Engineering*, vol. 298, 2013.

is one limit to the potential aspect ratio of the material, where the critical height that can be obtained for the microstructures before they will begin to buckle under their own weight, h_c, is given by;

$$h_c = \left(\frac{0.49Ed^2}{\rho g}\right)^{\frac{1}{3}}$$

where ρ and E are the density and elastic modulus of the micro-pillar material. However, it has been proposed that attraction between separate pillars and between pillars and the substrate is what leads to observed pillar collapse mechanisms. The maximum achievable aspect ratios for each case are outlined within [60]. For a given aspect ratio and material, stability can be increased by either increasing the inter-pillar spacing or decreasing the surface energy of the pillars. Within these physical constraints and parameters, the initial SU-8 mould selected for replication of epoxy pillars is a hexagonal array with the dimensions of a 10μm diameter, a pillar height of 25μm, and a centre to centre spacing of 25μm between each structure.

PDMS has become a commonly used material in soft-lithography for its ability to pattern relief structures with feature sizes ranging from the nanoscale to a few centimeters using one of five typical techniques; microcontact printing, replica moulding, microtransfer moulding, micromoulding in capillaries, and solvent-assisted micromoulding [26]. In this work, a form of replica moulding is used to recreate the master mould pattern. The original pattern is either transferred onto different substrates or to different materials depending on the purpose of the procedure.

Transfer to Epoxy Substrate

The ability to pattern a substrate with an array of micro-pillars allows for a range of beneficial properties to be imparted to new and innovative applications. A facile pattern transfer process allowing the large scale application of a regular pattern of a robust epoxy material serves as a hydrophobic protective coating. The ability to transfer these patterns to a curved surface is the focus of this procedure and is the novel aspect that has been developed. To pattern a relatively large piece of epoxy film with micro-pillars onto flat or curved surfaces as shown in Figure 11, a two-stage pattern transfer process was developed involving: (1) the fabrication of a flexible PDMS negative pattern (micro-holes) from the original SU-8 micro-pillars which is then treated with a releasing agent, and (2) the transfer of the original pattern onto a thermoset epoxy coating from the negative mould.

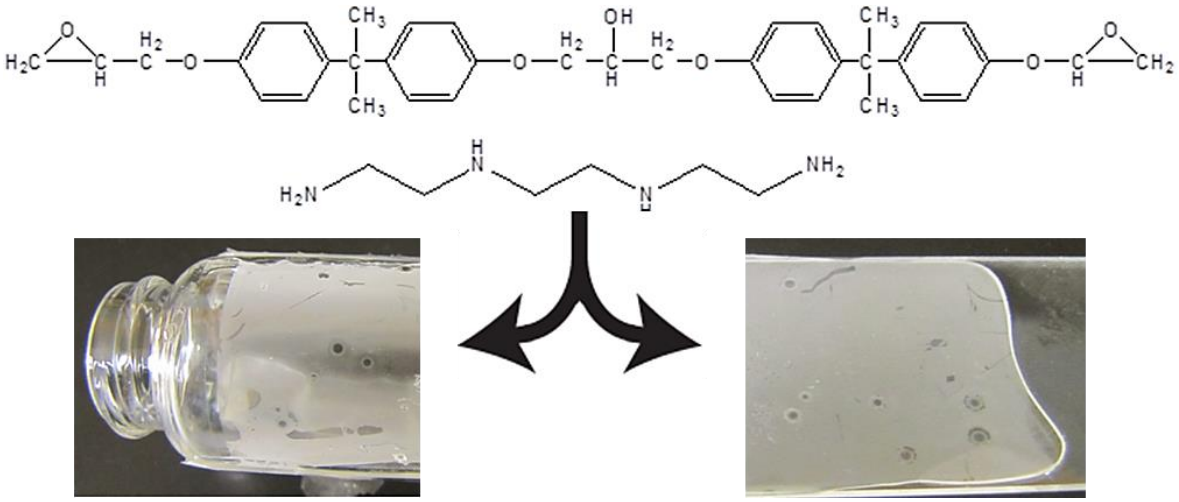

Figure 11: The chemical components of the epoxy mixture; DER 322 - a Bisphenol A diglycidylether and DEH 24 – triethylenetetramine and biomimetic patterned epoxy coatings onto flat (bottom right image) and curved surfaces (bottom left image)

Material Information

The PDMS polymer kit (Sylgard 184), the epoxy resin (DER 322), and the curing agent (DEH 24) were all purchased from Dow Corning and used as received. The Sylgard 184 kit consists of a PDMS resin and curing agent. Sylard 184 PDMS has been used as a standard research material due to a low-density, characteristic high hydrophobic surface properties, high fracture toughness over a wide temperature range, and low surface and bulk conductivity [26]. DER 322 is a bisphenol A diglycidyl ether, was selected for this study due to its low equivalent weight (176g/eq) and subsequent low viscosity. Dow Epoxy Curing Agent, DEH 24 (Triethylenetetramine – TETA) is an aliphatic polyamine with six active groups and an equivalent weight of 24g/eq, and was selected due to the tendency to undergo a slight contraction in size while curing at high temperatures. With these equivalent weights, the mixing ratio can be calculated as;

$$24g/eq * \left(\frac{100g}{176g/eq}\right) = 13.63g$$

where to fully cure the mixture, a minimum 13g of hardener is required for every 100g of resin. This procedure calls for a mixing ratio of 100:13 to ensure the complete curing of the material while an intense blending cycle with a vortex mixer is applied to disperse the hardener. Isopropyl alcohol is added as a diluting agent in a ratio of 1:100 to resin to decrease the viscosity, and any trapped air is removed under vacuum before the resin is cured at 90°C for 120 minutes. Figure 12 shows the chemical structure of 1H, 1H, 2H, 2H-perfluorodecyltrichlorosilane (FDTS – $C_{10}H_4Cl_3F1_3Si$) which was purchased from Gelest, PA, and used as a releasing agent. A self-assembled monolayer was fabricated under vacuum at 110°C for 1 hour with FDTS and several mL of H_2O present to activate the agent and form a monolayer of 1-2nm on the cured PDMS surfaces.

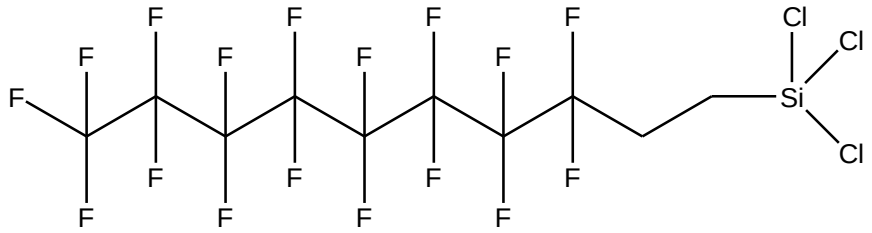

Figure 12: The chemical structure of 1H, 1H, 2H, 2H-perfluorodecyltrichlorosilane utilized as a releasing agent to provide a low surface energy monolayer to the PDMS stamps for easier release by decreasing the adhesion. The Chlorine groups hydrolyze and are removed to bond to surface hydroxyl groups

The FDTS monolayer was applied through a gas-phase application process to generate a smooth surface exposing the extremely hydrophobic and low surface energy fluorine groups outwards from the surface. The fluorination was performed under vacuum using a desiccator for 1 hour with 50-100μL of FDTS and several mL of H_2O present to activate the agent and form a monolayer of 1-2nm. The procedure was conducted within an oven at a temperature of 110°C to promote the chemisorption of FDTS and increase the lateral cross-linking of the molecules on the surface. The resulting effects of the surface treatment were observed through subsequent sessile drop contact angle analysis, where it was found that the pre-cured epoxy resin will wet the UVO treated surface more effectively than the non-treated surface.

Epoxy Dual-Pattern Transfer Process

The initial master mould of micro-pillars was fabricated using a negative SU-8 photoresist (SU-8-25, Microchem Co., Newton, MA, USA) supported by a silicon wafer, where a mask was used to control UV-radiation exposure and generate a uniform and regular hexagonal pattern of pillars within a cleanroom environment. SU-8 was the selected material for the initial mould due to high resolution capabilities of isolated features (inter-pillar spacing) and the low surface energy which allows materials to be peeled from its surface more easily. The micro-pillars have a height of 25μm, 10μm diameter, and a 25μm centre-to-centre spacing over a surface area of 3.5cm by 7cm. The surface was examined for quality via both optical microscopy (Wyko 1100, Veeco Instruments Inc., Plainview, NY, USA) and scanning electron microscope (LEO FE-SEM 1530 Carl Zeiss NTS), where each sample possessed a defect density of less than 5% [7].

The flexible soft-polymer negative pattern, or stamp, is a key feature to this pattern transfer allowing for the easy conformation of the final micro-pattern to a curved or more complex surface. Furthermore, the pattern-transfer procedure demonstrates a feasible use of biomimetic micro-patterns for large scale industrial application to improve the performance of conventional epoxy coatings. Figure 13 illustrates this two-stage transfer process.

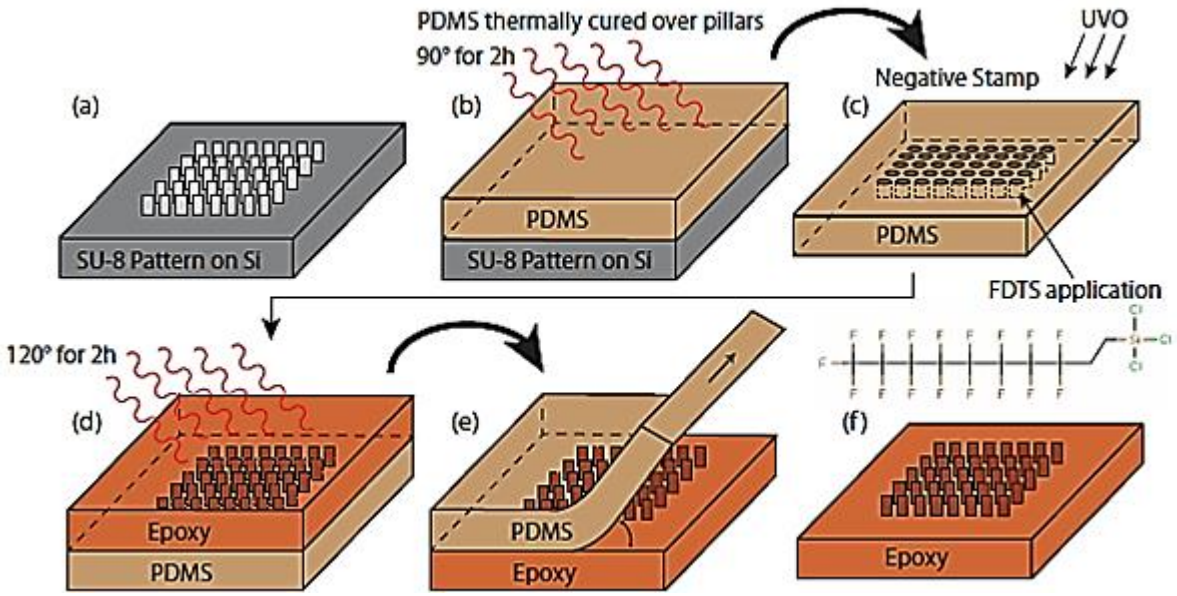

Figure 13: Schematic diagram of the pattern transfer process. Images (a) through (c) outline the first stage of the pattern transfer process from the SU-8 master pattern (fabricated via photolithographic techniques) and the surface treatment of the negative PDMS mould using soft lithography. Images (d) through (f) outline the application of the thermoset epoxy material and subsequent delamination of the negative mould resulting in the final epoxy pillars that mimic the original master SU-8 pattern

Using the original hexagonal array of rigid micro-pillars made of the photoresist SU-8 via UV-photolithography (Figure 13-a); a negative pattern of holes was subsequently fabricated. Figure 13-b represents the formation of the negative pattern, where a 10:1 weight ratio mixture of PDMS resin to curing agent was prepared and degassed before being spin-coated onto the SU-8 micro-pillars at 300RPM. The degassing process ensures both a good contact and consistency within the polymer matrix as it is cured that removes mechanically weak points and surface defects. Once cured, the PDMS negative stamp was peeled from the SU-8. The delamination of the PDMS mould from the epoxy surface post curing (Figure 13-e) was assisted with the addition of a polyethylene terephthalate (PET) sheet during the pre-curing stages of the stamp fabrication to strengthen the shear modulus of the PDMS and prevent tearing. An optical profilometer was used to observe the topographical structure and cross-section of the negative pattern to confirm that there was no damage or loss of structural details during the process.

Figure 13 d-f represents the second-stage of the pattern transfer, including the application of the epoxy resin to the negative mould and the fabrication of the pillar array mimicking the master SU-8 pattern. The negative mould must be held to the desired surface for 2 hours at 90°C in order for the epoxy to cure before the negative mould along with the PTFE substrate is peeled carefully to avoid tearing the PDMS and to maintain a clean pattern. For this peeling process, the thermodynamic work of adhesion between the epoxy and PDMS is low, as determined by:

$$W_{EP} = \gamma_E + \gamma_P - \gamma_{EP} \approx 37\ mJ/m^2$$

where the individual surface energy values γ_E = 46.2mJ/m^2,[24] and γ_P = 22-24mJ/m^2[25] along with the relation of $\boldsymbol{\gamma_{EP} \approx (\gamma_E \gamma_P)^{1/2}}$ are utilized. However, we found that the PDMS negative mould was easily torn during the peeling process of the second transfer stage. Recent work by Shahsavan et al. reported that an increase in aspect ratio for patterned polymer surfaces results in a significantly enhanced conformal adhesion due to local friction between the micro-pillars and the conforming matrix. Beyond a critical aspect ratio, the adhesive forces become too great to allow for clean delamination due to a drastic increase of the peeling force [7]. Thus, we suspect that the local friction forces generate a significant amplification of the global adhesion such that the adhesive forces are sufficient to tear the PDMS as it is peeled.

To reduce the adhesion and friction so as to avoid tearing the PDMS negative mould, we found it essential to generate a self-assembled monolayer (SAM) of fluorinating molecules (FDTS) to serve as a releasing agent on the PDMS surface. For this process, the surface of the negative PDMS stamp was first activated with ultra-violet-ozone (UVO) plasma. This process modifies the surface structure of the PDMS material with chain-scission that alters the surface layer in the presence of ozone to generate an abundance of hydroxyl surface functionalities. It has been reported by Efimenko et al. that the UVO treatment causes the material density of PDMS to reach 50% SiO_2 through the first 5nm of the materials surface during exposure of 28mW/cm^2 at a 6mm separation [26]. The oxygen-plasma penetrates several hundred nanometers into the bulk polymer while resulting in irreversible chemical changes near to the surface. These changes were analysed with X-ray photoelectron spectrometry to reveal the substitution of carbon atoms with oxygen, and ultimately generating the desired hydrophilic surfaces [61]. Although several groups reported that the UVO modified surfaces were polar following treatment, trace amounts of carbon containing species were detected via X-ray photoelectron spectometry even following very long treatment times [26]. Using a similar process, the negative mould was treated for a period of two hours, where we confirmed that this process altered the typically hydrophobic PDMS surface from the expected average value of 107.2° to a complete wetting state with a contact angle less than 5°. This behaviour was also observed for patterned surfaces, where the contact angle was altered from the observed average of 152° again to a complete wetting state with the water observed to penetrate the pillared structures. As the PDMS mould is not confined through this process, we expected and were able to confirm that the use of ozone plasma did not result in any cracking of the PDMS surface layers on the micro-level, validating that there was no significant form of induced mechanical or thermal stresses. Berdichevsky et al. reported similar observations [28]. However, as the surface layer of PDMS is converted to a thin and brittle silica-like layer, the mechanical properties of the PDMS is modified, where nano-scale cracks are formed below the visibly observable threshold. It is these cracks that was proposed by Owen and Smith to allow the migration of lower-molecular weight uncross-linked PDMS polymer molecules to the surface layer in an effect termed as the *hydrophobic recovery* [62]. The resulting high density of hydroxyl functionalities (-

OH) at the surface of the exposed PDMS serve as bridging molecules to the chlorinated silica of FDTS. These treatments resulted in a smooth FDTS monolayer coated on the PDMS significantly reducing the adhesion between the PDMS and epoxy layers, resulting in easier peeling from the cured epoxy surface.

With this pattern transfer procedure, arrays with a projected surface area of $10cm^2$ and as thick as 4mm (pattern on top of thick coating) are able to be generated consistently. The two-stage approach also provides the ability to transfer the pillar array to a curved surface. The soft negative PDMS stamp ensures both a good contact and consistency within the polymer matrix allowing for the stamp to be moulded and held to many different surfaces while the epoxy cures. Facilitated by the PET backing material, the negative mould was readily peeled from the cured epoxy, resulting in arrays of transparent epoxy pillars coated onto a curved surface. Figure 14 shows characteristic images from each stage of the pattern-transfer process: (a) the optical profile of the SU-8 pattern, (b) the PDMS negative stamp observed through an optical microscope, and (c) a SEM image of the resulting epoxy micro-pillars showing a clean and uniform array of pillars resembling the pattern observed from the initial SU-8 master mould. The micro-pillars closely resemble cylindrical structures with a flat top, although it is observed that slight undercutting during SU-8 fabrication creates a slight edge. The star-like diffraction pattern observed in Figure 14-b is consistent with the hexagonal configuration of the original SU-8 micro-pattern, and is presumably the result of Poissonian shrinkage of the PDMS network between the fixed pillars during the curing process. This shrinkage leads to the formation of slight peaks and valleys within the intermittent spaces around the PDMS micro-holes [7].

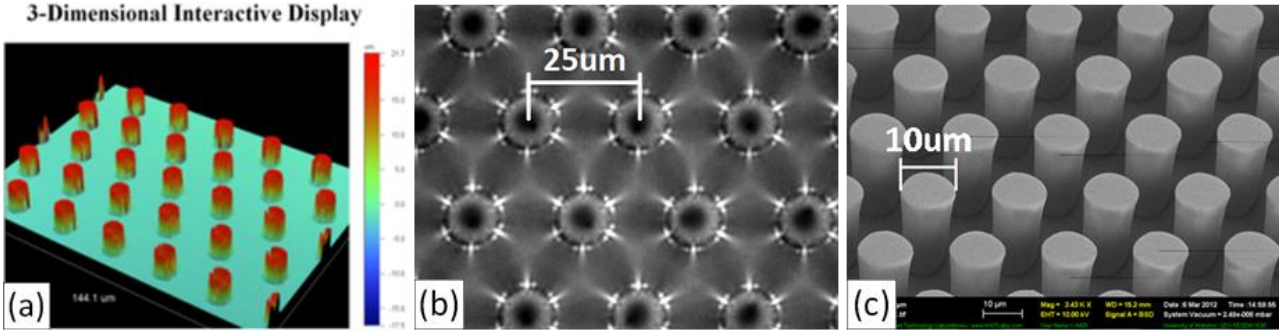

Figure 14: Characteristic results from each stage of the pattern-transfer process with; (a) the optical profile of the SU-8 pattern, (b) the PDMS negative mould as observed through an optical microscope, and (c) Au-coated epoxy micro-pillars at incident energy of 10keV and a magnification of 3500x observed at a 45° tilt

Control samples for all characterization testing were fabricated as flat non-patterned samples of DER 322 through a parallel procedure with the patterned samples; the sole exception being the use of a glass slide as the master mould versus the patterned SU-8 array.

Replication of Trembling Aspen Leaves

In attempt to directly copy the surface properties of a hydrophobic leaf sample with the fabrication of a physically identical synthetic replica, this two-stage pattern transfer process is the core of biomimetics. The PDMS polymer Sylgard 184 was again selected as the material of choice for this application due to its ability to flow easily and replicate complex patterns with a high precision through soft-lithographic processing. Furthermore, from an functional standpoint, the high hydrophobicity, contamination resistance, and long-term endurance make PDMS a very useful polymer for applications requiring insulation, anticorrosion, or antifouling properties [26]. The fabrication of synthetic leaves should be able to compete with the traditional heat moulding of polyesters, where future work aims to utilize different chemical dyes to further offer a more realistic substitute. Figure 15 below is a magnified optical image that showcases a Trembling Aspen leaf sample taken from a tree on the university of Waterloo campus. The micro-papillae are very easily observed as a dense pattern over the entire surface consisting of very similar sized asperities that are hemispherical in shape.

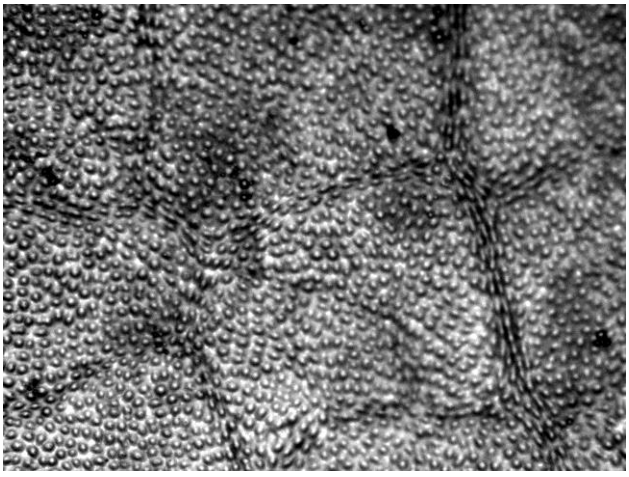

Figure 15: A magnified image of the Trembling Aspen leaf showing a rough structure with some areas more isotropic and showing different surface characteristics

To replicate this surface, a very similar procedure to the pattern transfer of epoxy micro-pillars was utilized. The easy to perform, and repeatable process leads to the conclusion that this process would be easily scaled up, and able to pattern as large of area as desired. The two-step pattern replication technique is outlined in Figure 16.

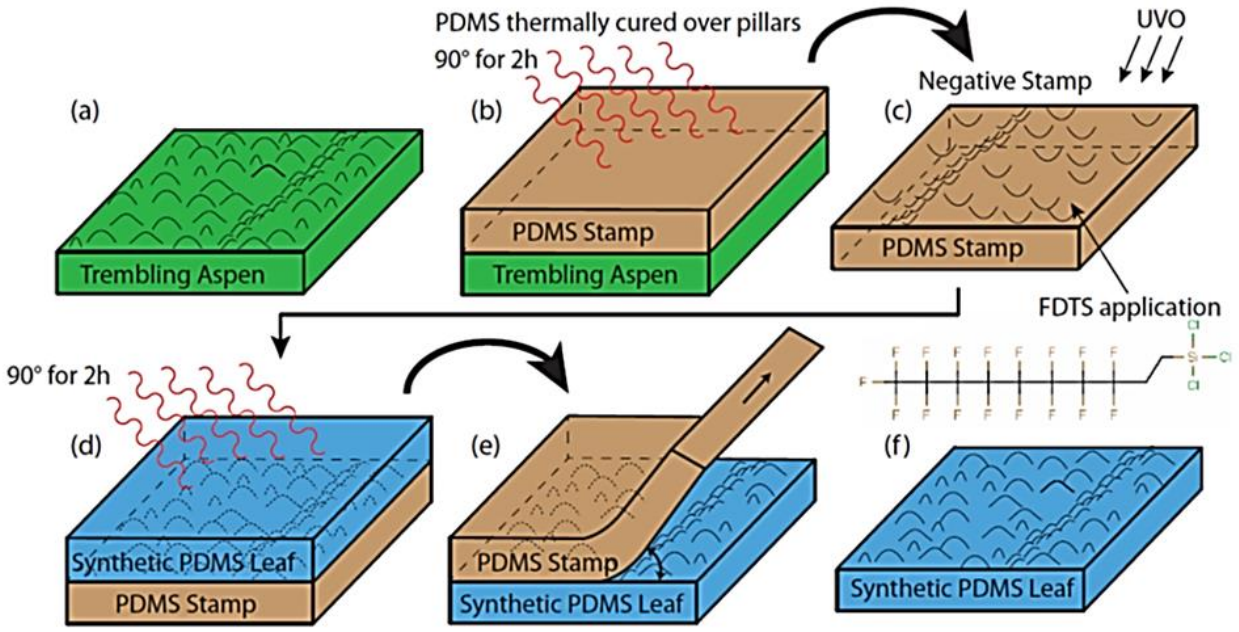

Figure 16: Schematic diagram of the Trembling Aspen synthetic leaf fabrication. Images (a) through (c) display the initial moulding of a negative stamp capturing the specifics of the leaf sample and the subsequent surface treatment with the FDTS releasing agent, while images (d) through (f) display the second pattern transfer to fabricate the synthetic leaf sample with PDMS

A fresh sample is picked from a tree and brought back to the lab to serve as the initial patterned substrate. The sample was prepared by attaching it to a glass slide and taping all edges down to prevent the curling of the sample during the thermal curing process and prevent any excess PDMS from leaking underneath the leaf sample. Sylgard 184, again mixed in a 1:10 ratio of resin to curing agent, was vortex mixed, degassed, and then applied to the sample after which it was left to cure for one hour at 90°C as in Figure 16-b. During this step, it was found that the leaf sample decomposed at this temperature from a colour change to a dull green from the initially vibrant green due to the rapid degradation of chlorophyll, which is the plant pigment responsible for giving plants its green colour [63]. The heat also causes water to evaporate from the leaf leading to a decrease in size and shriveling. However, this made for easier peeling as the internal structure of the micro-papillae shrank, and no longer filled the holes of the PDMS structure formed over the early stages of the curing process. Room-temperature curing was trailed with early samples in an attempt to navigate this issue with both fresh and dried leaf samples. However, it was very difficult to peel the PDMS after leaving it for the recommended 24 hour room-temperature curing period [64] as the leaf tore easily and adhered to the PDMS very readily. However, through visual analysis, it was found that the negative stamp actually copied the initial size of the micro-papillae before any size decrease, and the decomposition of the initial sample is a convenient result of the curing procedure. Figure 17 shows several different images obtained through optical microscopy of the negative stamps, clearly displaying the transfer of the micro-papillae to the stamp.

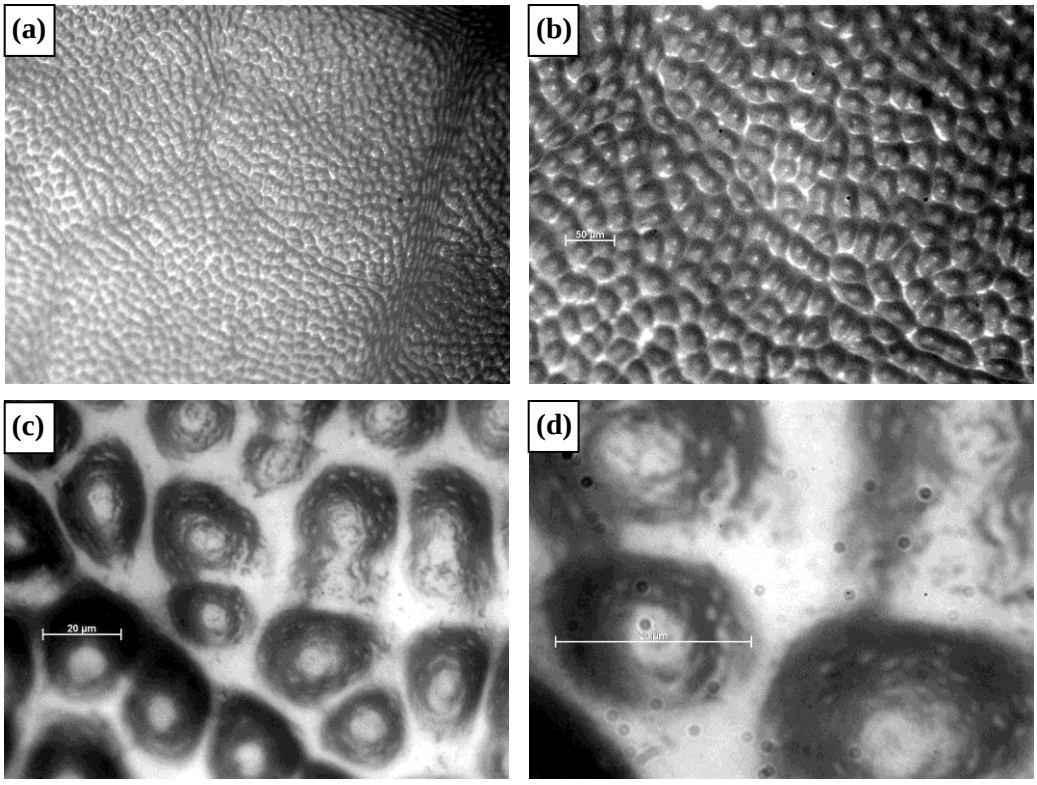

Figure 17: : Images of the negative stamp of a Trembling Aspen leaf at (a) 50 times, (b) 125 times, (c) 500 times, and (d) 1250 times magnification before surface treatment of FDTS. Scale reference bars indicate that the average size of the micro-papillae on the surface is 20µm

Figure 16-c refers to the surface treatment of the PDMS negative stamp with the gas-phase application of a monolayer of FDTS, which in this procedure served to act as a releasing SAM between the two PDMS layers. Following the initial exposure of the negative stamp to a UVO treatment for two hours, the abundance of hydroxyl functional groups served as a bridge for the chlorinated silica head-group of FDTS. The possibility of skipping the surface treatment step was trialed several times, and it was determined that it was not possible delaminate two PDMS samples from one another without tearing one or both of the samples as they fuse during the second curing stage in Figure 16-d. This is a result of the cross-linking and interpenetration of the PDMS polymer chains between the two samples as they cured, which effectively removes any defined interface separating the samples. Therefore, it was concluded that the FDTS surface treatment not only served to lower the surface energy, and therefore decrease the adhesion of the two polymers, but also as a physical separator that prevented the pre-cured liquid polymer and curing agent from penetrating the other matrix and cross-linking to the cured sample.

In order to understand the effect of the PDMS exposure to the UVO treatment prior to the application of the FDTS SAM, the contact angle was measured at different times during and following the exposure of a flat PDMS sample. Under the relative conditions that this investigation occurred, the initial contact angle measured for the flat PDMS sample was 113.5°, which decreased to a value of 94.8° after a

one hour exposure within the UVO chamber. After another hour of exposure, the contact angle decreased to a value of 41.8°. However, it was also observed that the contact angle for the PDMS surfaces decreased to a completely wetting state (contact angle < 5°) when exposed to the UVO plasma for two consecutive hours. This indicates that the effectiveness of the UVO exposure is dependent on the uninterrupted time in the UVO chamber that allows for the chain-scission to increase the SiO_2 density at the surface. After the second contact angle reading, the sample was left at ambient conditions exposed to atmosphere, and it was found that the contact angle only increased to a value of 56° after one hour.

Once the surface has been treated, Figure 16-e shows the application of a second layer of PDMS in a 1:10 ratio of resin to curing agent following the exact procedure as Figure 16-b stated above. The new synthetic leaf was then peeled from the negative mould, where it was found that the surface was an exact copy of the initial leaf sample. In comparing Figure 17 to Figure 18, the initial size, shape, and density of the micro-papillae are preserved through the dual pattern transfer procedure to the synthetic leaf sample.

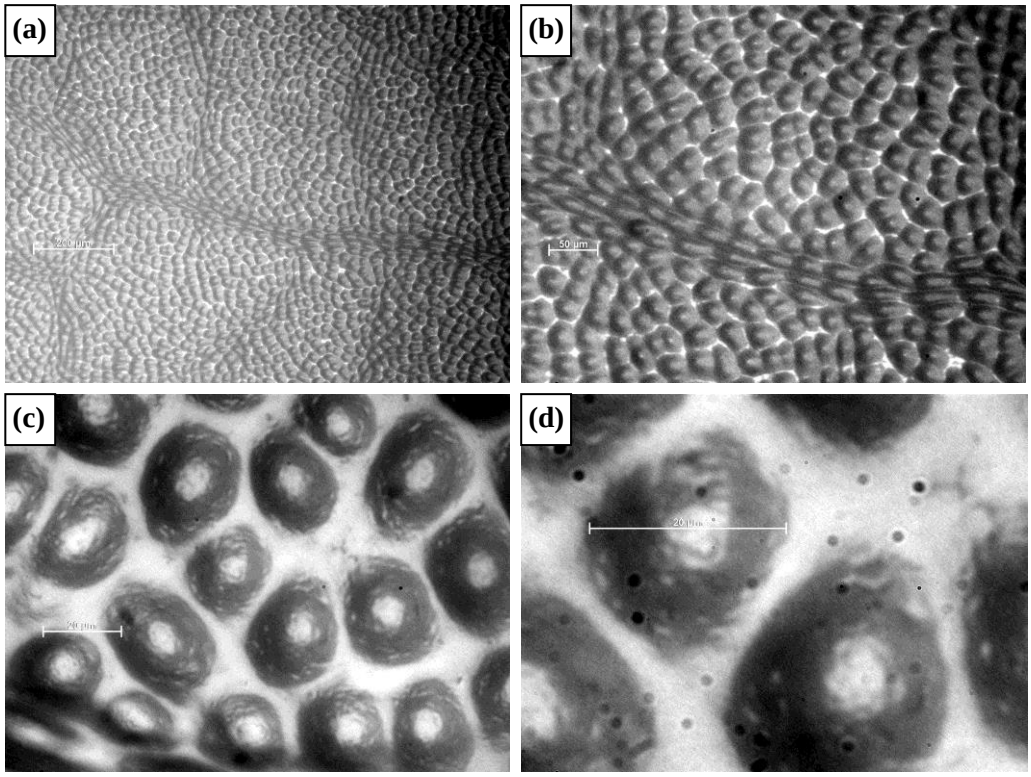

Figure 18: Images of the synthetic leaf sample as a copy of the original Trembling Aspen leaf mould at (a) 50 times, (b) 125 times, (c) 500 times, and (d) 1250 times magnification following the successful delamination of PDMS from PDMS following the surface treatment. Reference scale bar again shows that the final micro-papillae are approximately 20µm in diameter on average

Following the final peeling of the synthetic leaf sample from the negative stamp, close analysis of the surface shows that the stamp was not damaged from the procedure. In fact, it was able to be used repeatedly to generate samples without a loss of the releasing layer that allowed for the two PDMS

samples to delaminate without tearing. This major benefit of using PDMS in this procedure is that the flexible moulds are able to be used repeatedly to mass produce samples without the loss of materials in a destructive process. Moreover, though the initial leaf sample is decomposed in the creation of the initial moulds, the sample is able to be preserved in the synthetic variant, where simply repeating the surface treatment allows for a multiple use secondary master mould. Figure 19 shows a full leaf that was able to be copied resulting in a complete synthetic sample using a Canadian loonie as a reference for size.

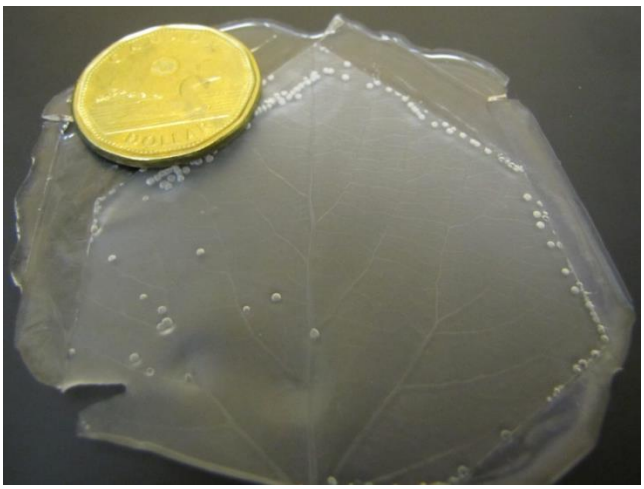

Figure 19: A full size sample synthetic leaf after peeling is complete

Through initial testing and observation, it was found that the synthetic leaf sample is better suited for extreme temperatures then its biological inspiration. The Trembling aspen leaf degrades at any temperature greater than 50°C for an extended period (as shown with the complete decomposition during the fabrication), and the surface waxes freezes within sub-zero temperatures (as much of the sample is actually H_2O) creating very brittle surfaces. Conversely, Dow Corning states that Sylgard 184 will remain functional within a temperature range of -45 to 200°C, or even for thermal cycling within temperature conditions reaching as low as -55°C [64].

Chapter 4

Characterization of the Patterned Surface

This chapter describes the characterization of the patterned surfaces in regards to the wetting and tribological properties. The wetting behaviour of the fabricated surfaces is observed, while the specific interaction between the surfaces and water is discussed in more detail. The robustness of the epoxy patterns is discussed and characterized in order to shed light on the primary benefit achieved through the use of a non-commonly patterned material via a novel pattern transfer process. Furthermore, the interaction of a complaint probe and a rigid surface is observed in comparison to the same probe used with a soft-material. Similarly, the application of a soft-probe to the rigid patterned surface is characterized in depth to understand the behaviour of the surface interactions on the micro-scale.

The majority of the characterization of the patterned epoxy coating has been published, including the pillar strength testing procedure and analysis along with the wetting and tribology data is an expanded representation of my published work[2]. The main drive of this work revolves around the ability of the fabricated surfaces to minimize the wetting by both maximizing the contact and minimizing the hysteresis and droplet adhesion at the contact interface. In patterning the epoxy surface, hydrophobicity was induced, and a better understanding of the surface's interaction with water was developed. The relative adhesive properties of the surface is an important material characteristic, where both the rolling angle of a droplet and the manner in which the droplet evaporates are used to characterize the surface. Statistical analysis is employed through the different procedural stages of the synthetic leaf fabrication using the wetting state to better understand what is happening throughout the process. Additionally, the tribological properties of both patterned systems are analyzed building an understanding from first principles to read into the data obtained and understand the enhancement resulting from the addition of a surface pattern. Furthermore, the tribological properties of the synthetic leaf, representing a compliant patterned surface, is characterized with a soft PDMS probe to understand the specific function of the loading force in determining the friction mechanism that should be applied.

Equipment

Typical epoxy coatings were prepared on both flat and curved glass surfaces with a thickness of approximately 4mm. Testing comprised of three samples of both patterned and non-patterned epoxy samples fabricated individually. The strength of the coatings was determined through indentation tests using a Universal Materials Tester (UMT) tribology system (CETR Campbell, CA, USA). The

[2] B. McDonald, H. Shahsavan, and B. Zhao, "Biomimetic Micro-Patterning of Epoxy Coatings for Enhanced Surface Hydrophobicity and Low Friction," *Macromolecular Materials and Engineering*, vol. 298, 2013.

deformation of the pillars was measured by moving a 440-C stainless steel hemispherical probe (radius = 0.8mm) towards the surface at a constant low speed and observing the force in the z-direction. The hydrophobicity of the epoxy coatings was characterized by measuring the water contact angle, where the silhouette of a droplet of a defined volume in a static state was captured to represent the surface interaction. This image was then analyzed with MATLAB imaging processing software to approximate the contact angle in an elliptical best-fit model. Friction tests were performed on a custom-designed micro-indentation and friction system complete with an inverted optical microscope (Carl Zeiss Axio Observer; Z1m) in-line with a CCD camera to monitor the contact area in real time [23]. Each test involved mounting the probe on a load cell (Transducer Techniques; TMO-2), attached to a compact nano-positioner (PI P-611; XZS) with a resolution of 0.2nm and a potential travel distance of 100μm. The nano-positioner was fixed on a movable linear stage (Newport; ESP-MFA-CC) with a range of 25 mm. The movement of the load cell was controlled by both nano-positioner and a displacement controller (PI E-625; PZT). Each trial was controlled through a custom-developed LabVIEW (version 8.5, National Instruments) interface. All measurements were conducted using a relatively soft PDMS (Sylgard 184) hemispherical probe tip with a 6mm ± 0.01mm diameter at a defined preload. The area of contact was observed while the stage travelled laterally with the probe interacting with the surface. Data sets comprised of three separate patterned and flat samples were constructed through systematically varying the preload applied to the surface while maintaining all other variables (travel distance, speed, approach, pause timing, and the detectors used). Tests were performed with preloads ranging from 0.98mN to 24.5mN.

Mechanical Strength of the Patterned Surface

The niche that the epoxy micro-pillars were fabricated to fill is to provide a strong coating material able to withstand large forces in both the normal and shear directions, while providing that hydrophobic benefits observed from the application of a pattern which has historically been easy to do using soft materials. It is important to know the mechanical behaviour of the micro-pillars for practical applications, where the strength of the epoxy pillars fabricated as a potential icephobic surface is a critical design component; the coating material must be robust enough to withstand typical weather conditions while also optimizing performance. The micro-indentation/UMT system was utilized to determine the strength of the pillar-array and determine the buckling (static) force required to destroy the patterned surface. A load bearing normal force was impacted onto the surface in order to observe the deflection of the micro-pillars as the force was increased, where the extent of any resulting damage can be seen. The ability of pillars to resist plastic deformation decreases with the size of pillars or an increasing aspect ratio as smaller pillars tend to bend and buckle more readily under an external stress or strain [65]. The

mechanical behaviour of this epoxy micro-pillar system was investigated by indenting a hemispherical indenter into the surface to deform the micro-pillars. Typical epoxy coatings were prepared on both flat and curved glass surfaces with a thickness of approximately 4mm, although all tribological tests were performed on the flat surfaces due to the linear nature of the dynamic measurements.

Using the UMT Tribology system, the stainless steel probe approached the surface at a constant speed where the resulting normal force interaction was recorded and analyzed. Figure 20 displays the typical indentation traces observed for both flat and patterned samples. The normal force increases at an approximately linear rate once the probe is in contact with the pillars. The pillars are deflected until a threshold value of 10μm, where they collapse under a force of 600mN and the modulus decreases as the surface is easily deformed. The probe continues to advance into the material while the force remains constant due to the inability of the pillars to offer resistance until solid contact is reestablished after approximately 20μm indentation. At this point the modulus resumes the constant linear trend with an equivalent modulus to the epoxy pillars prior to buckling. Throughout the plateau region, the compressive force does increases at a lower rate, where the constant resistance is observed to compress and bend the pillars rather than snapping them off completely. Parallel tests are performed from an equivalent load-displacement curve with flat epoxy coatings.

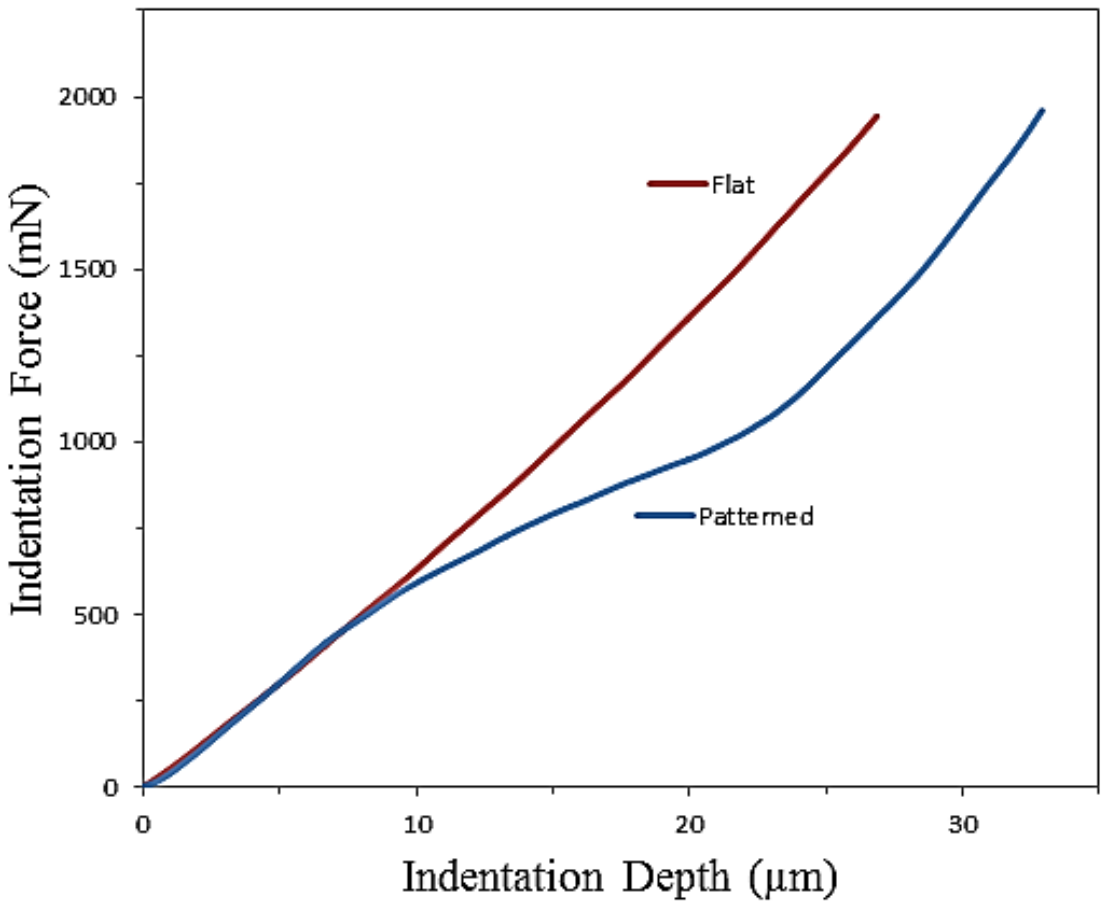

Figure 20: Force as a function of the vertical displacement of the steel probe on the UMT tribological instrument for both patterned and flat epoxy surface coatings. The pillars were observed to buckle under a load of 600mN. Each trend is an average of 3 samples

Using a spherical probe to characterize the indentation allows for the application of the Brinell hardness scale (HBW) as defined by the following equation;

$$HBW = 0.102\frac{2F}{\pi D(D - \sqrt{D^2 - d^2})}$$

In this equation, F is the applied normal force, *D* is the diameter of the indenter, and *d* is the diameter of the indented area. The HBW is a test standard that is able to be empirically correlated to the ultimate tensile strength of a material prior to fracture. Figure 20 indicates that the patterned surface begins to deflect under an applied load of 600mN when the indenting probe is 10µm into the sample. At this depth, the diameter of the steel sphere in contact with the surface into the surface is 0.252mm. These values result in a HBW factor of 1.219HB, which is comparable to samples of softwoods, but less than metals such as lead (5.0HB). Furthermore, the elastic modulus of the cured epoxy material was estimated using the Hertz model for indentation through measuring the compressive force recorded as a probe indents the

surface and calculating the reduced modulus. After imputing data found for the AISI Type 440-C stainless steel probe [30], the resulting Young's modulus of the epoxy in this study was found to be 500MPa.

We further estimate the pressure required to buckle the pillars from the applied force of 600mN, the radius of contact for a flat surface was estimated under the Hertz model such that, $\boldsymbol{a = \sqrt{r\delta}}$, where a is equal to the radius of the contact area as a function of the probe radius, r, and indentation depth, δ. The contact area is found to be $2.5\times10^{-8}m^2$ at an indentation depth of 10μm where the probe is in contact with an average of 35 pillars or $2.7\times10^{-9}m^2$. The pressure applied to this area resulting in the collapse of the pattern is equal to 222.2MPa, which is equivalent to a 80kg mass placed on an area of $3.56\times10^{-6}m^2$ (equivalent to $3.53mm^2$).

Wetting Behaviour and Properties of the Patterned Epoxy Surface

We have employed three types of water contact angle measurements to evaluate the response of the epoxy micro-pillars to water droplets. The three tests are: (a) static sessile water contact angle, (b) evaporation water contact angle, and (c) rolling of water droplets. Figure 21-a,b highlights the marked increase in contact angle that was observed with the addition of the micro-pattern to the epoxy surface versus a control sample. The increase in contact angle from 76.5°±5° to 151°±5° shows the importance of contact area modification resulting from the addition of a surface pattern.

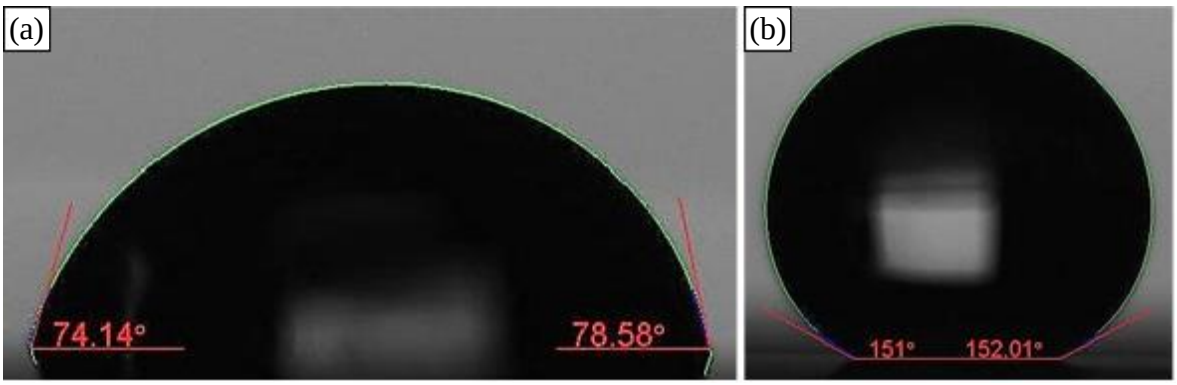

Figure 21: Sessile contact angle tests for (a) a flat, and (b) a patterned epoxy surface

Comparing the patterned and flat epoxy samples, the hydrophilic surface is observed to take on superhydrophobic properties when patterned. This indicates a contribution of an increased surface area and the creation of a heterogeneous interface. Furthermore, the spreading ability of the droplet on the patterned surface was monitored, where it appears that the microstructures inhibit spreading over an extended time. The study of this behaviour for water droplets on patterned superhydrophobic surfaces is well characterized and the system is understood within this context [18].

Using Young's equation along with the material properties of the epoxy [23] and water [47], we are able to determine the interfacial energy;

$$\gamma_{SG} = \gamma_{SL} + \gamma_{LG} * cos\theta_C$$

$$46.2\text{mJ/m}^2 = \gamma_{\text{SL}} + 72\text{mJ/m}^2 * \cos(76.5°)$$

$$\gamma_{\text{SL}} = 29.4\text{mJ/m}^2$$

with the surface energy along with contact angle obtained experimentally, we are able to determine the spreading coefficient of water on the flat epoxy surface through the Young-Dupre relation;

$$S = \gamma_{LG}(cos\theta - 1)$$

$$S = 72mJ/m^2(\cos(76.5°) - 1) = -55.19mJ/m^2$$

where the negative value indicates the partial wetting state of the surface as shown in Figure 21-a.

In looking at the effect of the surface pattern on the wetting properties of the surface, we applied the classical Wenzel model to explain the changing contact angle. In this model an atomically smooth patterned surface with cylindrical pillars is assumed, along with a complete contact between the liquid and solid. The resulting contact angle is predicted from the ratio of the real to the projected surface area.

$$\cos\theta_W{}^* = r * \cos\theta_C$$

Using the physical parameters of the micro-patterned surface relative to the control sample (given r = 0.408) along with the contact angle of the non-patterned sample, θ_C, the Wenzel model predicts an effective contact angle, θ_W* equal to 55.1°; this reduced contact angle was not observed in our experiments. As the wetting state does not follow the Wenzel model, which can be observed by noting that the surface inherits hydrophobic properties from the application of a pattern versus the predicted enhancement of the hydrophilic characteristics, we know that there must be broken contact at the interface. Similar to the Lotus flowers ability to support a droplet on top of its asperities preventing complete penetration into the pattern, the patterned epoxy surface follows the Cassie model that accounts for the droplet sitting on a hybrid interface of both the pillar tops and air;

$$cos\theta_{CB}{}^* = f\ (1 + cos\theta_C) - 1$$

within this relation, f is the area fraction of the water/solid interface. Assuming a series of flat and uniform pillar surfaces where the droplet is only in contact with the top of each structure and does not penetrate into the epoxy micro-structures, we can calculate that f is equal to 0.145 for the 2D hexagonal close packed system with these dimensions (the ratio of pillar top surface area to the unit cell area, $\frac{\mathbf{2}}{\sqrt{\mathbf{3}}}\frac{\boldsymbol{\pi r^2}}{\boldsymbol{cc^2}}$, where r is the pillar radius and, cc, is the centre to centre spacing). With this assumption and the contact angle for the flat epoxy sample, we calculated the effective contact angle of the patterned surface, θ_{CB}*;

$$cos\theta_{CB}{}^* = 0.145(1 + \cos(76.5°)) - 1$$

$$\theta_{CB}{}^* = 145.2°$$

This value is similar to the observed contact angle of the patterned surface. Therefore, it is reasonable to assume that the superhydrophobic wetting state of the epoxy micro-pillars is a result of Cassie-Baxter wetting mechanism.

Taking this reasoning one-step further, we can assume that this system will have to incorporate a minor adjustment for the *f* value under the assumption that the water droplet will convex into the pillared structures to increase the relative surface area of the water-air interface versus the epoxy-water. Using the experimentally determined values, we find *f* to be;

$$\cos(151.5°) = f * (1 + \cos(76.5°)) - 1$$

$$f = 0.098247$$

Here the decreased value of the epoxy-water contact area ratio indicates that there is in fact more water-air interface than predicted under ideal conditions using the strict model proposed by Cassie and Baxter.

In order to attempt to maximize the observed contact angle, preliminary tests were performed on completed epoxy patterns by attempting to coat the surface with a SAM of FDTS in a similar method to the releasing layer used in the pattern transfer procedures described in Chapter 3. Although the chemical compatibility is not there with the epoxy material as is with the PDMS substrates, it was believed that an unbounded physisorbed layer of FDTS molecules might provide a means to increase the superhydrophobicity. Figure 22 qualitatively shows that there is little difference in the contact angle with the application of the SAM, and there was no statistically relevant change in the mean contact angle values.

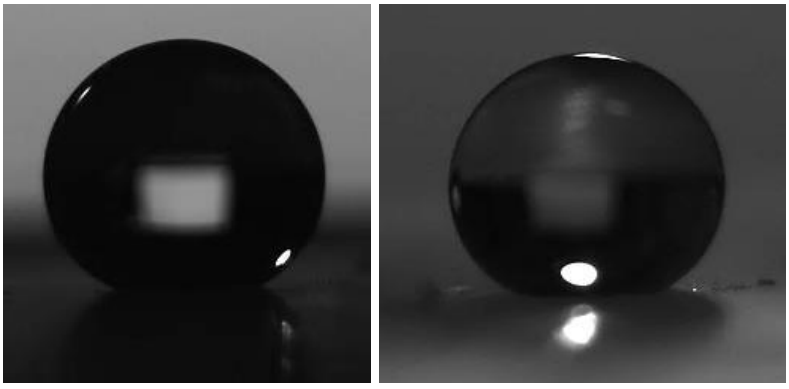

Figure 22: Sessile contact angle test images both before (left), and following (right) an attempted gas-phase application of a monolayer of FDTS fluorinating molecules

To understand more about the adhesive properties of the surface, sessile drop testing was performed over an extended period at ambient conditions to observe how a droplet evaporates from both the patterned and smooth epoxy surfaces. Figure 23 shows the evolution of the contact angle for each surface. The patterned epoxy coating displays hydrophobicity with an initial contact angle greater than 150°, while the flat epoxy coating shows an initial hydrophilic contact angle of 85°.

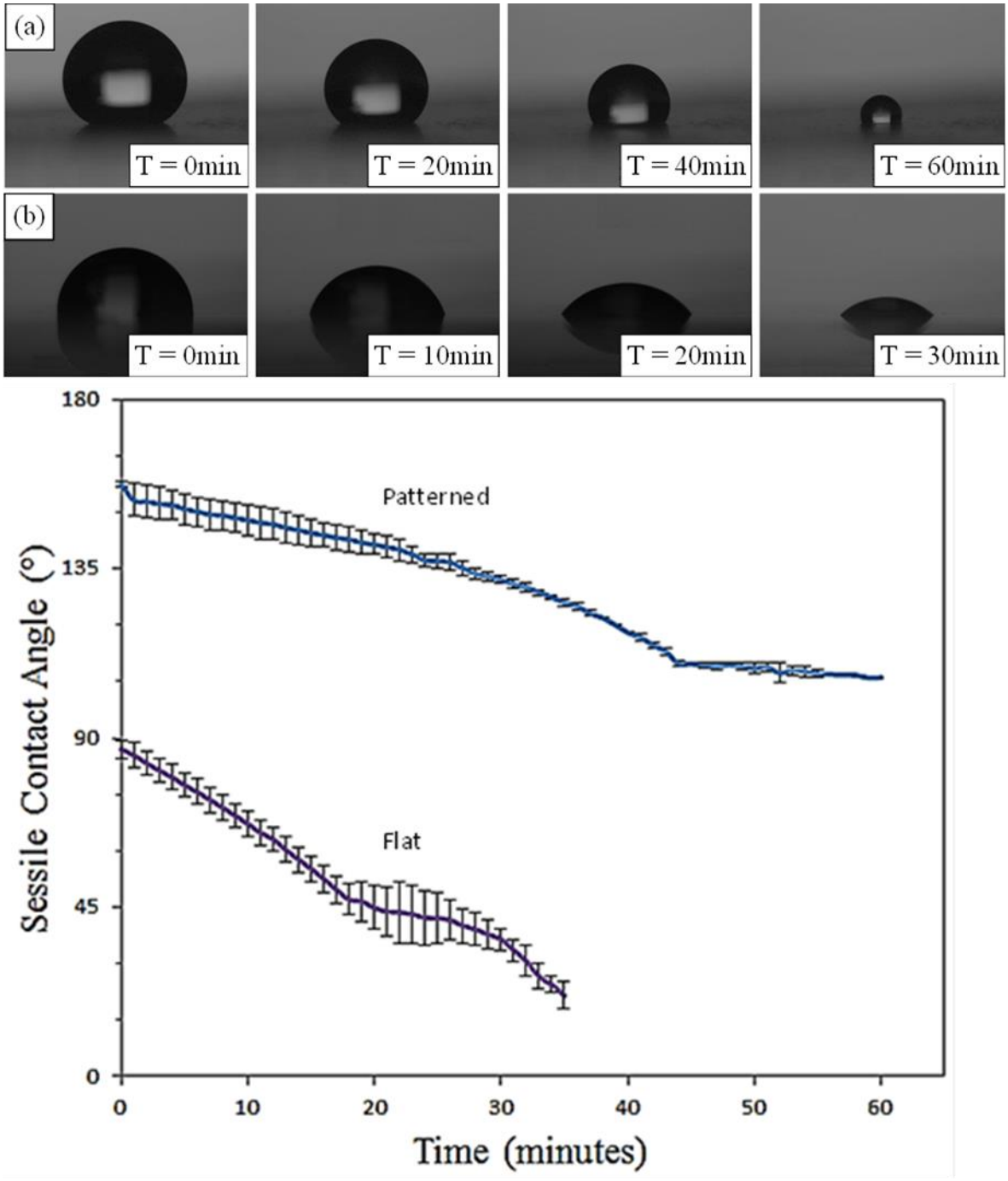

Figure 23: Contact angle variation over time as 15µL droplet evaporates at 25.1°C and 24% relative humidity from (a) patterned and (b) flat epoxy surfaces. Each trend is averaged from 3 trials

Both samples show a decreasing contact angle over time, although the patterned surface delays this decrease. It is important to note that although the patterned surface shows a decreasing trend, it never dips below the 90° hypothetical line that separates hydrophilic from hydrophobic surfaces until the droplet completely evaporates. As the droplet evaporates, a stationary contact line will lead to an evolving

contact angle with a constant area of contact. On the patterned surface, the more consistent contact angle is indicative of water being able to penetrate the surface structures and promote a hybrid wetting state that remains relatively constant. However, the results are more in line with higher adhesion liquid/solid interfaces when compared to literature [12].

Similar to the way in which the contact angle was predicted with the Cassie-Baxter model, looking at the dynamic state of wetting shows why the contact angle evolves over time. As the flat epoxy sample was found to be hydrophilic, the surface wets more and more as the droplet on the surface reaches an equilibrium state. This indicates that there will be more and more penetration into the pillar array over time, resulting in a growing epoxy-water interface relative to the constant meniscus contact area of water and air. Therefore the value of *f* will continue to increase. Looking at the trend of the patterned surface's contact angle value over time in Figure 23, we can see that the contact angle decreases to approximately 135° after 30 minutes of contact time. Using this contact angle to calculate a value for *f*;

$$\cos(135°) = f * (1 + \cos(76.5°)) - 1$$

$$f = 0.24$$

Assuming a torus-like penetration pattern around the pillars, this is equal to the droplet penetrating a distance of 12.2μm into the pattern over the 30 minutes that the droplet was in contact with the interface.

We observed relatively little droplet pinning for the patterned epoxy surface suggesting that there is little hysteretic interaction between the droplet and micro-pillars. The increase in contact angle in combination with a low hysteresis allows the droplet to roll on the micro-patterned surface. To verify this point, 5μL droplets were placed on the epoxy coated glass slides and held at different angles. Non-patterned epoxy samples were able to be held at angles of both 180° (Figure 24-a) and 90° (Figure 24-b) without the droplet moving. In contrast, the patterned surface was unable to be tilted more than 29° on any axis before the droplet would release from the surface.

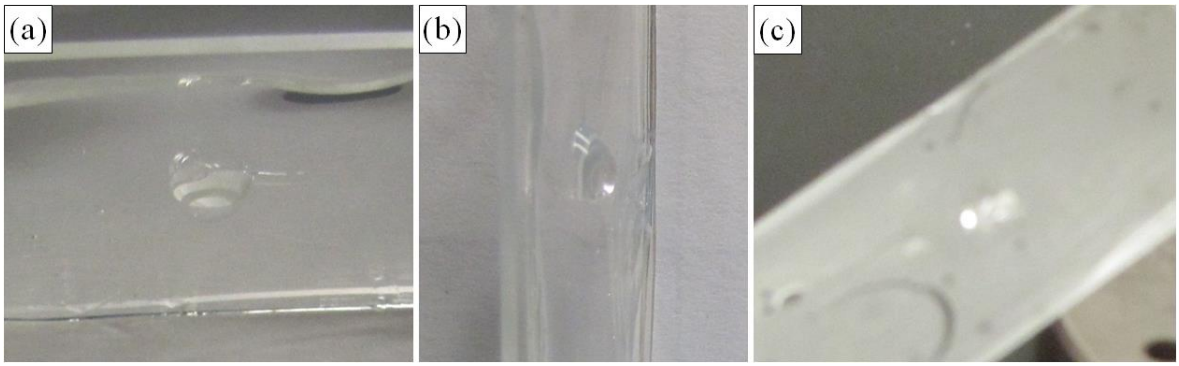

Figure 24: Images of a 5μL droplet on epoxy surfaces; (a) flat epoxy at 180°, (b) flat epoxy at 90°, and (c) patterned epoxy at 25°

In looking at the contact angle hysteresis, we obtain an idea of the ability of a droplet to roll on the surface, which is an important factor in the ability of a surface to remain dry with the impact of water droplets ultimately preventing icing. The contact angle hysteresis for the patterned epoxy surface was determined by using the tip of the syringe used to inject the water as an arm to drag the droplet on the surface while images were captured during motion as shown in Figure 25.

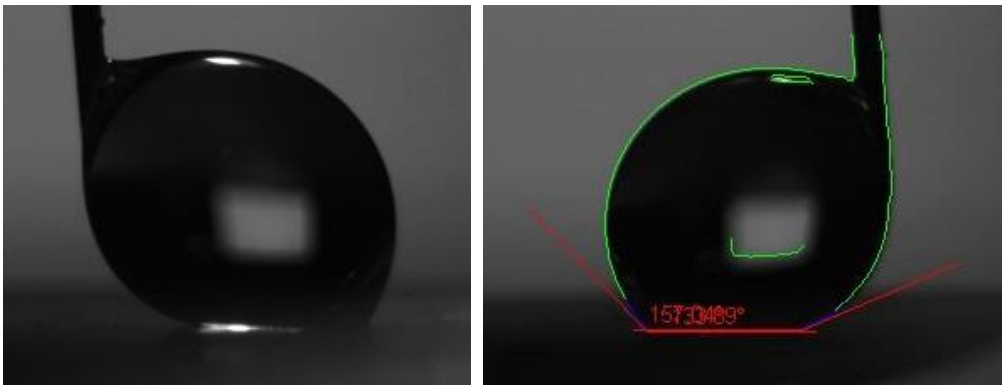

Figure 25: Contact angle and hysteresis values obtained from a 6µL droplet on a patterned epoxy surface displaying the advancing and receding angles observed on the patterned epoxy surface

From Figure 25 (right), we see that the approximate advancing edge is at an angle of 157.04°, where the receding edge is 133.89°, resulting in a hysteresis value of 23.15°. The contact angle hysteresis of the patterned epoxy surface is relatively high compared to typical superhydrophobic surfaces with a hysteresis of less than 10°, which is indicative of high adhesion surfaces.

Wetting Behaviour and Properties of the Synthetic Leaf Sample

In order to better understand the developed pattern transfer process and to compare the synthesized leaf sample versus the actual hydrophobic Trembling Aspen leaf samples, the contact angle has been characterized at the different stages of the process. Figure 26 displays examples of the contact angle of the initial leaf sample found on the waxy natural patterned surface.

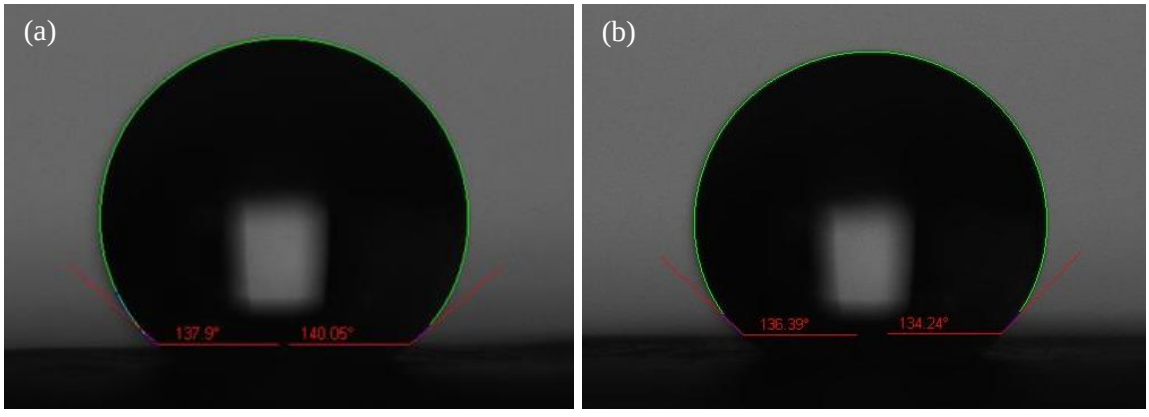

Figure 26: Images of a 10µL water droplet on different points on the surface of a Trembling Aspen leaf with the contact angles approximated through image processing software

The wetting state of hydrophobic leafs is derived from a hierarchical system starting with the micro-papillae on the surface, where the micron sized asperities are coated with a hydrophobic waxy layer with the potential of further crystallization creating a nano-structure [1]. The Wenzel wetting mechanism is apparent with this sample due to the high-adhesion nature of the leaf sample, where it is sumized that the water penetrates the surface structures to a great extent. In fact, droplets less than 15µL were able to be held at 180° angles without the droplet falling off. However, 20µL droplets did roll off of the surface when slowly tilted to approximately 75°.

In order to achieve a proper statistical analysis of the data, thorough and structured collection is an important aspect along with ensuring the repeatability of the data within this investigation. This allows for easier identification of the issues that center on how the values obtained for the surface properties are measured and reported, as they often conflict in how they are reported within literature [2]. The Trembling Aspen leaf has an average contact angle of 135.7°, which was determined from both the right and left edges of the droplet at three different locations on three different leaf samples. This type of sampling was utilized in order to determine the sources of variability for the biological sample. Table 2 showcases the data collected to find out if significant variability exists among the different leaf samples, or on different locations on the surface of the leaf.

Table 2: The ANOVA table of the Trembling Aspen leaves sampled (3 samples at 3 separate points on the surface) showing the F-observed values against the null hypothesis testing if the variance of the samples, or on the sample is significant

ANOVA	Sum of Squares	Degrees of Freedom	Mean Square	F_{OBS}
Between Samples	107.43	2	53.71	1.386
Within Samples	202.64	2	101.32	2.614
Total	310.07	8	38.76	

Comparing the F-observed values determined from the mean square of the variance sources over the total mean square results in a comparative value to the critical value determined from the sample population sizes within the F-distribution comparing variances. For each case, the F-criticle value is the same; $\mathbf{F_{0.05,\ 2,\ 8} = 4.46}$. The F-critical value is taken from the F-distribution, and refers to the null hypothesis being testing under a 95% confidence interval. That each F-observed value is less than the F-critical indicates that neither of the two sources of variability are able to reject the null hypothesis of the sources being equal to zero. Therefore there is no significant variability from sample to sample or between different spots on each sample.

In looking at the negative stamp casted in PDMS, the first observation is the decrease in contact angle from the actual Trembling Aspen leaf samples to a value of 121.9° which indicates the contribution of the waxy nanostructures, and their greater contribution to the hydrophobic characteristics of the sample than the negative PDMS surface [66]. Figure 27 displays images of the contact angle measured for the negative stamp of PDMS. It was determined that a SAM of FDTS was required to be deposited on the surface of the negative stamp prior to the second pattern transfer in order to separate the two layers of PDMS and prevent any cross-sample bonding. Additionally, it was found that the application of the FDTS did not increase the contact angle of the PDMS sample significantly. The two collections of sample data for the untreated and treated PDMS samples were determined to be equal through testing to see if there is any statistically significant difference between the means by testing the hypothesis that the difference in the means is equal to zero. Once the two variances were found to be considered equal through an F-test, an observed T-value can be determined through comparing the means with an adjusted variance; the value for these data sets was calculated as 1.817 with 14 degrees of freedom. In looking to the T-distribution for the critical value at a 95% confidence interval, the T-critical was found to be 2.14. Therefore, as the T-observable is less than the T-critical, we fail to reject the original hypothesis, and conclude that the means are not significantly different on this confidence interval. The negligible increase of contact angle from the application of the monolayer conflicts with the expected increase in hydrophobicity due to the lower surface energy of the fluorinated tails. However, as described above, the layer served more the facilitate the separation of the PDMS layers during curing, and was found to be tough, as several trials with the same treated sample failed to degrade the results obtained.

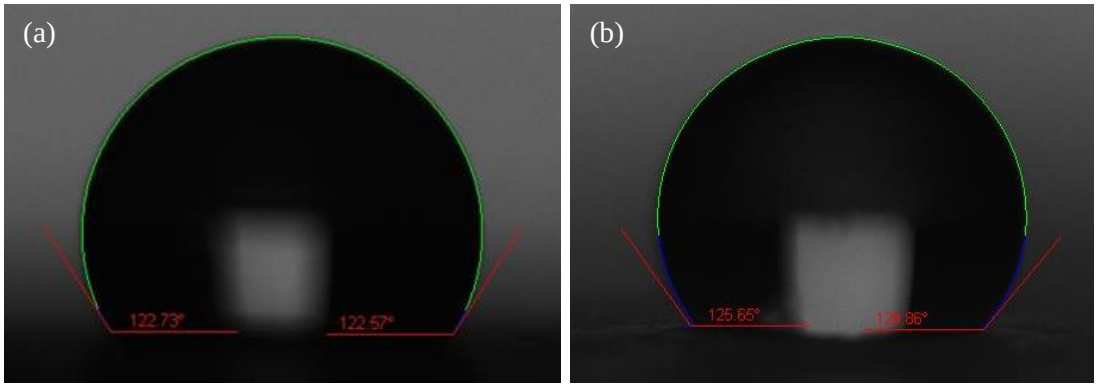

Figure 27: The sessile contact angle test of the negative PDMS stamp prior to the surface treatment

Additionally, using ANOVA methods for the sample populations of the untreated and treated PDMS sample, we find that the observed F-values indicate that there is no statistically significant variance either between the different leaf samples, or from sample to sample. However, it is worth noting that there is a greater contribution of variance between leaf samples than from within the same sample indicating that

the variance observed may be more a result of the different leaf samples found in nature than the instrumental and procedural error of back-to-back samples.

After generating a successful pattern transfer, the hydrophobicity of the synthetic leaf was measured. Figure 28 is one of many measurements where the average value was found to be 115.8°.

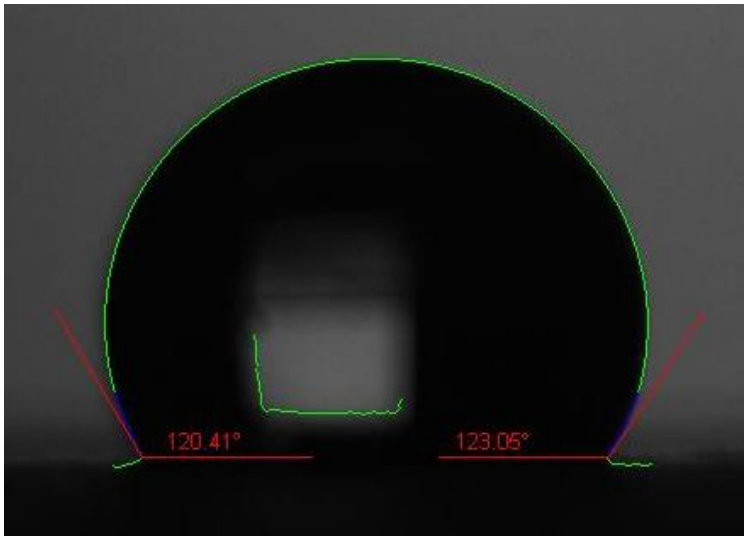

Figure 28: The contact angle of the final synthetic PDMS Trembling Aspen replicate leaf

As the roughness of the negative stamp and the replicated synthetic leaf can be considered equal through the nature of the pattern transfer process, the difference in contact angle must be the result of some other influence. This observation supports later claims for icephobicity where the skewness and kurtosis of a surface affects the adhesive force of droplets and therefore frozen droplets to a surface. The skewness is a measure of the asymmetry of the profile against the mean of a rough surface, while the kurtosis is a measure of the spikyness of a surface versus a more rounded bumpy surface. Figure 29 characterizes the difference between a more rounded rough surface and a more sharp and spiky profile, where more sharp surfaces cause a shift towards the Cassie wetting regime and an increase in hydrophobicity.

Figure 29: Different surface profiles showing the different kurtosis values for a surface, where the more positive the value (shifted towards the profile on the right), the more a surface will show hydrophobic and icephobic tendencies [67]

As a result of the inverted roughness, the observed decrease in contact angle observed for the synthetic leaf sample relative to the negative stamp, which has been shown to be statistically significant, is

expected. Several reports suggest that skewing the surface roughness towards the presence of a greater number of peaks versus valleys affects the observed water adhesion of the surface [12], [47], [68].

Tribological Properties of Epoxy Micro-Pillars

In observing the effect of a surface pattern on the hydrophobicity and tribology of different substrates, there are many different factors that contribute to the observations on a macro-scale. Physical aspects of the surface pattern that can be controlled include the aspect ratio and density of the surface features without compromising performance due to surface self-deformation. The effect of rigidity and topography on the tribological performance of surfaces has been studied in depth alongside the effect of variable normal load, shear velocity, and polymer materials [20], [32], [69], [70], [71], [72], [73], [74], [75], [76], [77], [78], [79], [80], [81], [82], [83], [84], [85], [86], [87]. Many studies have highlighted the ability to customize toughness, hardness, and the surface chemistry of thermoset materials. The ability to effectively and accurately transfer micro-patterns to conventional epoxy coatings enhances the hydrophobicity and reduces the surface adhesion and friction without compromising structural integrity. As such, the micro-patterned epoxy coating offers an innovative means to improve protective coating performance in harsh outdoor or industrial conditions where the surface encounters severe external stress and strain.

Micro-patterning reduces the area of contact such that it is able to effectively influence the tribological properties of a surface. We expect that the patterned epoxy surface will lower the observed friction relative to the flat samples. To investigate the friction properties of epoxy micro-pillars, the friction force was measured under varying preloads while the dependence of the coefficient of friction on the preload was investigated. Figure 30 displays typical friction plots at 0.2g (1.96mN) of applied preload for both flat and patterned samples measuring the normal (F_Z) and shear forces (F_X) of a PDMS probe scanning the surface.

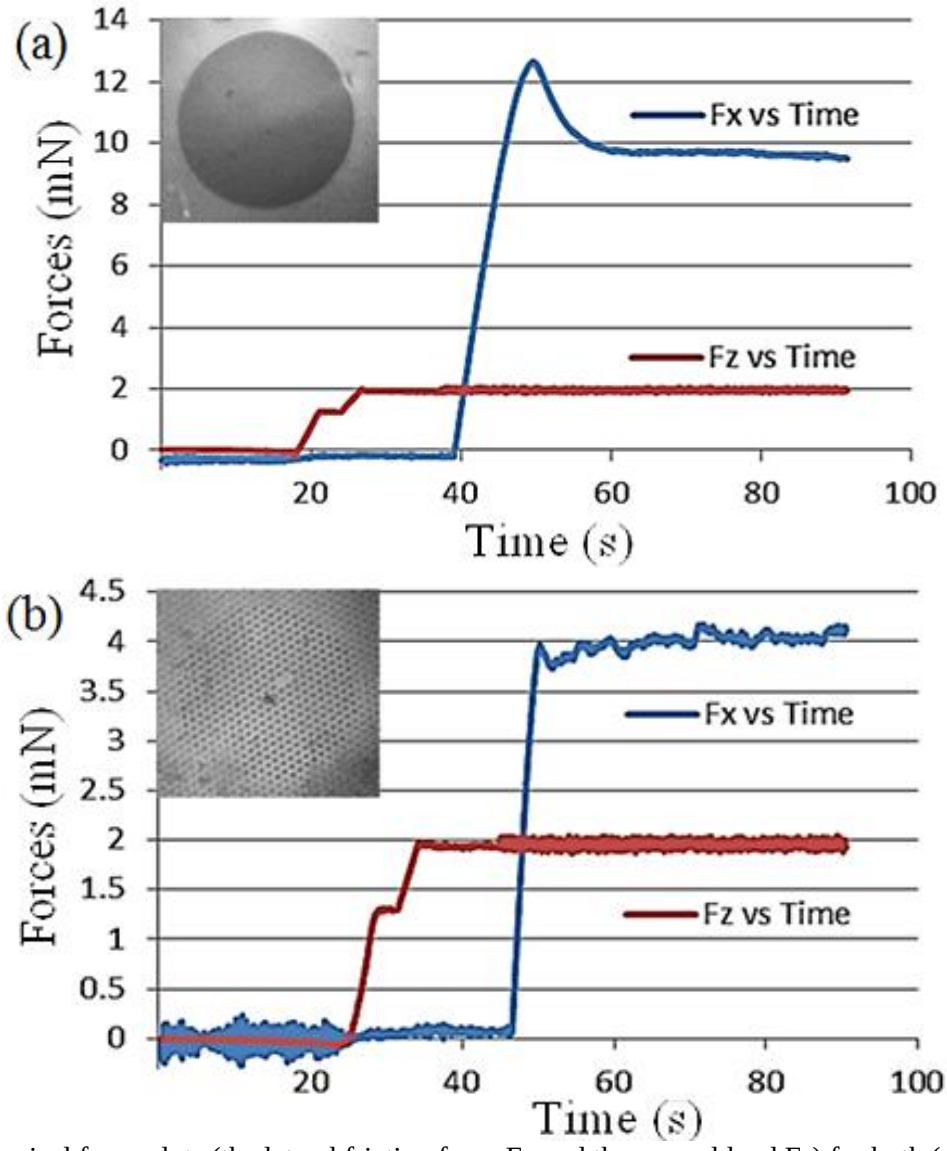

Figure 30: Typical force plots (the lateral friction force F_X and the normal load F_Z) for both (a) flat and (b) patterned thermoset polymer samples tracing both the parallel and perpendicular forces as the probe scanned the surface [insert: bottom view of contact area]

The maximum friction force for the flat and patterned samples was 12.65 and 4.18mN respectively while the average friction force within the kinetic region of the coatings is 11.38 and 3.99mN. The flat surface displays a large value of static friction, also known as stiction, represented by the large shear force required to initiate the motion of the probe. The addition of a micro-pattern to the epoxy material eliminates the stiction spike while decreasing the overall shear force. The absence of stiction for the patterned sample is a result of a consistent area of contact that recreates itself continuously through the duration of the scan in a series of smaller stick-slip interactions [32]. Conversely, the inability of the flat epoxy surface to recreate the contact area with the motion of the probe leads to a lower coefficient of friction than that at the onset of motion. Bottom view microscopy was used to qualitatively

examine the nature of contact, where the contrast observed between areas of contact versus the surrounding areas indicates that the contact mode is within the laid regime, i.e. the probe sits on top of the pillars. This is reinforced by the observation that there is no significant static friction response for the patterned surface indicating the suspension of probe on top of the micro-structures. Additionally, observing the patterned epoxy surface throughout the trials resulted in no apparent variance in the appearance of the pillar. This implies that there is no bending or deflection during the sliding, and therefore no contact observed between the probe and the side-walls of the pillars.

Figure 31 shows the dependence of the average friction force through the dynamic sliding regime on the preloads. The value of the friction force was calculated through a constructed Excel macro that first locates the maximum value of F_X measured, and then takes all values that fall within 80% of this value within the data set. The average F_X value is then found by taking the average of all these values, where it is assumed that the initial spike observed will balance the approach and retreat of the probe (both a small portion of the friction trace). The coefficient of friction is then found by dividing this average F_X value by the maximum F_Z value obtained. Within these trials, the friction is found to increase with the preload in a linear manner as predicted by the classical Amontons' friction law ($\boldsymbol{F_X \propto F_Z}$).

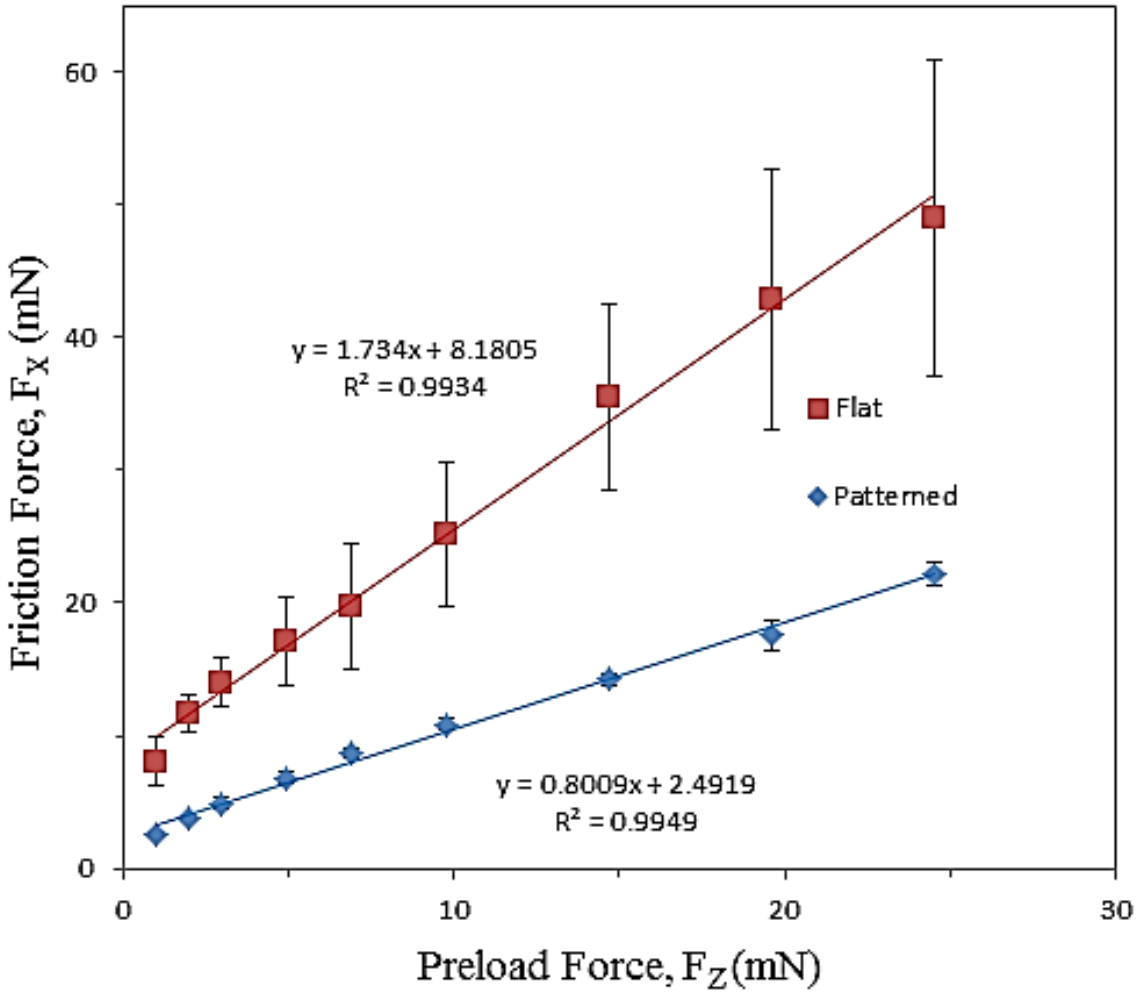

Figure 31: Average steady-state kinetic friction force as a function of the normal applied preload – fitting the data the correlation $F_X = \mu F_Z + \sigma_C A$

However, there is a discrepancy from the expected behaviour where it is predicted that the intercept should pass through the origin with no applied load. Bowden and Tabor proposed the inclusion of a term to incorporate a value for molecular adhesion based on the large coefficient of friction observed under low applied loads that is not predicted within classical linear models [33]. Moreover, Johnson et al. predicted that softer materials are able to deform by interfacial adhesion to generate a finite contact area with zero applied force [34]. Thus, the adhesion component, $\boldsymbol{\sigma_C A}$, was proposed as a function of the true contact area, A, and the adhesive shear strength of the interface, σ_C, where both variables are dependent on the normal load and the elastic properties of the materials in contact [36]. Subsequently, a combined model was proposed by Homola and Israelachvili to encompass both extremes in a single correlation; $\boldsymbol{F_X = \mu F_Z + \sigma_C A}$ [37]. Hence, Figure 31 reveals that there is a large adhesion-controlled friction component in the measured friction force, and that the intercept can be regarded to be equal to the adhesion component, $\boldsymbol{\sigma_C A}$. Apparently, the micro-pattern reduces the actual area of contact such that both

the adhesion and friction are reduced for the patterned surface without any change to the surface chemistry. The σ_C has been reported to be related to the adhesion hysteresis in a loading-unloading process, where its value is determined by the nature of the surface chemistry, the contact time, the separation velocity, etc. [37], [38] As both the flat surface and the tops of the micro-patterned surface are almost identical and the sliding conditions are equivalent, the difference in σ_C between the two surfaces would be negligible. The larger intercept for the flat surface is a result of the greater surface area generating a larger interfacial interaction, and inducing the elastic deformation of the probe as it nears the surface. A comparison of the slopes of the F_X versus F_Z plots in Figure 31 reveals that the coefficient, μ, in Homola's correlation is reduced for the micro-patterned surface. This suggests that the μ term is not only determined through surface chemistry, but also the surface topological features.

The coefficient of friction (COF) is defined as the ratio between the friction force and applied load ($\boldsymbol{COF = F_X / F_Z}$) and is a typical design parameter used in materials engineering. Although the overall relation between friction force and preload does not follow the Amontons' law as shown in Figure 31, we may still calculate the Amontons COF at each preload in contrast to Homola's overall coefficient. We investigated the dependence of the COF as a function of preload for both flat and micro-patterned epoxy coatings. As shown in Figure 32, the Amontons COF is remarkably higher at lower preloads, and gradually decreases to a lower plateau value as the applied load is increased past a threshold value.

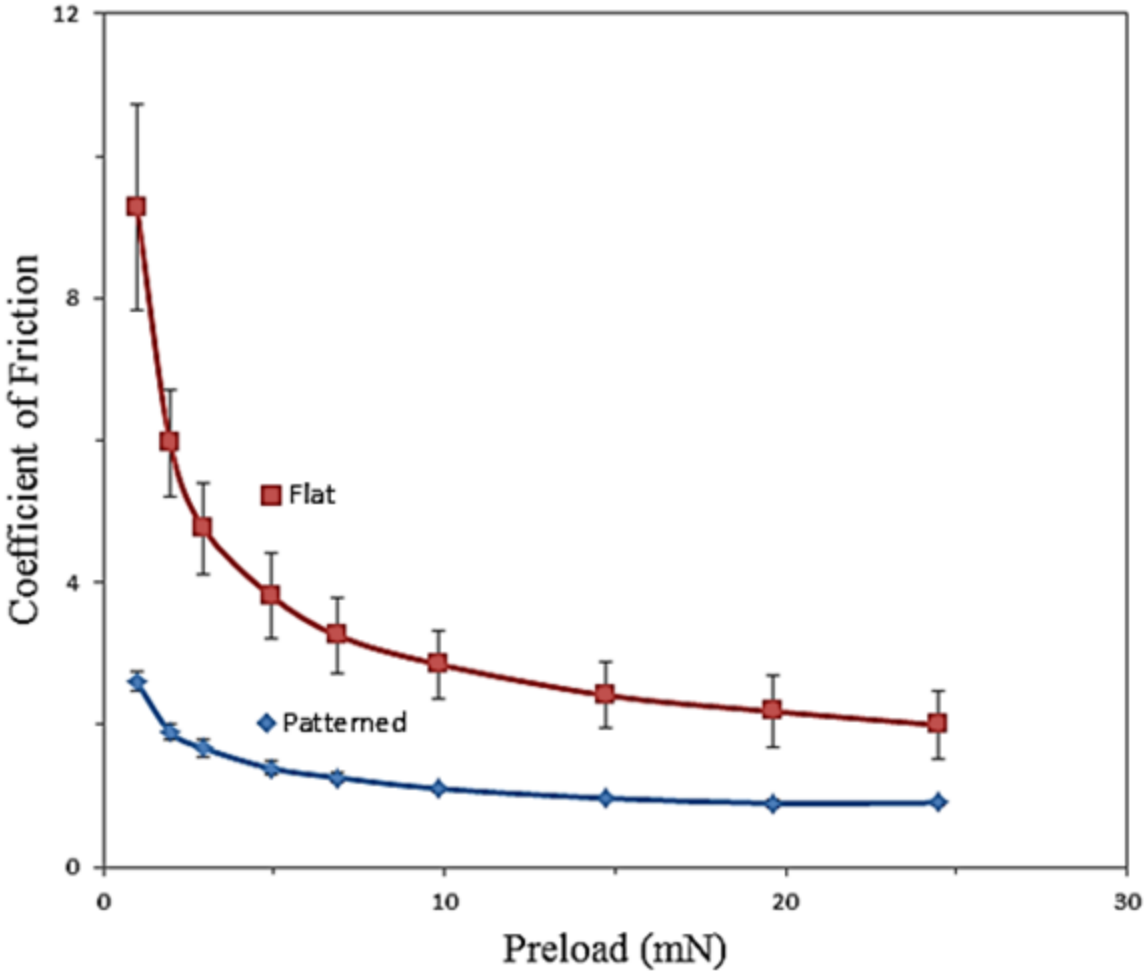

Figure 32: The local coefficient of friction defined as the shear force over the normal force as a function of the preload for both flat and micro-patterned surfaces

This trend may be attributed to the increased role of interfacial interactions as discussed in the preceding section. The high sensitivity of the local COF to the preload under low normal forces verifies the dominance of interfacial interactions over classical mechanisms for the soft polymer probe. This understanding is further confirmed by the observation that as the preload increases, the local value of the dynamic COF levels-off, indicating the transition from interfacial friction to the classical mode of friction. We further explored the dependence of COF on the preload by utilizing Schallamach's model, $\mu \sim \boldsymbol{C} * \boldsymbol{F_N^{-1/3}}$, for sliding a rubber on a hard surface, where the constant, *C*, is a function of the interfacial properties and the area of contact assuming a constant velocity.

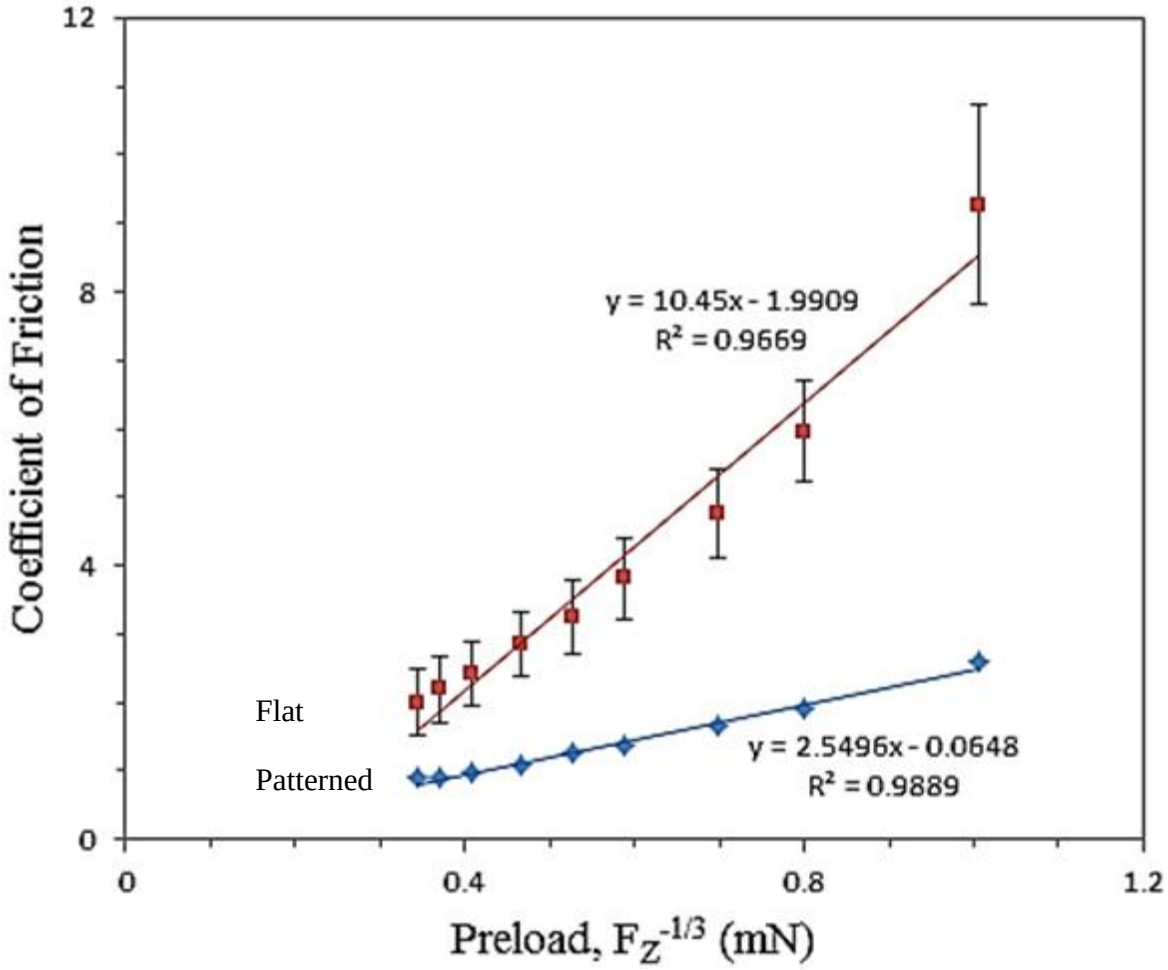

Figure 33: The Coefficient of Friction as measured from the steady-state values observed versus a variable preload adjusted to model Schallamach's relation referring to vulcanized rubbers on rough plates.

Figure 33 plots the COF as a function of the empirical relationship, $\boldsymbol{F_N^{-1/3}}$, and displays a linear trend. However, we noticed a deviation from linearity for the flat samples which we speculate to be a result of uneven distribution of the load on the surface at the contact line. This analysis suggests that the behaviour of the patterned epoxy surface exhibits a close adherence to Schallamach's relation, where the friction is a function of the true area of contact and normal load as suggested by Bowden and Tabor [20], [39].

Tribological Properties of Synthetic Leaf

The effect of a surface pattern is again observed in the tribological characterization of the synthetic leaf samples. The measurements of the synthetic leaf are unique in that they observe the realm of soft on soft interfacial elastic contact as opposed to contact with one relatively hard interface resulting in deformation of only one material. As stated before, the effect of many different variables has been studied for patterned surfaces, including the velocity, normal force, shape and size of surface features, and the material dependent elastic and surface chemistry properties of various substrates [70], [71], [72], [76],

[77], [79], [87], [88]. The friction is measured at multiple preloading forces to gauge the effect of adding the pattern to the compliant surface. The ability of a patterned surface to decrease the friction experienced occurs within the laid mode of contact that is well documented above. Within this system however, the more compliant nature of the PDMS material will result with a variable influence of the pattern on the friction measured. Though it would be interesting to compare the synthetic leaf versus the collected biological sample, the elastic and adhesive nature of the two materials resulted in the tearing of the samples during any dynamic testing.

From a series of tests, it was observed that the surface pattern reduces the friction force observed at low preloads, while this effect is dampened and eventually eclipsed as the normal force increases. Though the hydrophobicity of the patterned PDMS surface was only marginally increased over that of flat PDMS, the decrease in friction with the addition of a surface pattern is very pronounced. Separate trials were conducted with two synthetic Trembling Aspen samples, where a PDMS probe was scanned over the surface at a speed of 5µm/s for 1000µm after approaching the surface at 1µm/s in order to avoid overshooting the desired loading force. Each defined preload force involved two trials on the patterned surfaces, and one trial on a flat PDMS surface. Figure 34 displays the friction traces of this sample surfaces during these trials to offer a comparison between the patterned and the flat PDMS samples.

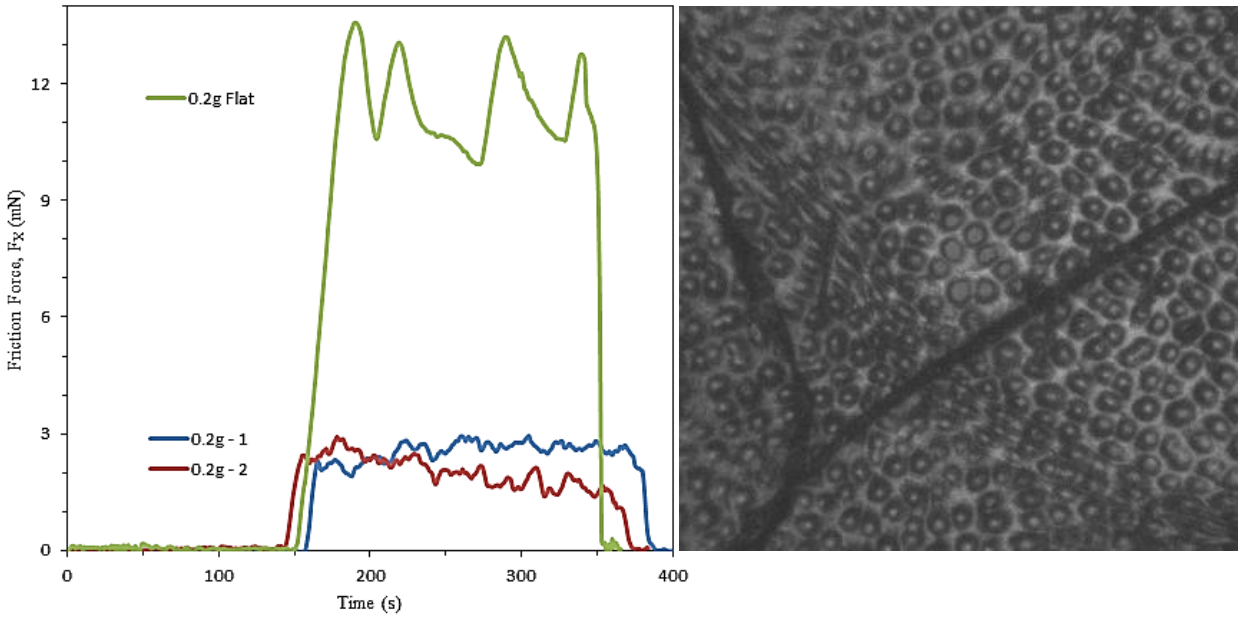

Figure 34: 1.96mN loading force applied to a synthetic leaf sample during a friction scan. The Friction traces on the left plot showcase the dissimilar nature of contact between the flat and patterned surfaces while the image on the right shows the minimal contact area of the probe on the patterned surface

In Figure 34 there are several expected trends that mimic the behaviour of other patterned surfaces, where the most striking observation is the large decrease in friction observed for the patterned surface. This is expected, as even though the coefficient of friction is greater at lower preloads, the laid

contact mechanism observed indicates a dramatic decrease in real area of contact. Therefore the ability of stiction and surface adhesion to influence the overall friction force experienced is also reduced. The difference in average experienced friction force was measured to be 9.53mN, or 4.86 times the initial loading force. Additionally, the flat surface shows a very large value of static friction resulting from the stiction at the onset of the initial contact, which is much more pronounced at lower preloading values (Figure 34 versus Figure 35) as a result of the refined model of friction as proposed by Israelachvili $\boldsymbol{F_X = \mu F_Z + \sigma_C A}$ [37].

As discussed based on Figure 30, the addition of a pattern eliminated the stiction spike at the onset of lateral motion. This phenomena results from the ability of the patterned surface to continuously recreate the area of contact with each asperity in a series of small stick-slip type motions which is reflected in the erratic and constantly changing F_X for the patterned friction traces while the overall value of the F_X remains relatively constant [32]. Furthermore, the image of contact from bottom view microscopy in Figure 34 confirms that the contact is primarily within the laid regime where the probe lays on top of the pattern, and does not contact the area in-between the asperities. However, as opposed to the more rigid epoxy flat surface, the elastic nature of the PDMS flat surface allowed for several stick-slip motions over a similar distance, where the peak of each contact reaches a similar maximum and the peaks occur at a regular distance as the probe is deformed while it moves. Figure 35 displays the contrasting end of the spectrum of preloading forces measured, where the friction traces and a bottom-view image of the contact offer a different perspective when comparing the flat and patterned PDMS samples.

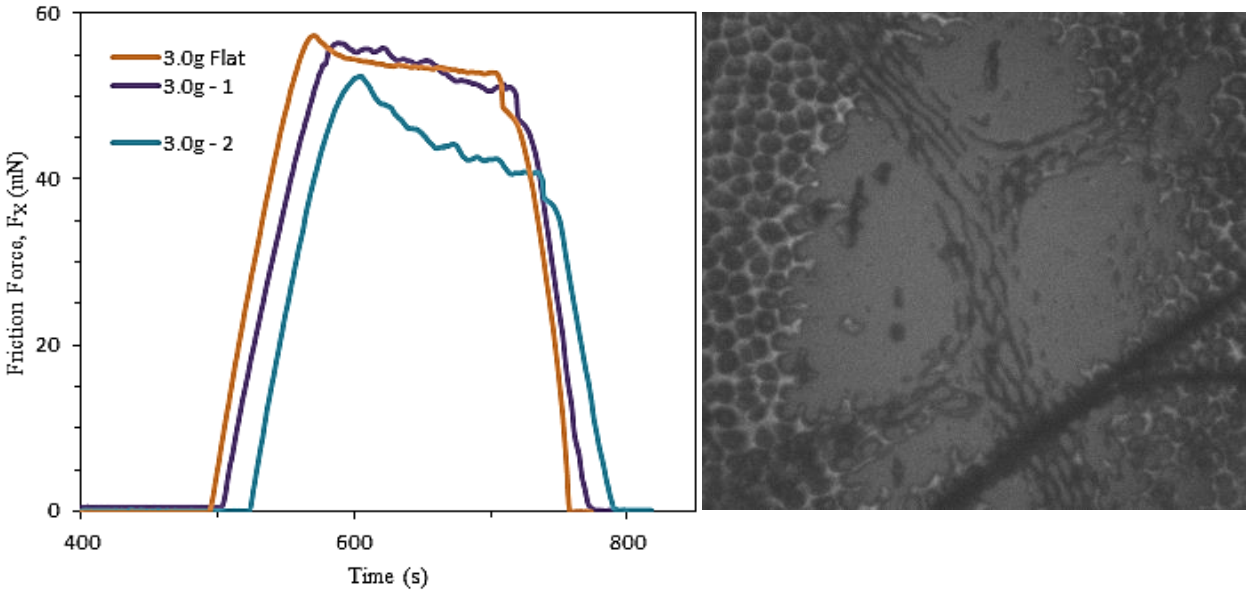

Figure 35: 29.4mN loading force applied to a synthetic leaf sample during a friction scan. The Friction traces on the left plot showcase the relatively similar nature of contact between the flat and patterned surfaces while the contact area shown in the right image displays the conformal contact at the interface while the probe scans the surface

Figure 35 offers the comparison to Figure 34 in that the maximum preload force of 29.4mN was used to contrast the patterned and flat PDMS samples. The stark difference in average F_X force measured in earlier trials supports the claim that the mechanism is different now that the preload has increased. At the greater preload, the difference in F_X between the flat and patterned samples is 12% of the preload value as opposed to 486% for 1.96mN. The bottom-view microscopic image in Figure 35 during the scan shows that the mechanism of contact has changed with the increasing preload to a more conformal state. The patterned friction traces are now much less "noisy" as the friction is much less-dependent on single asperity interactions, and instead based on a much larger surface are where the ability to continually recreate the area of contact is lost. However, the patterned surfaces did display the ability to retain some pockets of air at the interface beneath the probe, predominantly on the leading edge as the scan progressed resulting in the observed drop-off in friction force measured over the duration of the scan. Additionally, the friction traces show a similar stiction trend for the flat samples at the onset of lateral motion, where the patterned surfaces also experience a similar sticition spike due to the nature of the contact. The stick-slip motion mechanism experienced for the flat surface at the smaller preload is no longer present due to the greater loading force preventing the jumping of the probe, although from reviewing the bottom-view images, the deformation of the probe is obvious in forming a crescent shape near the end of the scan. The data collected can be observed quantitatively from the trials for this experiment as displayed in Table 3 below.

Table 3: Data collected for a variable preload comparison of the friction properties of both and flat and patterned PDMS samples. Note that the friction force was developed as described for previous friction testing (on page 54), and the resulting patterned data used for the *Friction Data* is the average from two separate trials

		Fx Friction Force (mN)				Friction Data		
Preload (g)	**Preload (mN)**	**Patterned 1**	**Patterned 2**	**Flat PDMS**	**Difference**	**Patterned COF**	**Flat COF**	**% Patterned of Flat COF**
0.2	1.96	2.65	2.52	12.12	9.535	1.319	6.184	21.33%
0.5	4.9	7.34	5.94	19.14	12.5	1.355	3.906	34.69%
1	9.8	17.62	14.31	27.24	11.275	1.629	2.780	58.61%
2	19.6	26.66	32.63	40.58	10.935	1.513	2.070	73.05%
3	29.4	52.81	46.24	53.26	3.735	1.685	1.812	92.99%

From this data, several comparisons can be drawn from the variable preload force applied to both the flat and patterned compliant PDMS surfaces. Within the range of these trials, the patterned surface was found to always decrease the friction force. However, comparing the data over the range of the tests, the flat coefficient of friction decreases as the preload is increased while the patterned coefficient remains

relatively constant. This results in the two values approaching one another as the preloaded normal force increases reflecting the increasingly similar mode of contact. The low preload trials also showcased the largest relative difference between the patterned and flat surfaces relative to the preload forces. This translated into the large gap between the flat and patterned surfaces observed in Figure 34 with low preload values and a primarily laid contact mechanism relative to the minimal difference observed at the greater preloads in conformal contact as observed in Figure 35. By decreasing the preload to very low values, the stiction prevalent regime of interfacial interactions dominating the friction forces measured is observed. This translates into the highest measured COF for the flat surfaces. Conversely, the high preload trails show the lowest COF for the flat PDMS surface. The trend from largest to smallest coefficient of friction follows the observed path from previous trails conducted on the epoxy substrate, where the curve in Figure 36 showcases the transition from classical Amontons' friction mechanic at the higher preload to the surface interaction mechanism of Bowden and Tabor at the lower.

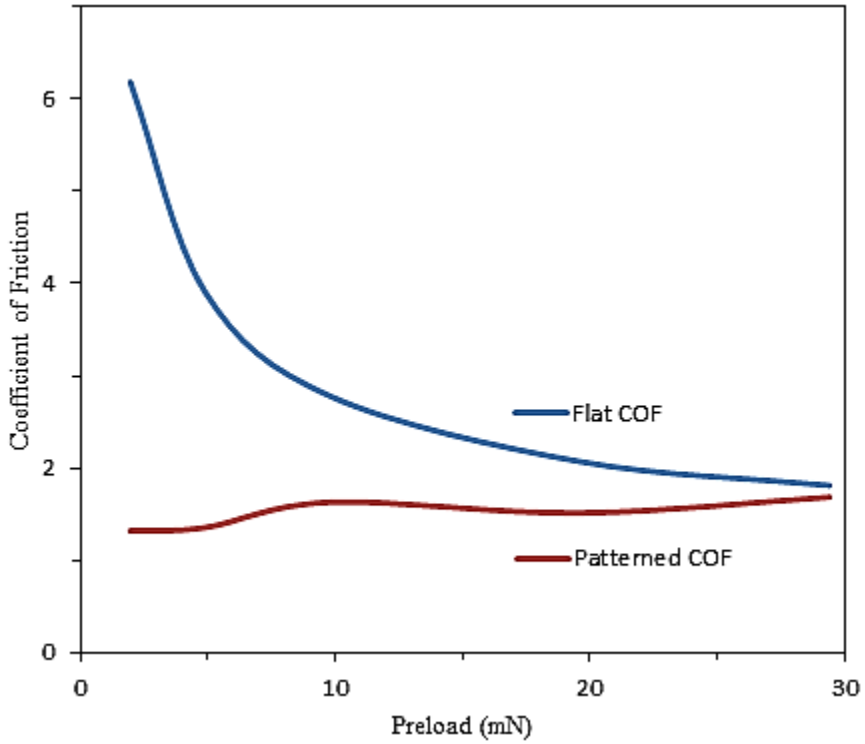

Figure 36: The local coefficient for both the patterned synthetic leaf and a flat PDMS sample as defined by the friction force as a function of a variable preloading force

From Figure 36 we are able to confirm the expected behaviour of the flat PDMS surface, where the transition from the interfacial dependent friction regime to the classical regime occurs over the preload range selected. The coefficient of friction for the flat surface will plateau and continue at a steady-state value as predicted by Amontons, where the average of the stick-slip shear forces measured will lose any dependence on the real area of contact. The patterned coefficient remains relatively constant

throughout the different preload values, and eventually matches the flat coefficient once conformal contact is achieved through the depression of the asperities achieving a complete contact area similar to the contact area with the flat PDMS surface. In fact, the measured friction for high preload values should began to surpass the flat surface values, which involves more than just the mechanics as proposed by Israelchvili where all the measured variables are equal once conformal contact is achieved. There has been much work to support the high adhesive ability of some patterned surfaces, such as the toe-pad of a gecko, where it is believed the directional configuration and setae shape of the nano-fibrils result in the increased adhesion [79], [87], [89], [90]. Moreover, several studies have reported the enhancement of friction from the interlocking of one or two patterned surfaces such that there are boundaries and contact lines not parallel with the direction of crack propagation at the surface [4], [7]. It can be predicted that if the normal force continues to increase past the levels in this investigation, the overall friction force observed for the patterned surface will surpass that of the flat PDMS.

Chapter 5

Icephobic Evaluation of Micro-Structured Surfaces

From the initial work completed in synthesizing a patterned surface able to be transferred to many different substrates, the application of an icephobic coating was pursued due to the robust nature of the epoxy system. The scope of icephobic work reported within this thesis looks at several qualitative observations of normalization tests performed to better understand the mechanism of freezing, and the potential icephobicity of different surfaces. Several important questions are explored including the manner in which condensation interacts and freezes on different hydrophobic surfaces, and the interaction of water droplets with different superhydrophobic surfaces. As the primary motivation of this work was the exploration of potential icephobic surfaces, this chapter serves to outline the set-up and intent of the icephobic research conducted. A potential icing experimental set-up is discussed and outlined to showcase the potential of the collected components for ice-adhesion quantification. Typical results that are generated from the novel set-up are introduced and discussed. The relevant freezing mechanism is described as per the direction of exploring biomimetically inspired superhydrophobic surfaces, to observe potentially icephobic results. More specifically, the experimental set-up allows for the creation of simulated rime icing conditions, where a super-cooled surface significantly decreases the freezing time of water droplets. This provides an accurate model for what occurs within a natural environment leading to accumulation and the many issues experienced from the icing of surfaces.

Traditional Icephobicity Measurements

In observing the behaviour of ice, it is important to note that the surface of ice will reflect the properties of an amorphous material even when the ice was frozen as a crystallized bulk structure. The surface of ice is composed of a multitude of arrangements that result from the ability of the water molecule to form up to four highly-directional hydrogen bonds [30], [57]. Focusing on the different behaviours and mechanisms of droplet freezing will allow for a better understanding of the fundamental interactions with a super-cooled surface. By observing the ice adhesion strength and the improvement offered through the use of a superhydrophobic coating, variables associated with the icephobic nature of the material are identified and isolated within experiments to indicate how to optimize the icephobicity.

A group at the University of Quebec directed by Masoud Farzaneh focused on understanding the freezing transition of water to ice and uses a unique means to quantify the ice-adhesion strength of a surface [15], [17], [47]. Sample surfaces are first coated with ice through the introduction of super-cooled micro-droplets of water into a wind-tunnel that is kept at sub-zero temperatures. This set-up most closely resembles the mechanism of rime icing which is of prime practical importance. The iced samples are then introduced to a homemade centrifuge device, where they are spun at increasing speeds until ice-adhesive

failure is realized at the interface. With the mass and area of the failure interface known along with the exact rotation speed of the sample, the shear stress at the interface, and therefore the relative ice-adhesion strength can be calculated. A Japanese group headed by Goro Yamauchi utilized an artificial snow machine to observe how different surfaces responded to the sliding of a mass of snow given surfaces with different coatings. Both the temperature of the set-up and snow left adhered to the surface were examined [3]. In studying the mechanism of ice-ice friction and the mechanism behind this interaction, Maeno et al. utilized two different icing set-ups, although both took place within a cold-room at sub-zero temperature (0 to -30°C) [52]. Distilled water was simply allowed to sit in this room until it froze, after which the measurements were taken using the purely polycrystalline ice samples which were prepared with a plainer to ensure parallel contact faces. Alizadeh et al. used a cooling plate set-up to freeze a 6µL droplet on a surface in a relatively low humidity environment to monitor the freezing transition of a water droplet. The surface was cooled at a rate of 20°C per minute while the droplet is monitored via infra-red thermography [49]. Another focus of their study was to measure any potential delayed freezing effects of hydrophobic surfaces by measuring the time taken to freeze a sample after it is applied to a super-cooled (via cooling-plate) hydrophobic surface versus other substrates at the same temperature. From this work they found that the hydrophobic surfaces did in fact delay the freezing of the droplets, and they suggest the potential to use these surfaces as a coating to prevent the accumulation of ice [49].

Experimental Set-up

There have been many testing procedures developed to attempt to quantify the icephobicity of different materials. However, the common shortcoming is that they are both very rudimentary and subject to many different variables, or that they involve very expensive and specialized equipment. To address this issue within the parameters of this laboratory, the equipment accessible was used with a simply designed cooling plate to propose a new method of quantifying the relative icephobicity of surfaces accurately.

The experimental set-up comprises of the existing UMT tribology instrument using a modified probe to provide a flat surface that will scan the surface of the sample and remove the frozen droplet while measuring the resistive shear force in the x-direction. The droplet itself is frozen by a peltier cooling plate that is powered by a current source. The peltier plate was purchased from TE-Tech as a single module that is potted to resist moisture damage during the cooling experiments, but otherwise used without modification. The cooling plate functions on the principles of the peltier effect, where the movement of an electrical current through a series of pn-junctions between the two plate-surfaces of the cooler results in the movement of heat in the form of a transportation of entropy through the charge carriers from one side to the other. In order to facilitate the heat transfer, the peltier cooler maintains a

defined difference in temperature (ΔT) from one faceplate to the other given a specific input voltage. With this stated, in order to avoid an accelerating heating process where heat is transferred across the plates, where to maintain the ΔT, the *cold* surface (top) will be continually heated from the *hot* surface (bottom) until inevitable equipment failure, a heat sink is essential. Experimental constraints are placed with the types of measurements that are desired, as any vibration or elasticity (with applied stress) has to be avoided. Therefore a solid heat sink was designed and fabricated to be used in conjunction with a coolant circulator to maintain a constant temperature on the *hot* face (bottom) of the peltier plate. With this set-up, the input voltage of the current source can be varied such that the *cold* face temperature can be set given the magnitude of the ΔT. The heat sink was modified post fabrication to better insulate the system to prevent heat loss, while an insulated ring was added on top of the heat sink around the peltier cooler to avoid the loss of cold-air. The water droplets that were used were applied to the surface via the automated syringe that is also used to apply droplets of a specific volume during contact angle testing. Figure 37 displays a bare representation of the experimental design, although the insulation is not present in this set-up.

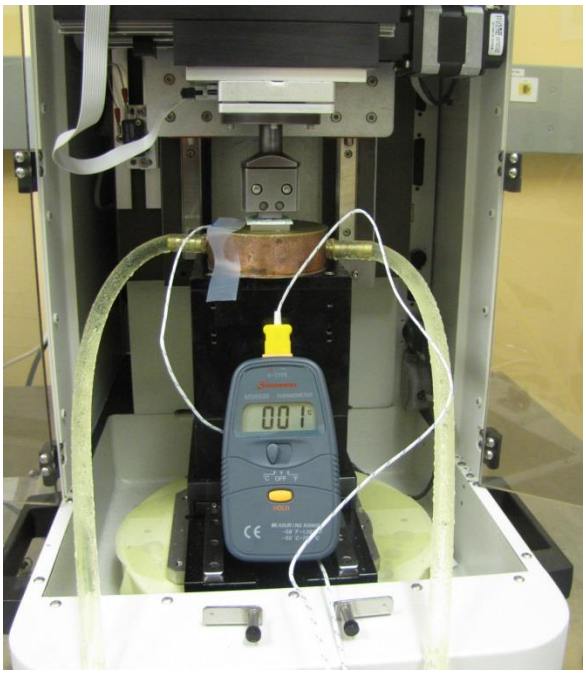

Figure 37: The basic set-up of the ice-adhesion testing apparatus. The heat sink was found to be able to maintain a constant temperature of 1°C at the *hot* (bottom) surface

Once the system was optimized, the peltier cooling plate was able to reliably reach temperatures of -10°C at the *cold* face. Figure 38 shows the transition of a droplet to a frozen droplet on the surface of PDMS when the peltier cooler is turned on. Note the mechanism of the shell freezing first before the bulk water freezes and forces the ice to expand upwards [55]. However the droplet is too small to fracture with the phase change.

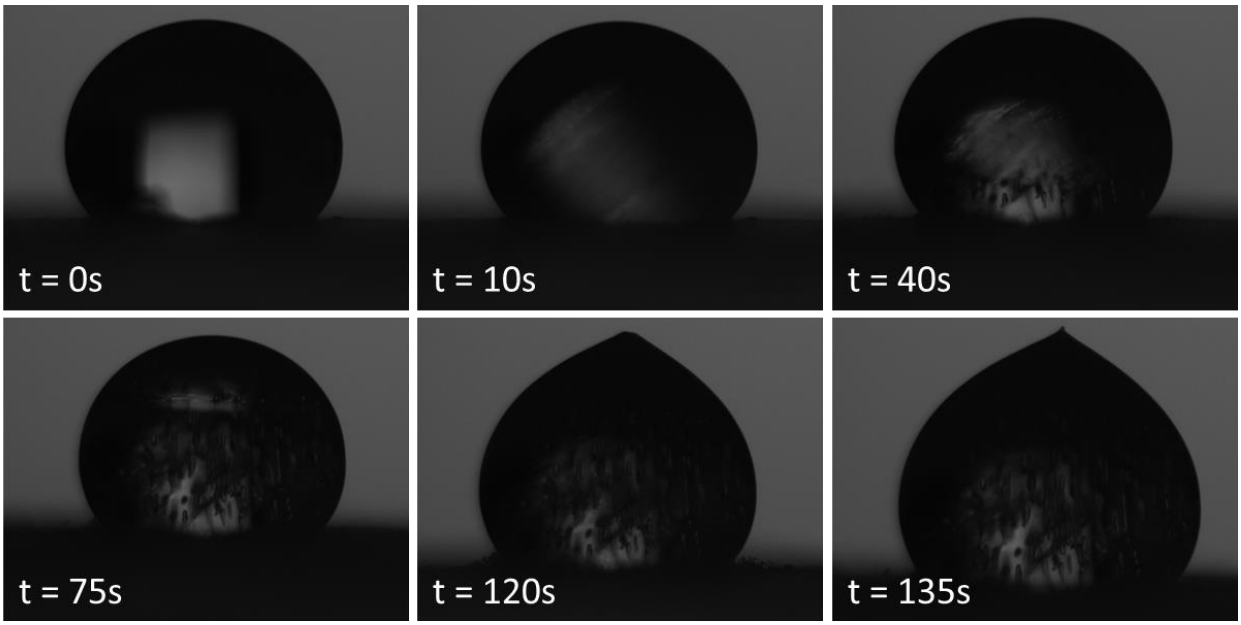

Figure 38: A timeline of a droplet freezing on an array of PDMS pillars displaying the mechanism of freezing on the superhydrophobic surface

Once the characteristic peak for the freezing a water droplet is observed, the probe is scripted to follow the routine of first approaching the surface, and then stepping back 1mm before scanning the surface at a defined speed and knocking the frozen droplet off. In utilizing a flat surface as the probe and scanning the surface at a height below what is observed at the widest circumference of the droplet, we ensure that the probe will contact the droplet at a single-point, and continue to increase the contact area as more force is applied to the ice until the droplet is sheared from the surface. Figure 39 displays a typical droplet prior to being frozen (left), along with the experimental set-up before the frozen droplet is knocked from the surface using a glass slide as the flat probe surface (right).

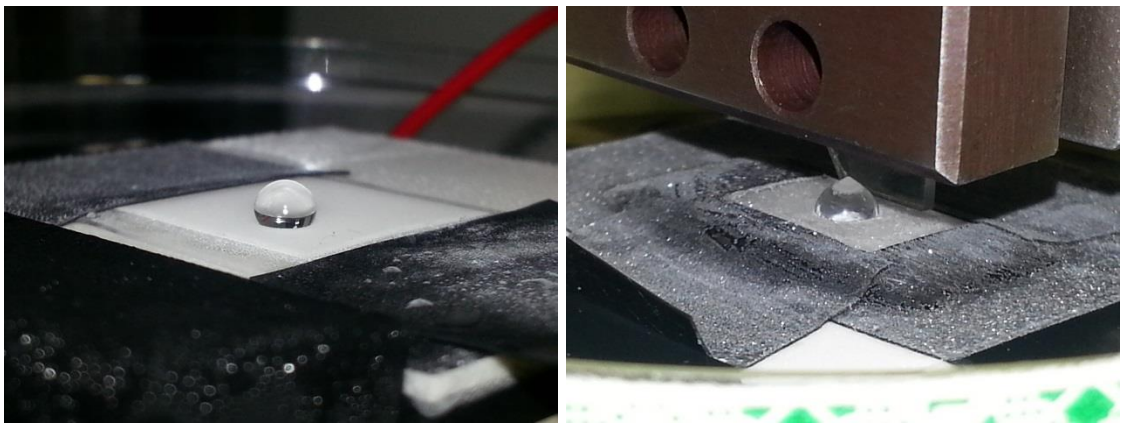

Figure 39: The freezing transition of a droplet on PDMS pillars as the peltier cooler is turned on. The right image also shows the probe and glass slide as it scans the surface prior to knocking the droplet off

As the probe scans the surface of the material, both the z- and x-direction force components are measured and recorded, where the amount of force it takes to remove the droplet at the interface can be observed. We are interested in the second step of this procedure, where the probe scans just above the surface until it contacts the frozen droplet, and proceeds to knock it off by separating the adhered solids at the interface. During the surface scan, we observe a sharp spike in the F_X force component as expected when the probe comes into contact with the immobilized frozen droplet. The non-ideal elastic nature of the probe materials leads to a matching peak observed in the F_Z direction due to some measured deflection of the probe in the z-direction that generates a force vector perpendicular to the shearing surface. This measured force is presumed to be a result of the probe deflecting as it contacts the frozen droplet and becomes hung up before the droplet is sheared at the contact interface. As a result, the magnitude of the resultant force vector can be measured through the force values in the x- and z-directions. Additionally, the angle of shear from the surface is able to be calculated and should be proportional to the measured amplitude if the elastic nature of the probe is the primary cause for the detection of force in the z-direction. Figure 40 outlines the basis of the probe interacting with the droplet frozen onto a surface along with the resulting force components that are measured in both the x- and z-direction throughout the scan.

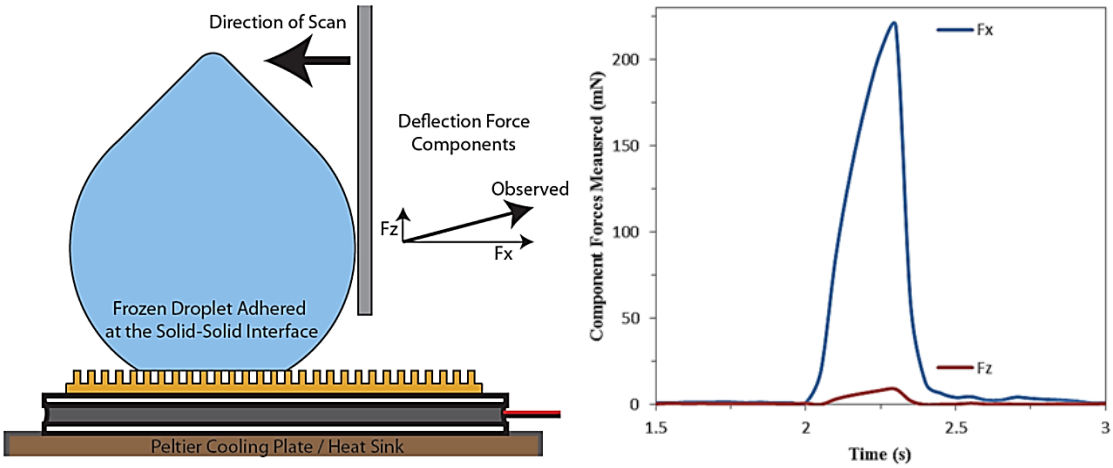

Figure 40: A schematic of the probes interaction with the frozen droplet during the scanning stage of the experiment (left) where the component forces shown with the interaction are characterized (right)

The results shown in Figure 40 are from a typical experiment, where only the scanning step is shown on the plot. Here the probe scanned the surface at a speed of 1mm/s, and therefore we can see that the probe moved less than 1mm from contact with the frozen droplet until it was sheared from the surface and knocked away completely. It is important to note that the F_X component force is much larger than the F_Z component which is essential to ensure that the system is not overly elastic, where the energy dissipation would lead to erroneous data. Figure 41 represents the before and after images of the experimental design where we observe that the frozen droplet is removed from the point of adhesion, after which the x-component force measured in Figure 40 drops back to zero.

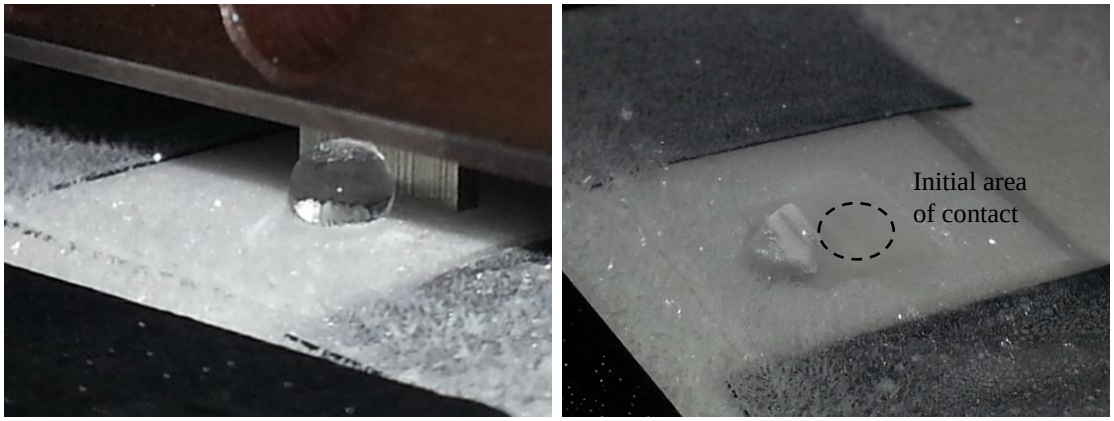

Figure 41: Before and following the knockoff of a frozen water droplet from a PDMS pillar array indicating the area from which the droplet was sheared at the interface (right)

As the droplet is sheared from the solid at the interface, it is the maximum force observed in both the z- and x-directions right before the moment of shear that is used to provide relative ice-adhesion strengths for different surfaces.

Icephobicity Testing

Initial testing involved trials of several different surfaces to gauge icephobicity, and compare relative results to other experiments run under similar conditions. Flat samples of PDMS were compared to patterned PDMS pillars to measure the difference in ice-adhesion that results from the reduction in real contact area observed from the patterned hydrophobic material. The flat samples were patterned using a cleaned glass slide as a substrate, before being peeled off and taped to the Peltier cooler. The Patterned samples were fabricated from an array of SU-8 micro-holes fabricated via UV-photolithography. More specifically, the resulting PDMS pillared structures are 45μm high and 30μm in diameter with a spacing of 67.5μm resulting in a surface density of 0.179. Additionally, a functionalized silica micro-particle with an average diameter of 500nm was embedded into an epoxy flat surface coated onto a glass substrate via a facile and reproducible dipping process that will be fully developed, characterized and discussed in further publications. The silica-particle coating is a superhydrophobic surface with a contact angle of 150° ± 5° consistently over the entire surface of a glass slide and a very low hysteresis, with a rolling angle of less than 2°. Figure 42 displays the hydrophobicity of the silica nano-particle coated epoxy surface along with SEM images of the surface showing the characteristic roughness resulting from particle aggregation.

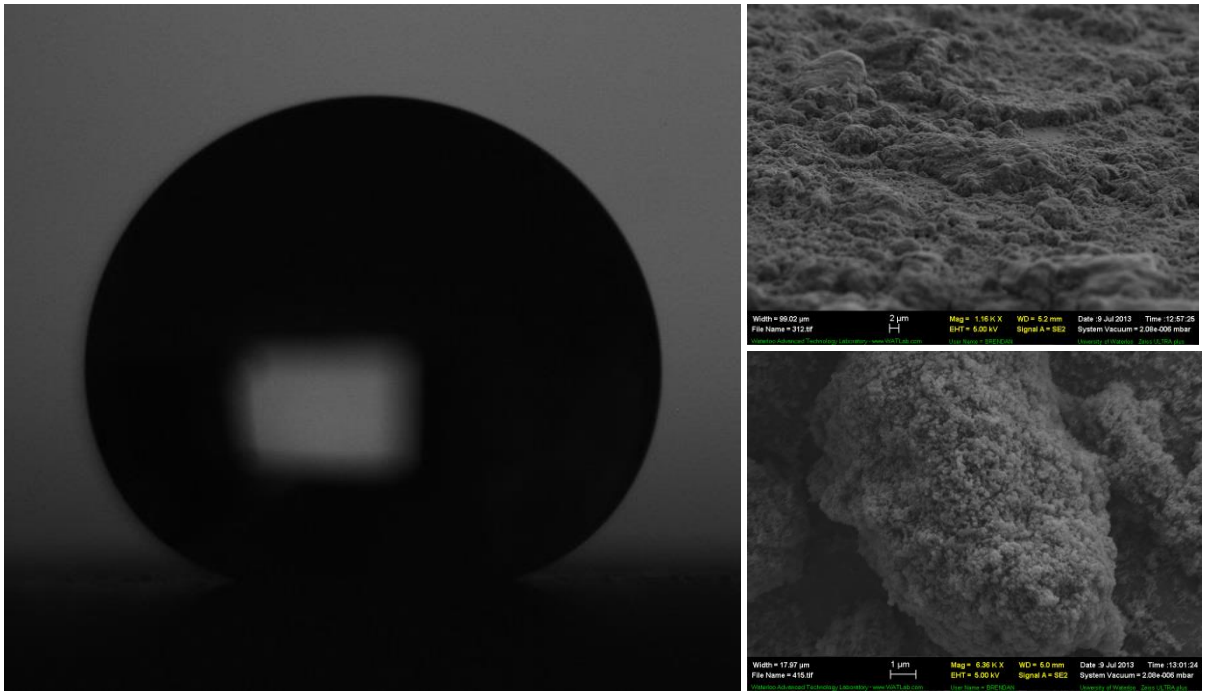

Figure 42: A droplet sitting on the silica-nanoparticle coated epoxy surface (left), and SEM images of the surface at 1160 times (top) and 6360 times magnification showing both the micro-roughness observed of particle aggregates that themselves possess nano-roughness resulting in a hierarchical system

Characterization of Ice Adhesion Strength

From the UMT experimental data, the vector forces in both the x- and z-planes is able to be quantified, and compared amongst different samples. From trialing several different surfaces, two trends were discovered. First, through patterning the equivalent PDMS material surface, a large increase in icephobicity was realized matching the increase in hydrophobicity and decreased hysteresis. Second, in comparing the icephobiity of the two types of surfaces, a counterintuitive finding was that the more hydrophobic embedded epoxy surface with the least hysteresis resulted in a less icephobic material. The data collected for a series of icephobicity surface-knockoff trials is collected in Table 4 below showing both vector forces, the ratio observed for the deflection of the probe, and the resultant vector magnitude and the angle for this vector against the shear plane.

Table 4: Data collected for F_X and F_Z force components during the frozen droplet (20µL) knockoff tests

Sample	Contact Angle	F_X (mN)	F_Z (mN)	$F_X : F_Z$	Vector Properties	
					Magnitude	Angle from Shear
Flat PDMS	115.6°	1118	689.9	4.52	3193.77	12.48°
PDMS Pillars	151.9°	219.5	9.016	24.35	219.71	2.35°
Epoxy Pillars	122.5°	5013	360.6	13.90	5025.66	4.12°
Epoxy/Silica - 0%	85.2°	8589	6901	1.24	11017.81	38.78°
Epoxy/Silica - 2%	146.0°	6977	972.2	7.18	7044.03	7.93°
Epoxy/Silica - 4%	155.0°	4655	235.2	19.79	4660.94	2.89°
Epoxy/Silica - 6%	153.9°	6603	927.1	7.12	6668.00	7.99°
Epoxy/Silica - 8%	148.7°	8531	5247	1.63	10015.31	31.59°

From the data collected, we are able to draw several conclusions about the surfaces tested within this investigation, as well as conclusions towards the potential improvements that are able to be incorporated into this testing procedure. Firstly, the addition of a pattern resulted in an increase of the icephobicity for both the PDMS surface and the epoxy patterned surface as shown in the larger magnitude of the force components for the flat PDMS and 0% concentration of silica particles in the epoxy surface. Figure 43 shows the results of directly comparing the shear force required to remove 20µL droplets from both the PDMS and epoxy surfaces.

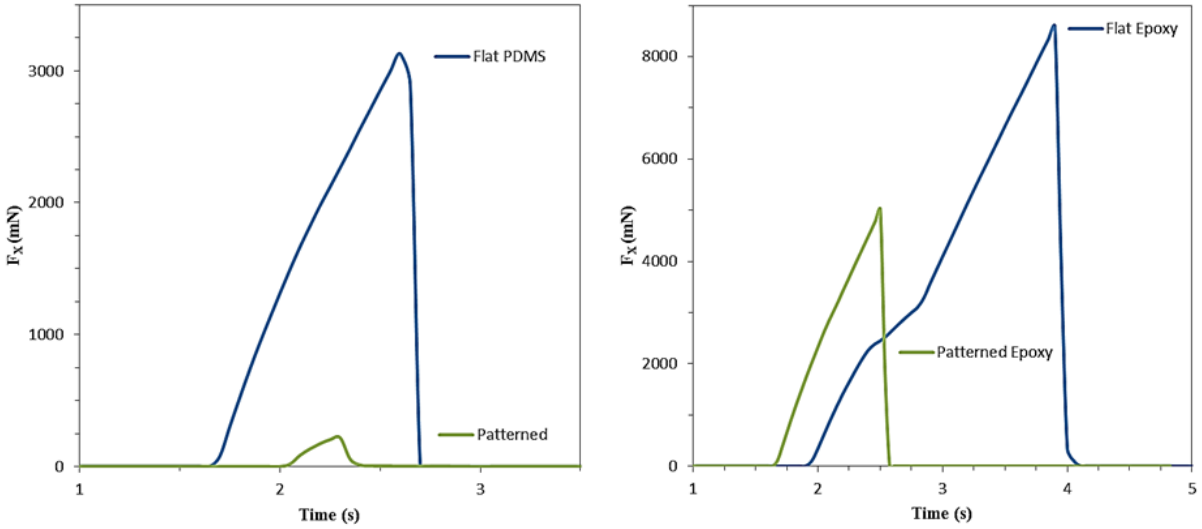

Figure 43: Trace of the F_X component force measured for both flat and patterned samples of PDMS (left and epoxy (right) as a 20µL droplet is knocked off of the surface

From Figure 43 the effect of the pattern is apparent in the decreased force required to knock the frozen droplet from the surface. In comparing the PDMS surfaces against the silica particle embedded epoxy surface that was found to possess a very low hysteresis, we observed that the PDMS surfaces were actually more icephobic than the more rigid and low hysteresis surface epoxy. In fact, the flat PDMS

surface showed a greater icephobic potential than the proven Cassie-wetted silica particles which have less real contact area due to air-pockets present at the interface. This is speculated to be because of the forced penetration of the frozen droplet into the irregular particles structures.

An additional study performed to better understand the nature of freezing water on different surfaces was performed by cooling the Peltier plate and allowing water to condense and then freeze on the surface. This testing generated some unique results, where ice crystals formed sitting on top of the patterned surfaces rather than the expected even coating of a frost like-layer as more and more water condensed on the surface. This observation applied to patterned surfaces of both PDMS and epoxy, where from a surface energy standpoint, one is hydrophobic and the other hydrophilic. Although slight frosting did occur across the interface prior to crystallization at a nucleation point, areas of frosting were observed to disappear around each ice-crystal as water was drawn off of the energetically unfavourable solid-liquid interface to crystallize in the low energy solid ice crystal. If was further noted that the hydrophobic PDMS surface produced larger crystals, which appeared to be the result of a larger area of water collection from the surrounding surface area.

The primary difference in the crystallization between the two materials was that when the Peltier cooler was shut-down, the surface returned to room-temperature quickly, and the ice quickly melted back into water. The hydrophilic epoxy material that was made hydrophobic with the application of the surface pattern showed a large bias to wet the surface, where the water formed into a very low contact angle droplet as opposed to the hydrophobic wetting state when the droplet was placed on top of the patterned surface. Conversely, the hydrophobic PDMS led to the water receding into droplets that would sit on top of pillars as opposed to wetting the surface even though it was known that the ice had penetrated the pillar array during freezing. This was observed from video recordings that showed the deflection of the elastic PDMS pillars as the ice crystal thawed, displaying one advantage of the compliant material, where the pillars adjusted to the frozen crystals without fracturing or compromising the integrity of the pattern. Repeated freezing and thawing cycles were performed on both the PDMS and epoxy micro-pillar arrays, where the resulting ability of the PDMS to be compliant enough and the epoxy material strong enough to survive the icing cycles without plastic deformation or degradation of the surface structures. After more than 20 complete freeze and thaw cycles, it was determined through contact angle testing and visual analysis under a microscope that the PDMS structure never incurred any damage even though it was constantly being moved and adjusted at sub-zero temperatures. This result points to the viability of these structures to serve as a potential anti-icing coating without further modification.

Testing Improvements

As a result of the elastic nature of the probing arm and the pendulum effect acting on the arm itself while it interacts with the frozen droplet, there will always be a deflection of the arm in the z-direction resulting in an overall force vector not aligned with the shear interface. This is unavoidable with the current set-up of the system; however, it would be ideal if the z-force component could be brought to zero. However, in looking at the results obtained from the initial trials, it is worth noting that there is a trend between the force component vector magnitude and the angle of this vector from the plane of shear.

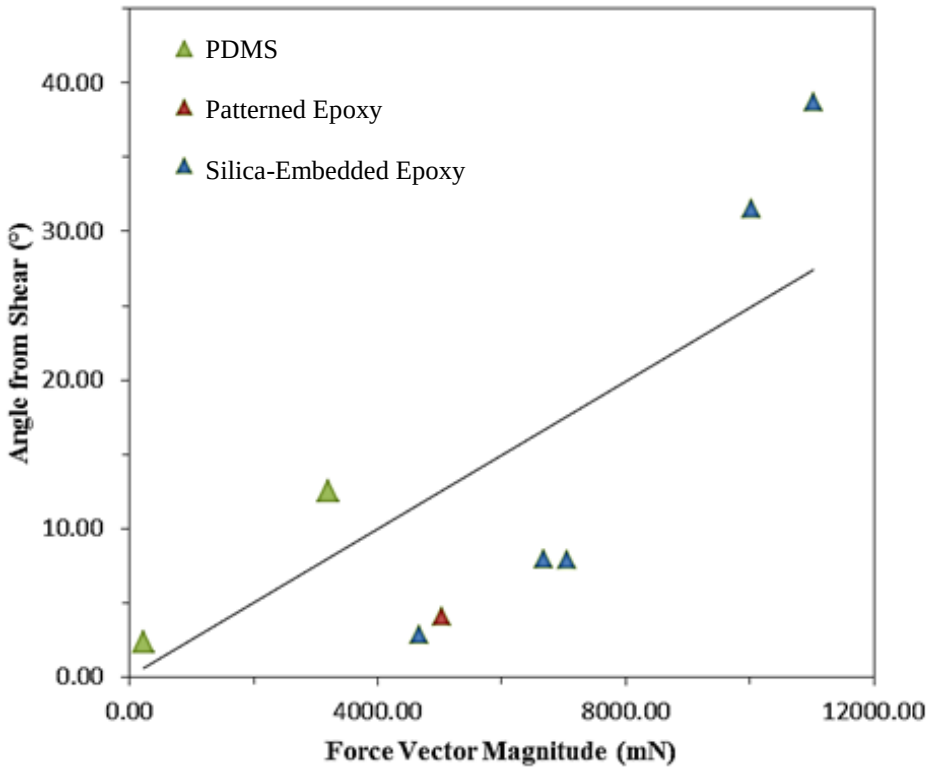

Figure 44: A comparison showing the linear relationship that can be derived from the magnitude of the force vector measured as a combination of F_X and F_Z and the deflection observed relative to the angle from shear of the magnitude vector

Figure 44 shows how the different material surfaces generally fall into different sections of this graph, indicating that the angle of shear, and thus the amount of deflection, is dependent on the surface properties. Within each material category, the observed ice-adhesion strength of the material is seems to closely follow the deflection value in a positive linear trend, which is expected due to the elastic nature of the probe and arm and being constant during all experiments. A more thorough investigation into the different freezing mechanisms based on the material surfaces, and the relationship between ice-adhesion strength and hysteresis is currently being performed for future publication. However, it is interesting to note that the observation of the surface with the lowest hysteresis having the relatively larger ice-adhesive strength differs from several established proposals that state that the hysteresis of a surface is proportional

to the ice-adhesion strength [17], [47], [48].From reading into the correlation studies, it is believed that the trend observed is the result of the use of fragile surfaces. The structures utilized to achieve the high contact angle and low hysteresis state are on the nano-scale and degrade easily through use. This was confirmed within the same studies to show a stark decrease in icephobicity after repeated trials as the surface broke down. Therefore, the initial icephobicty observed is believed to be the result of the water being frozen to the surface structures, which are then removed together during shear testing. Therefore it is actually the cohesive strength of the patterned surfaces that produces the icephobic values observed. Additionally, the high adhesive strength characteristics of the embedded epoxy substrate were found to be similar to other investigations that measure the ice-adhesion strength of similar surfaces [91].

Chapter 6

Conclusions and Recommendations

Within this thesis, the properties and primary mechanisms behind the interfacial wetting and tribiological behaviour of different surfaces was examined and characterized. With pre-made moulds of SU-8 on silica wafers, PDMS pillars were able to be generated for icephobic studies, while PDMS holes were fabricated to serve as a negative template for the subsequent synthesis of rigid epoxy micro-pillar arrays in a dual pattern transfer process. Trembling Aspen leafs were also taken from a tree on campus to serve as a mould for another dual pattern transfer process that results in a synthetic leaf reflective of the natural pattern of a hydrophobic leaf accurate on the micrometer scale. In both cases, the pattern transfer process were successful to the intended outcome, where a rigid epoxy micro-pillar array can be placed on curved surfaces mimicking an initially rigid pattern, and the synthetic leaves pattern transfer process generates a series of multiple use patterns the mimic the biological mould. The expansion of biomimicry should be relatively simple under current conditions where comparative studies have been performed for multiple plant species [12].

With the epoxy micro-pillar array, the strength of the pillars was examined and calculated through indentation tests, where quantifiable and relative results were obtained to support the *rigid* title applied to the modified material surface. The test indicated that the pillars themselves were able to withstand the application of a moderate amount of force before they were bent and plastically deformed rather than breaking or snapping. The epoxy pillars were then characterized in terms of the ability of a pattern to induce a superhydrophobic state to the hydrophilic epoxy surface. The specifics of the wetting state were discussed in detail given the ability to know the specifics of the surface properties. The mechanics behind the way in which a droplet evaporates from the different surfaces was discussed, where the epoxy pillars displayed a relatively high adhesion compared to other superhydrophobic surfaces. This was reflected in the observed tilting angle of the patterned surface relative to the flat epoxy surface, which was found to be approximately 23° when compared to the flat surface that could support a droplet when held at 90 and 180° angles. The tribological properties of the pillars, specifically the friction mechanics of a compliant probe scanning the relatively rigid surface were investigated in detail. The relationship between the preloading force and the resulting shear friction and coefficient of friction were discussed along with the development of the friction theory relevant to this work. The synthetic leaf sample was also characterized in terms of the wetting state throughout the different steps of the pattern-transfer process, where the role of the fluoropolymer monolayer in this process is speculated. The friction behaviour of the compliant material interacting with the likewise compliant PDMS probe with a variable preload normal force was developed. The difference derived from the application of a pattern to the

PDMS material in comparison to a flat PDMS surface in terms of the friction properties under light and heavy normal forces was determined along with the trending factors that show an increasingly indifference of the patterned surface as the preload is increased.

The icephobic potential of different materials was examined within the constraints of a designed ice-adhesion test proposed within this thesis. With the combination of several existing lab components, a viable means to measure the adhesive ability of different surfaces to frozen droplets is examined through a procedure designed to shear a droplet at the frozen interface. Data collected for several different samples contrast the icephobic potential for different materials, where flat versus patterned samples showcase the improvement resulting from decreasing the real area of contact with wetting in the Cassie Baxter regime. Comparing epoxy to PDMS surfaces displays the impact of a material specific surface energy on the icephobic potential. Furthermore, the contrast of a superhydrophobic low hysteresis epoxy surface embedded with silica nanoparticles to the relatively high hysteresis superhydrophobic patterned PDMS surfaces contrasts previous studies that aim to show a correlation between low hysteresis and improved icephobicity. In order to improve this work moving forward, there are several objectives to address, including the ability to predict the area of contact on the current set-up in order to complete subsequent calculations. Translating the relative ice-adhesion strength to a universally standard value would be simple in theory, although there are many potential sources of error that make this task difficult. The surface measured has the potential to effect the spreading of the water droplets with the presence of defects or chemical heterogeneity which would lead to inconsistent droplets and a variable area of contact. For this purpose, the bottom view camera utilized on the nano-indenter can provide the imprint of a typical contact, although the system could not be incorporated into the current set-up as it requires a transparent sample, where we also have the opaque heat sink and Peltier cooler. Alternatively, we could design some cooling chamber to provide a freezing atmosphere around the entire instrument, although this was deemed impractical within our current setting. Additionally, the use of a cooling plate leads to the heat capacity of the material being considered a variable based on the thickness of the substrate. More insulating or thicker materials would require more time to cool at the surface, and make any dynamic measurements very difficult to normalize.

Copyright Permissions

JOHN WILEY AND SONS LICENSE TERMS AND CONDITIONS

Sep 03, 2013

This is a License Agreement between Brendan McDonald ("You") and John Wiley and Sons ("John Wiley and Sons") provided by Copyright Clearance Center ("CCC"). The license consists of your order details, the terms and conditions provided by John Wiley and Sons, and the payment terms and conditions. All payments must be made in full to CCC. For payment instructions, please see information listed at the bottom of this form.

License date	Sep 03, 2013
Licensed content publisher	John Wiley and Sons
Licensed content publication	Macromolecular Materials & Engineering
Licensed content title	Biomimetic Micro-Patterning of Epoxy Coatings for Enhanced Surface Hydrophobicity and Low Friction
Licensed copyright line	© 2013 WILEY-VCH Verlag GmbH & Co. KGaA, Weinheim
Licensed content author	Brendan McDonald,Hamed Shahsavan,Boxin Zhao
Licensed content date	Jul 9, 2013
Type of use	Dissertation/Thesis
Requestor type	Author of this Wiley article
Format	Print and electronic
Portion	Full article

TERMS AND CONDITIONS

This copyrighted material is owned by or exclusively licensed to John Wiley & Sons, Inc. or one of its group companies (each a "Wiley Company") or a society for whom a Wiley Company has exclusive publishing rights in relation to a particular journal (collectively "WILEY"). By clicking "accept" in connection with completing this licensing transaction, you agree that the following terms and conditions apply to this transaction (along with the billing and payment terms and conditions established by the Copyright Clearance Center Inc., ("CCC's Billing and Payment terms and conditions"), at the time that you opened your RightsLink account (these are available at any time at http://myaccount.copyright.com).

Bibliography

[1] C. Neinhuis and W. Barthlott, "Characterization and Distribution of Water-repellent, Self-cleaning Plant Surfaces," *Annals of Botany*, no. 79, pp. 667–677, 1997.

[2] C. R. Crick and I. P. Parkin, "Preparation and Characterisation of Super-Hydrophobic Surfaces," *Chemistry*, vol. 16, pp. 3568–3588, 2010.

[3] H. Saito, K. Takai, and G. Yamauchi, "A Study on Snow Sticking Weight to Water-Repellent Coatings," *Materials Science Research International*, vol. 3, no. 4, pp. 216–219, 1997.

[4] A. Geim, S. Dubonos, I. Grigorieva, K. Novoselov, A. Zhukov, and S. Shapoval, "Microfabricated adhesive mimicking gecko foot-hair," *Nature Materials*, vol. 2, pp. 461–463, 2003.

[5] E. Martines, K. Seunarine, H. Morgan, N. Gadegaard, C. D. W. Wilkinson, and M. O. Riehle, "Superhydrophobicity and Superhydrophilicity of Regular Nanopatterns," *Nano Letters*, vol. 5, no. 10, pp. 2097–2103, 2005.

[6] M. Lamblet, E. Verneuil, T. Vilmin, A. Buguin, P. Silberzan, and L. Le, "Adhesion Enhancement through Micropatterning at Polydimethylsiloxane-Acrylic Adhesive Interfaces," *Langmuir*, vol. 23, no. 13, pp. 6966–6974, 2007.

[7] H. Shahsavan and B. Zhao, "Conformal Adheison Enhancement on Biomimetic Microstructured Surfaces," *Langmuir*, vol. 27, pp. 7732–7742, 2011.

[8] H. Shahsavan, D. Arunbabu, and B. Zhao, "Biomimetic Modification of Polymeric Surfaces: A Promising Pathway for Tuning of Wetting and Adhesion," *Macromolecular Materials and Engineering*, vol. 297, no. 8, pp. 743–760, Aug. 2012.

[9] B. Liu, Y. He, Y. Fan, and X. Wang, "Fabricating super-hydrophobic lotus-leaf-like surfaces through soft-lithographic imprinting," *Macromolecular Rapid Communications*, vol. 27, no. 21, pp. 1859–1864, Nov. 2006.

[10] D. M. Spori, T. Drobek, S. Zürcher, and N. D. Spencer, "Cassie-state wetting investigated by means of a hole-to-pillar density gradient," *Langmuir*, vol. 26, no. 12, pp. 9465–73, Jun. 2010.

[11] A. Solga, Z. Cerman, B. F. Striffler, M. Spaeth, and W. Barthlott, "The dream of staying clean: Lotus and biomimetic surfaces," *Bioinspiration & biomimetics*, vol. 2, no. 4, pp. S126–34, Dec. 2007.

[12] B. Bhushan and E. K. Her, "Fabrication of superhydrophobic surfaces with high and low adhesion inspired from rose petal," *Langmuir*, vol. 26, no. 11, pp. 8207–17, Jun. 2010.

[13] Y. Fang, G. Sun, T. Wang, Q. Cong, and L. Ren, "Hydrophobicity mechanism of non-smooth pattern on surface of butterfly wing," *Chinese Science Bulletin*, vol. 52, no. 5, pp. 711–716, Mar. 2007.

[14] S. Jung, M. K. Tiwari, N. V. Doan, and D. Poulikakos, “Mechanism of supercooled droplet freezing on surfaces.,” *Nature communications*, vol. 3, p. 615, Jan. 2012.

[15] G. Momen and M. Farzaneh, “Simple process to fabricate a superhydrophobic coating,” *Micro & Nano Letters*, p. 405, 2011.

[16] V. Bahadur, L. Mishchenko, B. Hatton, J. A. Taylor, J. Aizenberg, and T. Krupenkin, “Predictive model for ice formation on superhydrophobic surfaces.,” *Langmuir*, vol. 27, no. 23, pp. 14143–14150, Dec. 2011.

[17] R. Menini and M. Farzaneh, “Advanced Icephobic Coatings,” *Journal of Adhesion Science and Technology*, vol. 25, pp. 971–992, 2011.

[18] D. Quéré, “Wetting and Roughness,” *Annual Review of Materials Research*, vol. 38, no. 1, pp. 71–99, Aug. 2008.

[19] G. Castellanos, E. Arzt, and M. Kamperman, “Effect of Viscoelasticity on Adhesion of Bioinspired Micropatterned Epoxy Surfaces,” *Langmuir*, vol. 27, no. 12, pp. 7752–7759, Jun. 2011.

[20] F. Wu-Bavouzet, J. Cayer-Barrioz, A. Le Bot, F. Brochard-Wyart, and A. Buguin, “Effect of surface pattern on the adhesive friction of elastomers,” *Physical Review E*, vol. 82, no. 3, p. 31806, Sep. 2010.

[21] A. Winkleman, G. Gotesman, and R. Naaman, “Immobilizing a Drop of Water: Fabricating highly-hydrophobic Surfaces that Pin Water Droplets,” *Nano Letters*, vol. 8, no. 4, p. 1241, 2008.

[22] S. Kobayashi, E. Makino, T. Mineta, and T. Komatsuzaki, “Effects of microstructure geometry and plasma modification on wetting properties of SU-8 surfaces,” *Microelectronic Engineering*, vol. 88, no. 8, pp. 1775–1778, Aug. 2011.

[23] W. Zhang, F. K. Yang, Y. Han, R. Gaikwad, Z. Leonenko, and B. Zhao, “Surface and tribological Behaviors of the Bioinspired Polydopamine Thin Films UNder Dry and Wet Conditions,” *Biomacromolecules*, vol. 14, no. 2, pp. 394–405, Feb. 2013.

[24] B. P. Lee, P. B. Messersmith, J. N. Israelachvili, and J. H. Waite, “Mussel-Inspired Adhesives and Coatings,” *Annual review of materials research*, vol. 41, pp. 99–132, Aug. 2011.

[25] M. K. Chaudhury and G. M. Whitesides, “Direct measurement of interfacial interactions between semispherical lenses and flat sheets of poly(dimethylsiloxane) and their chemical derivatives,” *Langmuir*, vol. 7, no. 5, pp. 1013–1025, May 1991.

[26] K. Efimenko, W. E. Wallace, and J. Genzer, “Surface modification of Sylgard-184 poly(dimethyl siloxane) networks by ultraviolet and ultraviolet/ozone treatment,” *Journal of colloid and interface science*, vol. 254, no. 2, pp. 306–315, Oct. 2002.

[27] J. Israelachvili, *Intermolecular and Surface Forces*, Second. London: Elsevier Academic Press, 1991.

[28] Y. Berdichevsky, J. Khandurina, A. Guttman, and Y. H. Lo, “UV/ozone modification of poly(dimethylsiloxane) microfluidic channels,” *Sensors and Actuators B*, vol. 97, no. 2–3, pp. 402–408, Feb. 2004.

[29] D. Quéré, “Non-sticking drops,” *Reports on Progress in Physics*, vol. 68, no. 11, pp. 2495–2532, Nov. 2005.

[30] L. Bardella, “Mechanical behavior of glass-filled epoxy resins : experiments, homogenization methods for syntactic foams , and applications,” Université de Brescia, 2000.

[31] D. Bonn, J. Eggers, J. Indekeu, J. Meunier, and E. Rolley, “Wetting and spreading,” *Reviews of Modern Physics*, vol. 81, no. 2, pp. 739–805, May 2009.

[32] B. Bhushan and R. a. Sayer, “Surface characterization and friction of a bio-inspired reversible adhesive tape,” *Microsystem Technologies*, vol. 13, no. 1, pp. 71–78, Sep. 2006.

[33] F. Bowden and D. Tabor, “Friction, lubrication and wear: a survey of work during the last decade,” *British Journal of Applied Physics*, vol. 17, pp. 1521–1544, 1966.

[34] K. L. Johnson, K. Kendall, a. D. Roberts, T. R. Society, R. Society, and P. Sciences, “Surface energy and the contact of elastic solids,” *Proceedings of the Royal Society A*, vol. 324, no. 1558, pp. 301–313, Sep. 2012.

[35] H. Shahsavan, “Biomimetic Micro/Nano-Structured Surfaces: A Potential Tool for Tuning of Adhesion and Friction,” University of Waterloo, 2012.

[36] D. Tabor and J. McFarlane, “Relation Between Friction and Adhesion,” *Proceedings of the Royal Society of London Series A-Mathematical and Physical Sciences*, vol. 202, no. 1069, pp. 244–253, 1950.

[37] A. M. Homola, J. N. Israelachvili, P. M. Mcguiggan, and M. L. Gee, “Fundemental Experimental Studies in Tribology. The Transition from Interfacial Friction of Undamaged Molecularly Smooth Surfaces to Normal Friction with Wear,” *Wear*, vol. 136, no. 1, pp. 65–83, 1990.

[38] A. Faghihnejad and H. Zeng, “Fundementals of Surface Adhesion, Friction, and Lubercation,” in in *Polymer Adhesion, Friction, and Lubercation*, H. Zeng, Ed. John Wiley & Sons, Inc., 2013, pp. 1–58.

[39] A. Schallamach, “The Load Dependence of Rubber Friction,” *The Physical Society Section B*, vol. 65, no. 9, pp. 657–661, 1952.

[40] J. C. Berg, “Semi-empirical strategies for predicting adhesion,” in in *The Mechanics of Adhesion*, vol. 1, A. D. Chaudhury, Ed. Amsterdam: Elsevier B.V., 2002, pp. 1–73.

[41] D. E. Packham, “Some Contributions of Surface Analysis to the Development of Adhesion Theories,” *The Journal of Adhesion*, vol. 84, no. 3, pp. 240–255, Apr. 2008.

[42] K. R. Shull, D. Ahn, W. Chen, C. M. Flanigan, and A. J. Crosby, “Axisymmetric adhesion tests of soft materials,” *Macromolecular Chemistry and Physics*, vol. 199, no. 4, pp. 489–511, 1998.

[43] B. N. J. Persson, “Biological adhesion for locomotion: basic principles,” *Journal of Adhesion*, vol. 21, no. 12, pp. 1145–1173, 2007.

[44] S. N. Gorb, M. Sinha, A. Peressadko, K. a Daltorio, and R. D. Quinn, “Insects did it first: a micropatterned adhesive tape for robotic applications,” *Bioinspiration & biomimetics*, vol. 2, no. 4, pp. 117–125, Dec. 2007.

[45] M. Nosonovsky and B. Bhushan, “Multiscale friction mechanisms and hierarchical surfaces in nano- and bio-tribology,” *Materials Science and Engineering: R: Reports*, vol. 58, no. 3–5, pp. 162–193, Nov. 2007.

[46] L.-O. Andersson, P. Sture, and C.-G. Golander, “Ice adhesion to rubber materials,” *Journal of Adhesion Science and Technology*, vol. 8, no. 2, 1994.

[47] S. Kulinich and M. Farzaneh, “How Wetting Hysteresis Influences Ice Adhesion Strength on Superhydrophobic Surfaces,” *ACS Publications*, 2009.

[48] S. a Kulinich, S. Farhadi, K. Nose, and X. W. Du, “Superhydrophobic surfaces: are they really ice-repellent?,” *Langmuir*, vol. 27, no. 1, pp. 25–9, Jan. 2011.

[49] A. Alizadeh, M. Yamada, R. Li, W. Shang, S. Otta, S. Zhong, L. Ge, A. Dhinojwala, K. R. Conway, V. Bahadur, a J. Vinciquerra, B. Stephens, and M. L. Blohm, “Dynamics of ice nucleation on water repellent surfaces.,” *Langmuir*, vol. 28, no. 6, pp. 3180–6, Feb. 2012.

[50] G. Azimi, R. Dhiman, H.-M. Kwon, A. T. Paxson, and K. K. Varanasi, “Hydrophobicity of rare-earth oxide ceramics.,” *Nature materials*, vol. 12, no. 2, pp. 1–6, Jan. 2013.

[51] Q. Ke, W. Fu, H. Jin, L. Zhang, T. Tang, and J. Zhang, “Fabrication of mechanically robust superhydrophobic surfaces based on silica micro-nanoparticles and polydimethylsiloxane,” *Surface and Coatings Technology*, vol. 205, no. 21–22, pp. 4910–4914, Aug. 2011.

[52] N. Maeno, M. Arakawa, A. Yasutome, N. Mizukami, and S. Kanazawa, “Ice-ice friction measurements, and water lubrication and adhesion-shear mechanisms,” *Canadian Journal of Physics*, vol. 81, p. 241, 2003.

[53] K. K. Varanasi, T. Deng, J. D. Smith, M. Hsu, and N. Bhate, “Frost formation and ice adhesion on superhydrophobic surfaces,” *Applied Physics Letters*, vol. 97, no. 23, p. 234102, 2010.

[54] L. Yin, Q. Xia, J. Xue, S. Yang, Q. Wang, and Q. Chen, “In situ investigation of ice formation on surfaces with representative wettability,” *Applied Surface Science*, vol. 256, no. 22, pp. 6764–6769, Sep. 2010.

[55] S. Chatterji, “Aspects of the Freezing Porcess in a Porous Material-Water System,” *Cement and Concrete Research*, vol. 29, pp. 627–630, 1999.

[56] A.-M. Kietzig, S. G. Hatzikiriakos, and P. Englezos, “Physics of ice friction,” *Journal of Applied Physics*, vol. 107, no. 8, p. 081101, 2010.

[57] L. Ojamäe and L. Ojamae, “Crystalline Ice; Amorphous on the Surface,” *Nature Materials*, vol. 10, no. October, pp. 725–726, Oct. 2011.

[58] S. C. Colbeck, “Sliding temperatures of ice skates,” *American Journal of Physics*, vol. 65, no. 6, p. 488, 1997.

[59] D. Chandra and S. Yang, “Stability of High-Aspect-Ratio Micropillar Arrays,” *Accounts of Chemical Research*, vol. 43, no. 8, p. 1080, Aug. 2010.

[60] A. del Campo and C. Greiner, “SU-8: a photoresist for high-aspect-ratio and 3D submicron lithography,” *Journal of Micromechanics and Microengineering*, vol. 17, no. 6, pp. R81–R95, Jun. 2007.

[61] A. Olah, H. Hillborg, and G. J. Vancso, “Hydrophobic recovery of UV/ozone treated poly(dimethylsiloxane): adhesion studies by contact mechanics and mechanism of surface modification,” *Applied Surface Science*, vol. 239, no. 3–4, pp. 410–423, Jan. 2005.

[62] M. Owen and P. Smith, “Plasma Treatment of Polydimethylsiloxane,” *Journal of Adhesion Science and Technology*, vol. 8, no. 10, pp. 1063–1075, 1994.

[63] H. S. Erge, F. K. Z, N. Koca, and Y. Soyer, “Effect of Heat Treatment on Chlorophyll Degradation and Colour Loss in Green Peas,” *Academic Food Journal, GIDA*, vol. 33, no. 5, pp. 225–233, 2008.

[64] Dow_Corning, “Product Information - Sylgard 184 Silicone Elastomer,” 2007.

[65] N. J. Glassmaker, T. Himeno, C.-Y. Hui, and J. Kim, “Design of biomimetic fibrillar interfaces: 1. Making contact,” *Interface*, vol. 1, no. 1, pp. 23–33, Nov. 2004.

[66] Z. T. Burton and B. Bhushan, “Surface Characterization, Adhesion, and Friction Properties of Hydrophobic Leaf Surfaces and Nanopatterned Polymers for Superhydrophobic Surfaces,” Ohio State University, 2005.

[67] S. Farhadi, M. Farzaneh, and S. a. Kulinich, “Anti-icing performance of superhydrophobic surfaces,” *Applied Surface Science*, vol. 257, no. 14, pp. 6264–6269, May 2011.

[68] K. Koch, B. Bhushan, Y. C. Jung, and W. Barthlott, “Fabrication of artificial Lotus leaves and significance of hierarchical structure for superhydrophobicity and low adhesion,” *Soft Matter*, vol. 5, no. 7, p. 1386, 2009.

[69] J. Kwon, E. Cheung, S. Park, and M. Sitti, “Friction enhancement via micro-patterned wet elastomer adhesives on small intestinal surfaces,” *Biomedical materials*, vol. 1, no. 4, pp. 216–20, Dec. 2006.

[70] C. Majidi, R. E. Groff, Y. Maeno, B. Schubert, S. Baek, B. Bush, R. Maboudian, N. Gravish, M. Wilkinson, K. Autumn, and R. S. Fearing, “High friction from a stiff polymer using microfiber arrays,” *Physical Review Letters*, vol. 97, no. 7, p. 76103, Aug. 2006.

[71] E.-S. Yoon, R. a. Singh, H. Kong, B. Kim, D.-H. Kim, H. E. Jeong, and K. Y. Suh, "Tribological properties of bio-mimetic nano-patterned polymeric surfaces on silicon wafer," *Tribology Letters*, vol. 21, no. 1, pp. 31–37, Jan. 2006.

[72] Y. Okamoto, K. Nishio, J. Sugiura, M. Hirano, and T. Nitta, "Friction of elastomer-on-glass system and direct observation of its frictional interface," *Journal of Physics: Conference Series*, vol. 89, p. 012011, Nov. 2007.

[73] M. Varenberg and S. Gorb, "Shearing of fibrillar adhesive microstructure: friction and shear-related changes in pull-off force," *Journal of the Royal Society Interface*, vol. 4, no. 15, pp. 721–725, Aug. 2007.

[74] H. Yao, G. Della Rocca, P. R. Guduru, and H. Gao, "Adhesion and sliding response of a biologically inspired fibrillar surface: experimental observations," *Journal of the Royal Society, Interface*, vol. 5, no. 24, pp. 723–33, Jul. 2008.

[75] J. Lee, C. Majidi, B. Schubert, and R. S. Fearing, "Sliding-induced adhesion of stiff polymer microfibre arrays. I. Macroscale behaviour," *Journal of the Royal Society, Interface*, vol. 5, no. 25, pp. 835–44, Aug. 2008.

[76] L. Shen, N. J. Glassmaker, A. Jagota, and C.-Y. Hui, "Strongly enhanced static friction using a film-terminated fibrillar interface," *Soft Matter*, vol. 4, no. 3, p. 618, 2008.

[77] B. He, W. Chen, and Q. Jane Wang, "Surface Texture Effect on Friction of a Microtextured Poly(dimethylsiloxane) (PDMS)," *Tribology Letters*, vol. 31, no. 3, pp. 187–197, Aug. 2008.

[78] S. Vajpayee, R. Long, L. Shen, A. Jagota, and C.-Y. Hui, "Effect of rate on adhesion and static friction of a film-terminated fibrillar interface," *Langmuir*, vol. 25, no. 5, pp. 2765–71, Mar. 2009.

[79] M. P. Murphy, B. Aksak, and M. Sitti, "Gecko-inspired directional and controllable adhesion," *Small*, vol. 5, no. 2, pp. 170–5, Feb. 2009.

[80] M. Varenberg and S. N. Gorb, "Hexagonal Surface Micropattern for Dry and Wet Friction," *Advanced Materials*, vol. 21, no. 4, pp. 483–486, Jan. 2009.

[81] C. J. Rand and A. J. Crosby, "Friction of soft elastomeric wrinkled surfaces," *Journal of Applied Physics*, vol. 106, no. 6, p. 064913, 2009.

[82] N. Gravish, M. Wilkinson, S. Sponberg, A. Parness, N. Esparza, D. Soto, T. Yamaguchi, M. Broide, M. Cutkosky, C. Creton, and K. Autumn, "Rate-dependent frictional adhesion in natural and synthetic gecko setae," *Journal of the Royal Society, Interface*, vol. 7, no. 43, pp. 259–69, Feb. 2010.

[83] R. K. Kramer, C. Majidi, and R. J. Wood, "Shear-mode contact splitting for a microtextured elastomer film," *Advanced materials*, vol. 22, no. 33, pp. 3700–3, Sep. 2010.

[84] L. Ge, L. Ci, A. Goyal, R. Shi, L. Mahadevan, P. M. Ajayan, and A. Dhinojwala, "Cooperative adhesion and friction of compliant nanohairs," *Nano letters*, vol. 10, no. 11, pp. 4509–13, Nov. 2010.

[85] E. Buselli, V. Pensabene, P. Castrataro, P. Valdastri, A. Menciassi, and P. Dario, “Evaluation of friction enhancement through soft polymer micro-patterns in active capsule endoscopy,” *Measurement Science and Technology*, vol. 21, no. 10, p. 105802, Oct. 2010.

[86] B. Aksak, C.-Y. Hui, and M. Sitti, “The effect of aspect ratio on adhesion and stiffness for soft elastic fibres,” *Journal of the Royal Society, Interface*, vol. 8, no. 61, pp. 1166–75, Aug. 2011.

[87] M. P. Murphy, B. Aksak, and M. Sitti, “Adhesion and anisotropic friction enhancements of angled heterogeneous micro-fiber arrays with spherical and spatula tips,” *Journal of Adhesion Science and Technology*, vol. 21, no. 12–13, pp. 1281–1296, Jan. 2007.

[88] B. Bhushan, “Nanotribology, nanomechanics and nanomaterials characterization.,” *Philosophical transactions. Series A, Mathematical, physical, and engineering sciences*, vol. 366, no. 1869, pp. 1351–81, Apr. 2008.

[89] B. Zhao, N. Pesika, H. Zeng, Z. Wei, Y. Chen, K. Autumn, K. Turner, and J. Israelachvili, “Role of Tilted Adhesion Fibrils (Setae) in the Adhesion and Locomotion of Gecko-like,” *Journal of Physical Chemistry B*, vol. 113, no. 12, pp. 3615–3621, 2009.

[90] K. Autumn, Y. A. Liang, S. T. Hsieh, W. Zesch, W. P. Chan, T. W. Kenny, R. Fearing, and R. J. Full, “Adhesive force of a single gecko foot-hair,” *Nature*, vol. 405, no. June, 2000.

[91] R. Karmouch and G. G. Ross, “Superhydrophobic wind turbine blade surfaces obtained by a simple deposition of silica nanoparticles embedded in epoxy,” *Applied Surface Science*, vol. 257, no. 3, pp. 665–669, Nov. 2010.